

UNIVERSITÄT BONN

Physikalisches Institut

A Measurement of the Top Quark Mass with the DØ Detector at $\sqrt{s} = 1.96$ TeV using the Matrix Element Method

von

Kevin Kröninger

Using a data set of 158 and 169 pb⁻¹ of DØ Run-II data in the electron and muon plus jets channel, respectively, the top quark mass has been measured using the Matrix Element Method. The method and its implementation are described. Its performance is studied in Monte Carlo using ensemble tests and the method is applied to the Moriond 2004 data set. The top quark mass is measured to

$$\begin{aligned} m_{top}^{e+jets} &= 175.1^{+7.2}_{-6.1} (stat.)^{+10.5}_{-10.5} (syst.) \text{ GeV}/c^2 \\ m_{top}^{\mu+jets} &= 170.1^{+12.0}_{-11.6} (stat.)^{+10.7}_{-11.1} (syst.) \text{ GeV}/c^2 \\ m_{top}^{l+jets} &= 174.1^{+5.9}_{-5.1} (stat.)^{+10.5}_{-10.5} (syst.) \text{ GeV}/c^2 \end{aligned}$$

Post address:
Nussallee 12
53115 Bonn
Germany



BONN-IB-2004-06
Bonn University
April 2004

UNIVERSITÄT BONN

Physikalisches Institut

A Measurement of the Top Quark Mass with the DØ Detector at $\sqrt{s} = 1.96$ TeV using the Matrix Element Method

von
Kevin Kröninger

Dieser Forschungsbericht wurde als Diplomarbeit von der Mathematisch - Naturwissenschaftlichen Fakultät der Universität Bonn angenommen.

Angenommen am:	20.04.2004,
Referent:	Prof. N. Wermes
Korreferent:	Prof. E. Hilger

Contents

1. Introduction	1
2. Physics	3
2.1. The Standard Model	3
2.2. Top Quark Physics	4
2.2.1. Strong Top Quark Production	4
2.2.2. Weak Top Quark Production	7
2.2.3. Decay Channels	7
2.2.4. Top Quark Properties	9
2.2.5. Background Processes	12
3. Experimental Setup	15
3.1. The Tevatron Accelerator	15
3.2. The DØ Detector	15
3.2.1. The Tracking System	17
3.2.2. The Calorimeter System	20
3.2.3. The Muon System	22
3.2.4. Trigger	22
4. The Matrix Element Method	25
4.1. The Differential Cross Section as a Measure of the Production Probability	25
4.2. Detector Resolution	26
4.3. Estimation of Parameters	29
4.4. Application to $t\bar{t}$ Production and the Measurement of the Top Quark Mass . . .	29
5. Calculation of Event Probabilities	31
5.1. Transfer Functions	31
5.2. Calculation of the Signal Probability	32
5.2.1. Top Quark Mass and Total Cross Section	32
5.2.2. Integration of the Differential Cross Section	32
5.2.3. Jet-Parton Assignments and Multiple Solutions	35
5.2.4. Acceptance for $t\bar{t}$ Events	36
5.3. Calculation of the Background Probability	37
5.3.1. Integration of the Differential Cross Section	37
6. Derivation of the Transfer Functions	39
6.1. General Parameterization	39
6.2. Energy Mapping	39
6.2.1. Comparison to Run I	44
6.3. Corrections and Normalization	45

6.3.1. Parton-Level Corrections	45
6.3.2. η -dependent Corrections	45
6.3.3. Normalization	45
7. Monte Carlo Studies and Application to Data	47
7.1. First Studies of Parton Level Monte Carlo	47
7.2. Studies of Smeared Parton Level Monte Carlo	50
7.2.1. Comparison on Event by Event Basis	50
7.2.2. Ensemble Tests	53
7.2.3. Discrimination between Signal and Background	54
7.2.4. Calibration of the Mass Estimator	54
7.3. Studies of Reconstructed Monte Carlo Events	56
7.4. Application to Data	70
7.4.1. Single Event Likelihoods and Muon Resolution	75
7.4.2. Event Display	79
8. Systematic Uncertainties	81
9. Conclusion and Outlook	89
9.1. Final Result	89
9.2. Outlook: Plans, Improvements and Comparison to Run I	90
10. Further Improvements: A Jet Study	93
10.1. Jet Merging Algorithm	93
10.2. Resolution	96
10.3. Conclusion	100
A. Phase Space Calculations	103
B. Integration Techniques	105
C. Kinematic Solver	109
D. Data and Monte Carlo Samples	111
E. Data to Monte Carlo Comparison	113
Bibliography	119
Acknowledgements	122

1. Introduction

In High Energy Physics the existence and properties of fundamental particles together with their interactions are studied. Although the realm developed from the simple models of the Greek philosophers to the complex theories and models of today, the basic questions remained the same: what is the origin of matter and which are the fundamental building blocks? What are the forces between them? The Standard Model of Particle Physics merges the modern theories of electroweak and strong interaction. It knows three classes of particles: leptons (with the best known being the electron), quarks (the components of atomic nuclei) and the gauge bosons (the force carriers). Additionally, the yet not observed Higgs boson is predicted by the model.

The top quark is the most recently discovered quark. It was predicted by the electroweak theory as the isospin partner of the bottom quark. Electron-positron and hadron colliders had searched for it over many years when it was finally discovered by the CDF and DØ Collaborations in 1995. With the data set it was also possible to measure its mass to be around $175 \text{ GeV}/c^2$ which makes the top quark about two orders of magnitude heavier than all other quarks (for comparison, the next lighter quark is the bottom quark with a mass of roughly $5 \text{ GeV}/c^2$). This large mass leads to many interesting features like the short lifetime of the top quark and spin-correlations between top and antitop in pair production. In the Run II of the Tevatron these properties can be studied in more detail. In case of the mass it is not only important to cross-check the Standard Model but also to make predictions on the mass of the Higgs boson. This is done by performing electroweak fits to the data collected.

In this thesis a measurement of the top quark mass is presented using a technique developed during the Run I (the so called Matrix Element Method). It has been shown that the statistical power of the method exceeds the alternative approaches by a few GeV/c^2 . The method makes maximal use of the kinematic information measured in the detector as well as a certain assumption on the Standard Model production and decay model (i.e. the matrix element, which gives the method its name).

At the Tevatron, protons and antiprotons are accelerated and collide at a center-of-mass energy of $\sqrt{s} = 1.96 \text{ TeV}$. The top quark is dominantly produced in top-antitop-pairs and decays almost to 100% into a W boson and a b-quark. Since the W can decay leptonically or hadronically three channels are possible for the $t\bar{t}$ -pair: the di-lepton channel, the lepton + jets channel and the all-jets channel. In the present analysis the measurement is done in the $e + jets$ and $\mu + jets$ channels. Figure (1.1) shows the production and decay chain. The final state objects, observed in the detector, are 4 jets, which are the hadronized final-states of the partons involved, a lepton (in this case either an electron or a muon) and missing transverse energy. The latter accounts for the fact that the neutrino from the leptonic W decay is not observed in the detector due to its weak interaction. From momentum balance the transverse energy of the neutrino can be calculated.

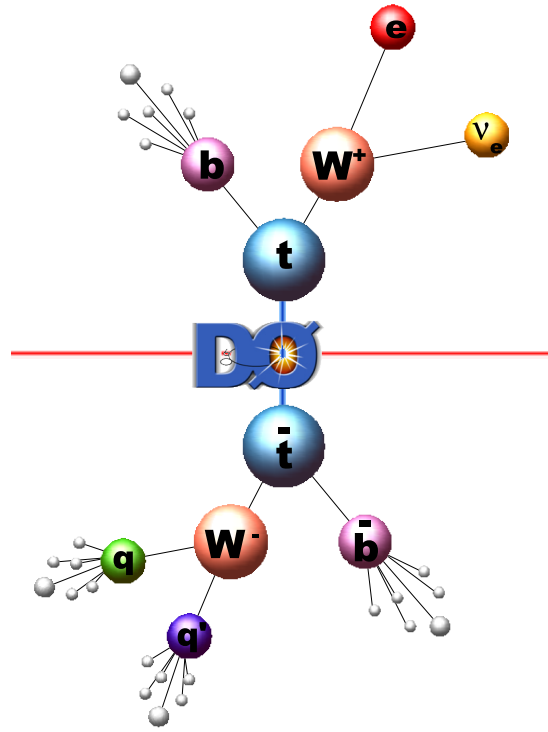


Figure 1.1.: Production and decay chain of $t\bar{t}$ events. The top-antitop-pair is produced in proton-antiproton collisions. Both top quarks decay instantaneously into a W boson and a bottom quark. In the lepton + jets channel one W decays into a lepton pair (here an electron and the corresponding electron neutrino) and the other W into hadrons, i.e. a (mostly light flavored) quark-antiquark pair.

This thesis is structured in the following way. Chapter 2 describes the physics processes with an emphasis on the top quark. Chapter 3 gives an overview on the Tevatron and the DØ detector. The main subcomponents are explained with references to the literature. A general introduction to the matrix element method is given in Chapter 4 with an application to the mass measurement. The calculations and specific processes involved are discussed in Chapter 5. An important ingredient of the method is the concept of transfer functions. Those account for the energy resolution and are derived in Chapter 6. Tests with Monte Carlo events and an application to data are presented in Chapter 7 with systematic studies in Chapter 8. After the conclusion and outlook in Chapter 9, a jet study is presented in Chapter 10. There, a merging algorithm for track and calorimeter jets is introduced in order to increase the quantity of selected events and study the effect on the quality of jets. The appendix summarizes technical details on the integrations performed in Chapter 4 and 5 and shows excerpts from the data to Monte Carlo comparison.

2. Physics

In the following the framework of the present analysis - the Standard Model - is introduced. The physics of the top quark, i.e. its production and decay processes and its properties, is explained in order to put the work into the right context.

2.1. The Standard Model

The Standard Model of Elementary Particle Physics combines the electromagnetic and weak (or electroweak) interactions with the strong interaction. Both are described by quantum field theories, namely the QED, QFD and QCD. Together with the mediators of forces (Table (2.1)), three families of quarks and leptons are known in this model. On the quarks side, these are the up (u), down(d), charm (c), strange (s), bottom (b) and top (t) quark, where the latter one is the most recently discovered and subject of this thesis. The leptons, electron (e), muon (μ) and tau (τ), come together with their almost massless partners, the neutrinos (ν_l). Additionally, the Standard Model predicts the Higgs boson which has not been observed yet, but is held responsible for the masses of the fermions and the gauge bosons.

$$\begin{aligned} \text{Quarks :} & \quad \begin{pmatrix} u \\ d \end{pmatrix} \quad \begin{pmatrix} c \\ s \end{pmatrix} \quad \begin{pmatrix} t \\ b \end{pmatrix} \\ \text{Leptons :} & \quad \begin{pmatrix} \nu_e \\ e \end{pmatrix} \quad \begin{pmatrix} \nu_\mu \\ \mu \end{pmatrix} \quad \begin{pmatrix} \nu_\tau \\ \tau \end{pmatrix} \end{aligned}$$

Due to fundamental concepts of the underlying gauge theories, all particles come along with their antiparticles, the most famous one being the positron - the antiparticle of the electron. In QCD, quarks do not only carry electric charge but also an abstract “color” charge which can be called red, green or blue.

Force	Relative Strength	Gauge Boson	Theory
Strong	1	8 gluons	QCD
Electromagnetic	10^{-2}	γ	QED
Weak	10^{-6}	W^\pm, Z^0	QFD
Gravitation	$< 10^{-40}$	Gravitons	Gen. Theory of Relativity

Table 2.1.: Forces with their corresponding mediators. The gravitational force is not included in the Standard Model but listed for completeness.

These particles can be claimed to be “elementary” since all matter or composite particles are made up of them. In order to gain further knowledge in the field of elementary particles it is therefore important to study the properties of quarks and leptons together with their interactions.

2.2. Top Quark Physics

The top quark is the most recently discovered quark. As the weak isospin partner of the bottom quark it is predicted by the Standard Model and was discovered in 1995 by the CDF and DØ collaborations. The large mass of the top quark leads to interesting properties, for example its short lifetime of about $0.5 \cdot 10^{-24}$ s (and therefore the inability to form bound states as $t\bar{t}$ or tb), and the spin correlation between the produced top and antitop. From a precision measurement of the top quark mass a prediction on the Higgs boson mass due to electroweak fits can be made. In the following, the production and decay processes of the top quark are introduced together with a short overview on its properties. Finally, the contributing background processes are discussed.

2.2.1. Strong Top Quark Production

At the Tevatron the top quark is dominantly produced via the strong interaction. Two subprocesses contribute to the production of $t\bar{t}$ pairs. At a center-of-mass energy of $\sqrt{s} = 1.8$ TeV ($\sqrt{s} = 1.96$ TeV) in the Run I (Run II) the quark-antiquark annihilation accounts for approximately 90% (85%), the gluon-gluon-fusion for roughly 10% (15%). Figure (2.1) shows the leading order Feynman diagrams corresponding to the contributing processes.

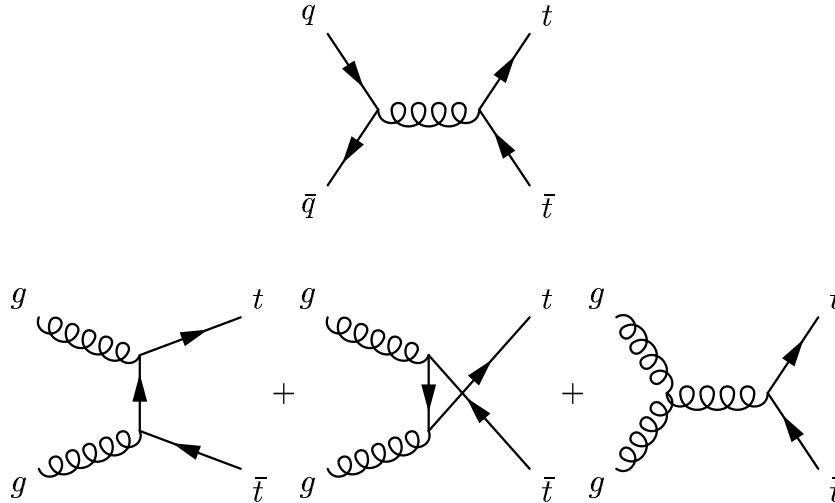


Figure 2.1.: Leading order Feynman diagrams for the $t\bar{t}$ -pair production at the Tevatron. **Top:** Quark-antiquark annihilation (85%). **Bottom:** Gluon-gluon-fusion (15%).

The total cross section for the production of $t\bar{t}$ pairs measured at CDF and DØ in the Run II of the Tevatron is consistent with the predictions from QCD calculations. In the Run II of the Tevatron it is preliminary measured to be [1]

$$\begin{aligned}\sigma_{t\bar{t}} &= 4.1 - 8.7 \text{ pb (CDF preliminary),} \\ \sigma_{t\bar{t}} &= 7.20 \text{ pb (lepton + jets, D0 preliminary).}\end{aligned}$$

The cross section of $t\bar{t}$ production depends on the center-of-mass energy. This can be explained by the parton model of the proton, in which the proton is composed of partons: quarks, antiquarks and gluons. In proton-antiproton collider experiments, single partons from each (anti-)proton interact¹ as demonstrated in Figure (2.2).

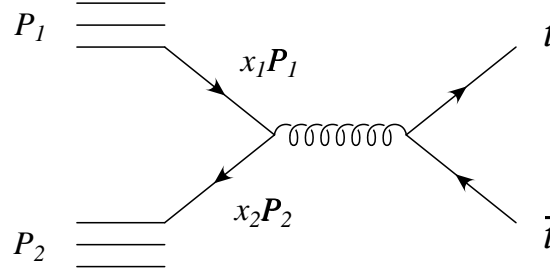


Figure 2.2.: Parton model of the proton: the proton is composed of quarks, antiquarks and gluons. The interacting partons only carry a fraction of the initial proton momentum.

The momenta carried by the two partons are only fractions (x_1 and x_2) of the initial (anti-)proton momenta. Assuming 4-momenta of p_1 and p_2 for proton and antiproton respectively, the parton momenta are x_1p_1 and x_2p_2 . The center-of-mass energy for the hard scattering process is therefore

$$\hat{s} = (x_1p_1 + x_2p_2)^2 \approx 2 \cdot x_1x_2p_1p_2 = x_1x_2 \cdot s, \quad (2.1)$$

where the masses of the initial quarks are neglected. From energy- and momentum-conservation it follows that in order to produce top-antitop pairs, the center-of-mass energy has to be larger than twice the top quark mass. Assuming, for the sake of the argument, the fractions of proton momenta to be equal on average ($x_1 \approx x_2 = x$) the following relation holds:

$$x \approx \frac{2 \cdot m_{top}}{\sqrt{s}}. \quad (2.2)$$

Assuming a top quark mass of $175 \text{ GeV}/c^2$ the fraction of proton momentum required to produce a $t\bar{t}$ pair is approximately $x = 0.18$ at the Tevatron (Run II). From the parton distribution functions (PDFs) it can be derived that the probability $xf(x)dx$ for a parton to carry a fraction of momentum between x and $x+dx$ increases with lower momentum fractions. From Figure (2.3), which shows the CTEQ5D parton distribution function [2] at $Q^2 = m_{top}^2$ and $Q^2 = 400 \text{ GeV}^2$, it can also be concluded that the fraction of quark-antiquark-annihilation in the production process decreases with increasing center-of-mass energy. Figure (2.4) shows one of the most recent calculations of the $t\bar{t}$ -pair production cross section in NNLO [3] (again assuming a top quark mass of $175 \text{ GeV}/c^2$). The measured cross sections from CDF and DØ are fully consistent with the prediction.

¹also, so called “multi parton interactions” occur in which partons can interact with other partons from the remnant of a prior scattering process leading to so called “underlying events”. Those are not taken into account for the calculation presented

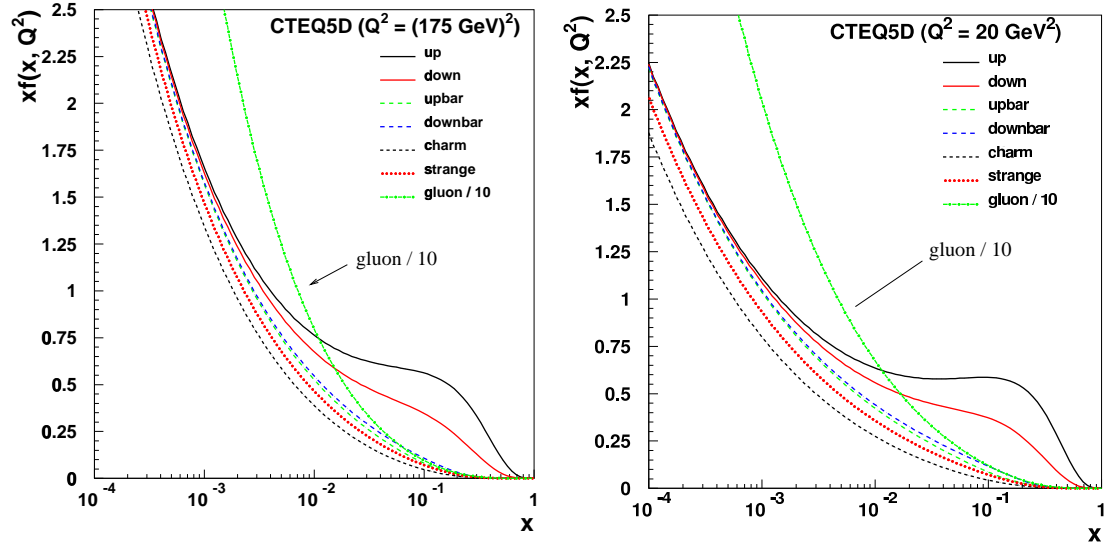


Figure 2.3.: CTEQ5D parton distribution functions at $Q^2 = m_{top}^2$ (left) and $Q^2 = 400 \text{ GeV}^2$ (right).

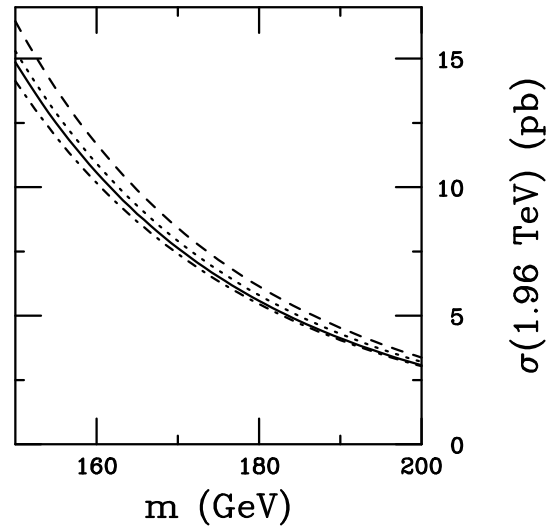


Figure 2.4.: NNLO calculation of the strong $t\bar{t}$ -pair production cross section.

2.2.2. Weak Top Quark Production

Similar to all other fermions, the top quark also interacts via the (V-A) charged-current weak interaction. This implies additional production processes which are shown in Figure (2.5). The cross section for these processes is predicted to be smaller than the strong production but on the same order of magnitude. So far, only limits have been obtained from the CDF and DØ experiments due to the forward topology of the events and the large amount of background. The limits are still weaker than the Standard Model prediction by more than an order of magnitude. The DØ experiment preliminary measures these limits to

$$\begin{aligned} \text{t-channel} : \sigma(qb \rightarrow qt) &< 15 \text{ pb (95\% CL)} \quad (\sigma_{theory} = 2.12 \pm 0.24 \text{ pb}) \\ \text{s-channel} : \sigma(q\bar{q} \rightarrow t\bar{q}) &< 16 \text{ pb (95\% CL)} \quad (\sigma_{theory} = 0.88 \pm 0.06 \text{ pb}) \end{aligned}$$

The t-channel calculation is NLO and can be found in [4], whereas the s-channel cross section is NNLO and taken from [5, 6].

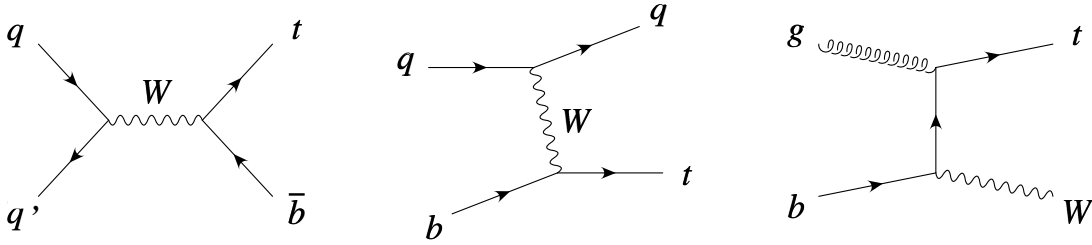


Figure 2.5.: Weak top quark production processes. **Left:** s-channel. **Middle:** t-channel. **Right:** associate production with a W .

2.2.3. Decay Channels

The top quark decays predominantly into a W boson and a b quark ($\text{BR} \approx 100\%$ as predicted from the Standard Model due to $|V_{tb}| \simeq 1$). The subsequent decays of both W bosons (the top quark is dominantly produced in pairs which will be assumed exclusively throughout the analysis) characterizes the signature of the event. The W can decay into a pair of leptons (a charged electron ($\text{BR} = (10.72 \pm 0.16)\%$), muon ($\text{BR} = (10.57 \pm 0.22)\%$) or tau ($\text{BR} = (10.74 \pm 0.27)\%$), together with the corresponding neutrino) or into hadrons ($\text{BR} = (67.96 \pm 0.35)\%$), i.e. a pair of quarks. The branching ratios, as presently listed in [7], are stated in brackets. Three decay channels are therefore distinguished: the di-lepton channel, where both W 's decay leptonically, the lepton + jets channel, in which one W decays leptonically, the other hadronically and the all-jets channel with both W 's decaying into hadrons. The branching ratios are visualized in the pie chart shown in Figure (2.6).

Due to the large mass of the top quark its lifetime is rather short: $\tau \simeq 0.5 \cdot 10^{-24} \text{ s}$. Therefore, it decays before hadronization is possible (the hadronization time scale is of the order of $\mathcal{O}(10^{-23} \text{ s})$) leading to the fact that bound $t\bar{t}$ states cannot be formed. A detection of the top quark is only possible via its decay products.

This analysis is focussed on the lepton + jets channel (excluding the τ + jets channel). The fractions of events in the $e + \text{jets}$ and $\mu + \text{jets}$ channels can be calculated from the branching ratios of the W boson, where in this calculation the fraction the τ 's decaying into the corresponding lepton are included:

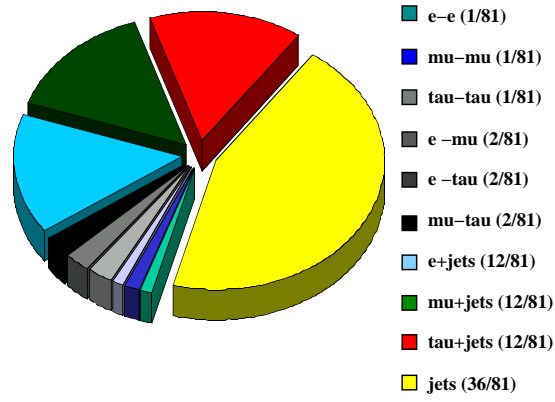


Figure 2.6.: Pie chart of the $t\bar{t}$ decay channels. The most probable is the all-jets channel, the di-lepton channels are rather rare. The numbers quoted are leading order and have to be corrected by higher order contributions.

$$\begin{aligned}
 \text{BR}(t\bar{t} \rightarrow l + jets) &= \text{BR}(t\bar{t} \rightarrow WWb\bar{b} \rightarrow l\nu_l b\bar{b} q\bar{q}') \\
 &= (\text{BR}(t \rightarrow Wb))^2 \cdot 2 \cdot \text{BR}(W \rightarrow qq') \cdot \\
 &\quad (\text{BR}(W \rightarrow l\nu_l) + \text{BR}(W \rightarrow \tau\nu_\tau) \cdot \text{BR}(\tau \rightarrow l\nu_l\nu_\tau)).
 \end{aligned}$$

Inserting the numbers for electrons and muons one obtains

$$\begin{aligned}
 \text{BR}(t\bar{t} \rightarrow e + jets) &= (17.10 \pm 0.24)\%, \\
 \text{BR}(t\bar{t} \rightarrow \mu + jets) &= (16.83 \pm 0.32)\%.
 \end{aligned}$$

The branching ratios are summarized in Table (2.2.3).

Process	Branching ratio
$t \rightarrow Wb$	≈ 0.998
$W \rightarrow e\nu$	$(10.72 \pm 0.16)\%$
$W \rightarrow \mu\nu$	$(10.57 \pm 0.22)\%$
$W \rightarrow \tau\nu$	$(10.74 \pm 0.27)\%$
$W \rightarrow \text{hadrons}$	$(67.96 \pm 0.35)\%$
$\tau \rightarrow e\nu\nu$	$(17.84 \pm 0.06)\%$
$\tau \rightarrow \mu\nu\nu$	$(17.37 \pm 0.06)\%$

Table 2.2.: Branching ratios used for the calculation of the branching ratios for the electron and muon channel. The numbers are taken from [7].

2.2.4. Top Quark Properties

Since the top quark is the latest one observed, its properties are yet almost unexplored. The fact that the top quark has such a heavy mass gives rise to many interesting features.

Mass, EW Fits The mass of the top quark is by far the largest of all fundamental particles. It is about the mass of a gold atom and has been measured to be [8]

$$m_{top} = (178.0 \pm 4.3) \text{ GeV}/c^2.$$

From a precision measurement of the top quark mass it is possible to make predictions for the (not yet discovered) Higgs boson mass. In the electroweak theory, the W boson mass can be calculated on tree-level:

$$\begin{aligned} M_W^2 &= \frac{1}{2} M_Z^2 \left(1 + \sqrt{1 - \frac{4\pi\alpha}{\sqrt{2}G_F M_Z^2}} \right) \\ &= \frac{\frac{\pi\alpha}{\sqrt{2}G_F}}{s_W^2}, \quad s_W^2 := 1 - \frac{M_W^2}{M_Z^2}, \end{aligned} \quad (2.3)$$

where the fine-structure constant α , the Fermi coupling constant G_F and the mass of the Z boson M_Z are known to high precision [7]. Taking into account loop corrections the formula for the W boson mass has to be divided by a factor $(1 - \Delta r)$, where two contributions include the top and the Higgs mass respectively:

$$(\Delta r)_{top} \approx -\frac{3}{8} \frac{G_F m_{top}^2}{8\sqrt{2}\pi^2 \tan \theta_W} \quad (2.4)$$

$$(\Delta r)_{Higgs} \approx \frac{11}{3} \frac{G_F M_Z^2 \cos \theta_W}{8\sqrt{2}\pi^2} \cdot \ln \frac{m_h^2}{M_Z^2} \quad (2.5)$$

As can be seen from Equations (2.4) and (2.5), the top mass enters the calculation of the W mass quadratically, the Higgs mass only logarithmically. These two contributions can be used in order to estimate the Higgs mass in case the W and top mass are measured precisely. Figure (2.7) shows the confidence level contours of a fit of the Standard Model to data as a function of the top quark and W boson masses. The solid line is the 1 sigma contour. Also shown in this figure are lines of constant Higgs masses. The shaded region is allowed by the Standard Model, experimentally accessible and not yet experimentally excluded. A lower limit of 114.4 GeV/c² was calculated from the LEP data, whereas the upper limit comes from Standard Model constraints. In the Run II of the Tevatron a measurement of the W mass with an uncertainty of 20 MeV/c² is expected. In order to make full use of the measurement a 3 GeV/c² error on the top mass is required.

Historically, these calculations have been used to estimate the mass of the top quark before its discovery. Figure (2.8) shows the χ^2 of the electroweak fit as a function of the top quark mass for different Higgs mass settings. The development of the top mass estimate with time is shown in Figure (2.9), including the direct measurements from CDF and DØ.

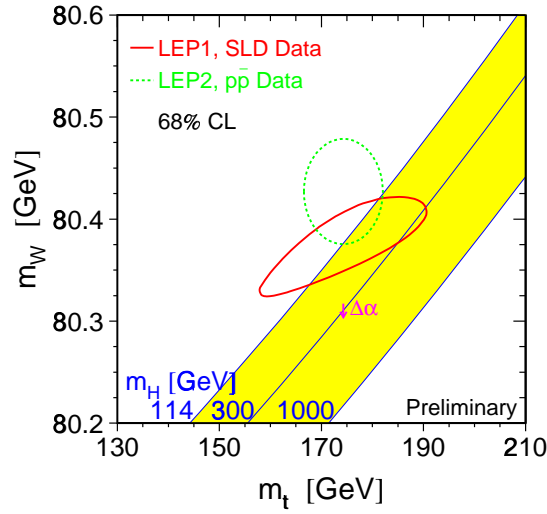


Figure 2.7.: Electroweak fit to the data from LEP, SLD and the Tevatron [9], the solid ellipse is the 1σ prediction limit. An increase of precision in the measurement of the W boson mass to $20\text{ MeV}/c^2$ translates into a precision of $3\text{ GeV}/c^2$ in the measurement of the top quark mass.

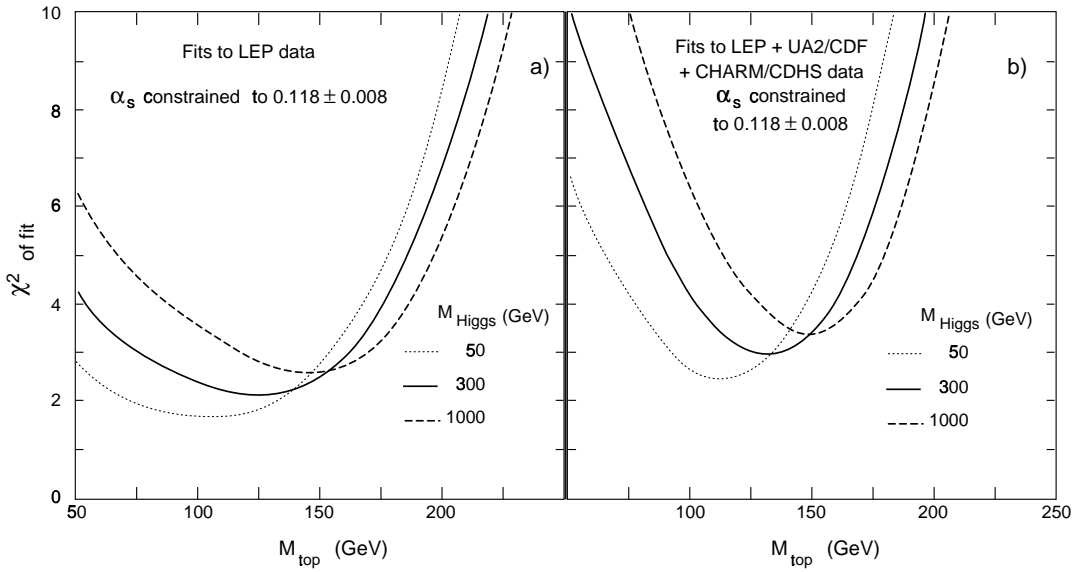


Figure 2.8.: χ^2 of the electroweak fit to data as a function of the top quark mass using LEP data (**left**) and LEP, hadron collider and neutrino experiment data (**right**) [10].

W-Helicity Due to the V-A structure of the weak interaction in the Standard Model the W boson from the top decay has either zero or negative helicity, the fraction of the former being $f_0 = \frac{m_{top}^2/2m_W^2}{1+m_{top}^2/2m_W^2} \approx 70\%$ in the top rest frame. A measurement of the angles between the lepton and the b quark in the leptonic branch makes it possible to estimate the fractions of negative (f_-), zero (f_0) and positive (f_+) helicity of the W boson. Previous measurements yielded

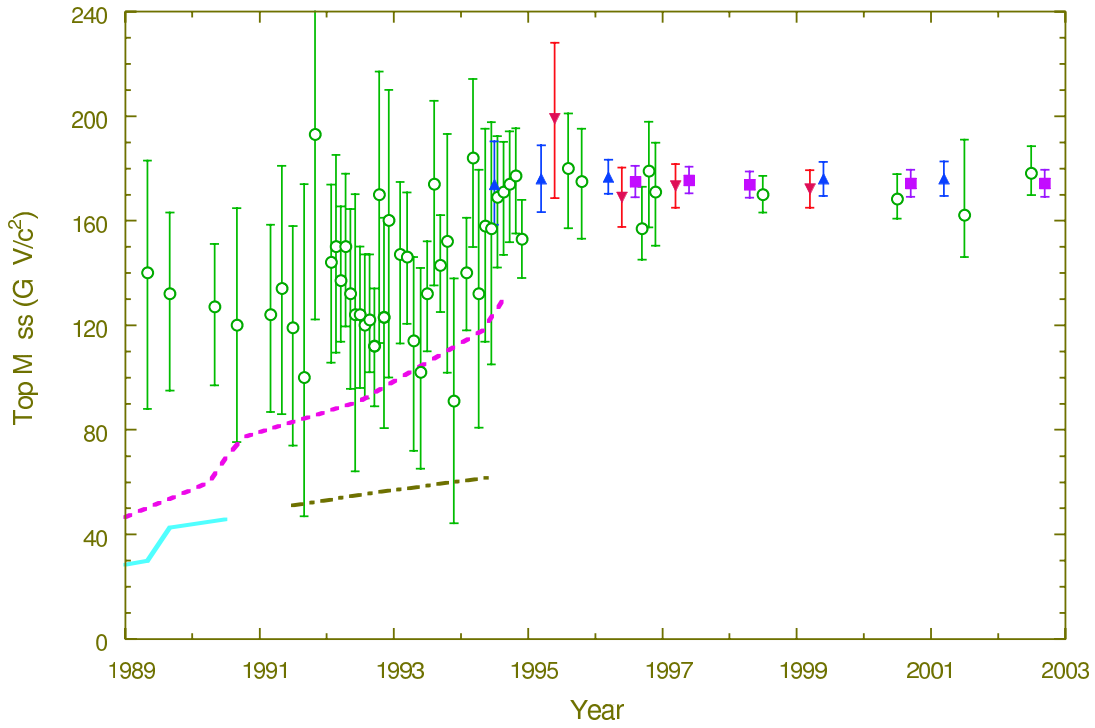


Figure 2.9.: Evolution of the top quark mass prediction and measurement with time [11]. Until 1995 only predictions from electroweak fits (o) have been done. These are consistent with the direct observation by CDF (\blacktriangle) and DØ (\blacktriangledown). The world average from both experiments is also shown (\blacksquare) as well as the lower bounds from hadron colliders (dashed line) and e^+e^- colliders (solid line).

$$\begin{aligned} f_+ &= 0.11 \pm 0.15 \text{ (CDF)}, \\ f_0 &= 0.56 \pm 0.31 \text{ (D0)}, \end{aligned}$$

which is consistent with the Standard Model.

Charge, Spin, Spin Correlations Although the Standard Model predicts a top mass with charge $+\frac{2}{3}$ and spin $\frac{1}{2}$ these predictions have not been verified yet. Also, no measurement of the spin correlations has been done so far. Due to the heavy mass of the top quark, and the resulting short lifetime, the spin information of the produced $t\bar{t}$ pair is not lost after its decay and can in principle be measured. Feasibility studies for these quantities are in progress.

Weak interaction, $|V_{tb}|$ The weak production processes described earlier allow a direct measurement of the Cabbibo-Kobayashi-Maskawa (CKM) matrix element $|V_{tb}|$. So far it has only been estimated from three-generations unitarity constraints ($|V_{ub}|^2 + |V_{cb}|^2 + |V_{tb}|^2 = 1$) plus assuming three generations using the measurements of the lighter elements, yielding a result of

$$|V_{tb}| = 0.97^{+0.16}_{-0.12} (> 0.75 \text{ 95\% CL}) \text{ (3 generations)}. \quad (2.6)$$

The cross sections of the “single top” processes are proportional to $|V_{tb}|^2$. So far, only limits have been estimated since the electroweak single top production process has not yet been observed.

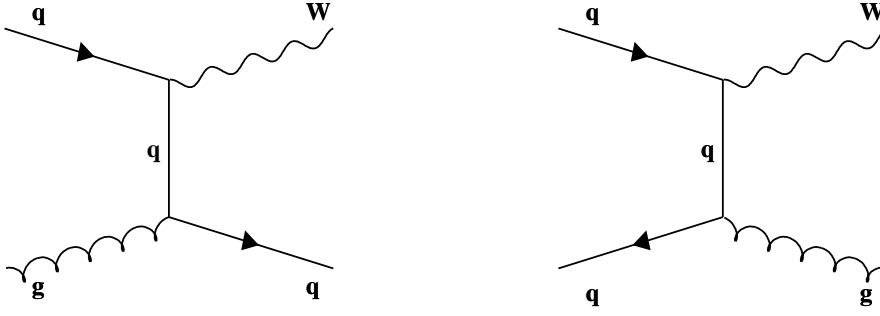
2.2.5. Background Processes

Two sources of background exist for the $l + jets$ channel. These are multijet (or QCD) and $W + 4 jets$ processes.

The former contributes due to processes in which jets are produced and one jet mimics a lepton. This happens more often in case of electrons since it is less likely that a jet fires the muon chambers (except for the case of a heavy-flavor jet with decaying b quark in which a muon is produced but the isolation from the jet is faked). Due to inefficiencies in the detection efficiency not identified jets can lead to missing energy. In this case the same signature as for a neutrino is found. This source of background is also referred to as instrumental background because the final-state is not coming from a physics process but is purely due to misidentification.

In the $W + 4 jets$ case, a W boson is produced which subsequently decays leptonically. The final-state is therefore the same as in case of the $l + jets$ decay channel of $t\bar{t}$ -pairs. The Feynman diagrams for several of these processes are sketched in Figure (2.10).

$W + 1$ jet processes:



$W + 2$ jets processes:

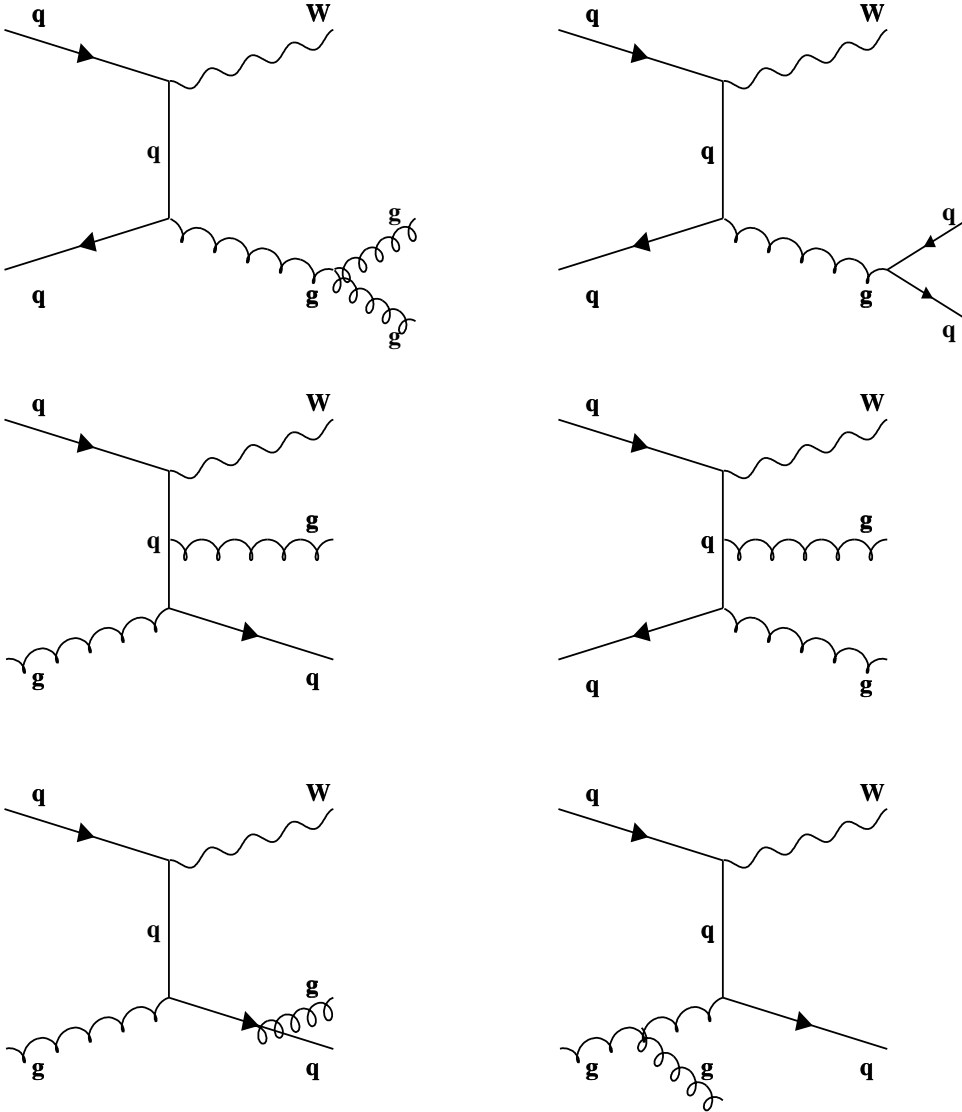


Figure 2.10.: $W +$ jets processes. The first two processes have one jet in the final state, the others have 2 jets. A large variety of contributions are found for 3 and more jet processes.

3. Experimental Setup

The Tevatron is the proton-antiproton collider with the world's highest energy, located at Fermilab in Batavia, Illinois, USA, with a circumference of 6.4 km. Two experiments, CDF and DØ, have taken data during the first run-period (Run I) from 1992 to 1996 at a center-of-mass energy of $\sqrt{s} = 1.8$ TeV. An integrated luminosity of $\int \mathcal{L} \approx 120 \text{ pb}^{-1}$ was collected during that time. A highlight in the history of the Tevatron is the discovery of the top quark by both collaborations, CDF and DØ.

The Tevatron and the detectors were upgraded during the time from 1996 and 2001. The center-of-mass energy of the Tevatron has been increased to $\sqrt{s} = 1.96$ TeV and the experiments were upgraded significantly. In the beginning of 2001 the Tevatron and both experiments entered the second data-taking period (Run II). So far, both experiments collected an integrated luminosity of $\int \mathcal{L} \approx 150 - 200 \text{ pb}^{-1}$ in Run II.

This chapter describes the Tevatron, the DØ experiment and its detector components with emphasis on the upgrades for the Run II.

3.1. The Tevatron Accelerator

A sketch of the accelerator complex is displayed in Figure (3.1). The protons, produced from hydrogen, are accelerated by a Cockroft-Walton accelerator and a Linac. A Booster brings the protons to an energy of 8 GeV after which they are transferred into the main injector. Here, the protons are accelerated to 150 GeV and brought into a bunch structure. Afterwards, one part of the protons is injected into the Tevatron and accelerated to 980 GeV. The other part is used to produce antiprotons by directing a 150 GeV beam of protons into a nickel/copper target. The antiprotons are subsequently accelerated to 8 GeV and accumulated. From there they are transferred into the main injector and accelerated to 150 GeV. Like the protons they are injected into the Tevatron in which they gain their final energy of 980 GeV.

The protons and antiprotons come in 36 bunches with a bunch spacing of 396 ns. These are grouped in three super-bunches (of 12 bunches each) with a gap of $2 \mu\text{s}$. In principle six interaction points are marked, with CDF and DØ being located at two of those.

A detailed description of the Tevatron can be found in [12].

3.2. The DØ Detector

The DØ detector is a multi-purpose detector with emphasis on the identification of leptons and jets. It consists of several subsystems, namely the tracking system, the calorimeter system and the muon system. Additionally, a newly built Forward Proton Detector (FPD) and luminosity monitors complete the detector. The trigger system consists of three levels which account for a rate to tape of 50 Hz in the data acquisition. Figure (3.2) shows a cross sectional view of the detector. The most important upgrade in the Run II is the installation of a complete tracking

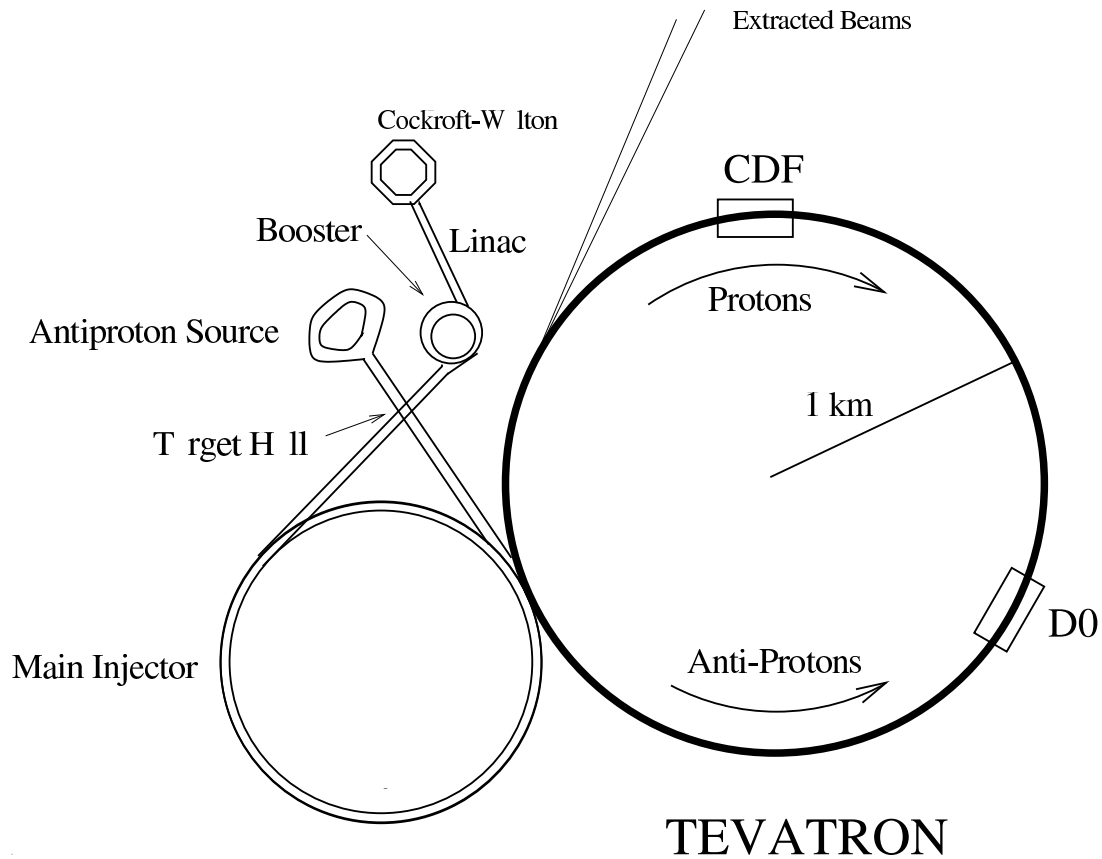


Figure 3.1.: Sketch of the accelerator complex. The production of protons and antiprotons is described in the text, as well as the acceleration chain.

system including a 2 Tesla solenoid magnet. The main components are described in the following. Details, especially on the components not introduced, like the luminosity monitor or the Forward Proton Detector, can be found in the literature [13, 14].

The $D\bar{O}$ coordinate system is right-handed with the z -coordinate along the proton direction and the x -component pointing towards the center of the ring. As common in hadron-colliders, polar coordinates are used:

$$\begin{aligned} r &= \sqrt{x^2 + y^2}, \\ \phi &= \tan^{-1} \frac{x}{y}, \\ \eta &= -\ln \tan \frac{\theta}{2}. \end{aligned}$$

The latter variable is the pseudo-rapidity which is chosen because in QCD the particle multiplicity is flat in η and $\Delta\eta$ intervals are Lorentz-invariant. Since it is often necessary to describe the coordinates of particles with respect to the primary vertex or the center of the detector, η will be referred to as “physics η ” or “detector η ”.

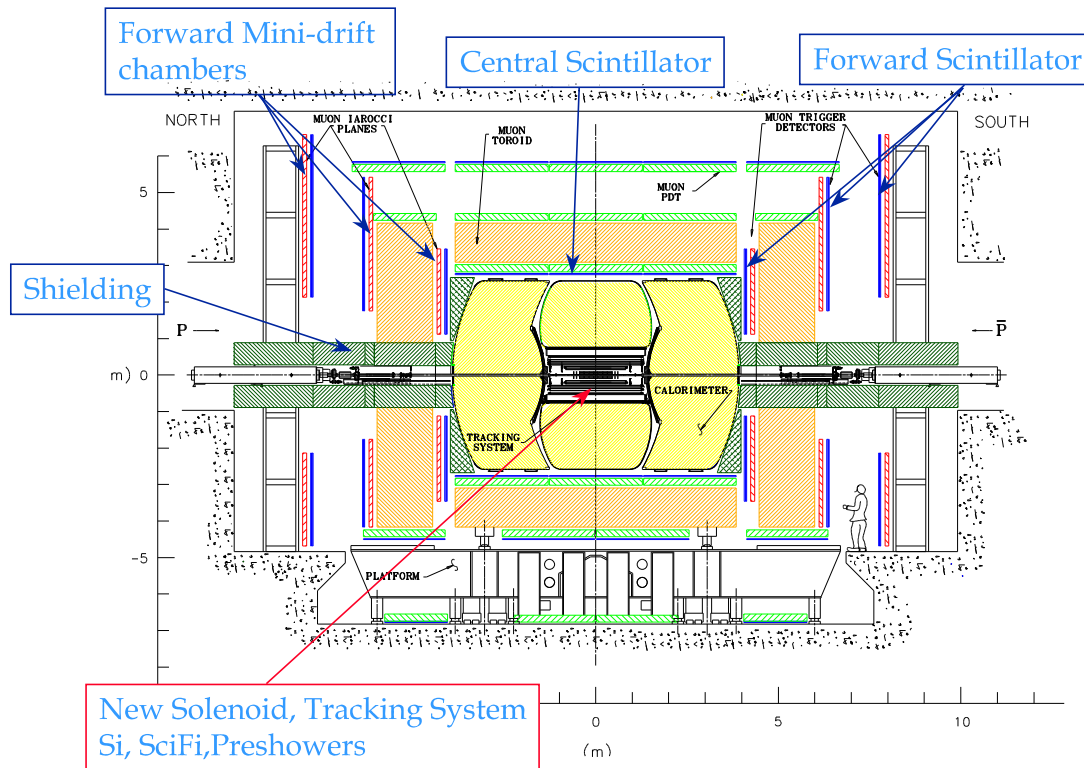


Figure 3.2.: Longitudinal cross section of the DØ detector. It consists of a tracking system in the center, a calorimeter system and a muon system. The upgraded components are explained by the labels.

3.2.1. The Tracking System

The tracking system consists of a silicon vertex detector, a central fiber tracker and the solenoid magnet. Particles with a charge different from zero are bent around the z -axis due the presence of the magnetic field. The radius of the helix is proportional to the transverse momentum $p_T = \sqrt{p_x^2 + p_y^2}$ of the particle:

$$r \text{ [m]} = \frac{p_T \text{ [GeV/c]}}{0.3 \cdot B \text{ [T]}} \quad (3.1)$$

The measurement of the 3-dimensional momentum is completed by additionally measuring the z -component in the $(r - z)$ -plane or η of the track.

Figure (3.3) shows a zoomed cross section of the tracking system. The silicon vertex detector is close to the beam line, followed by the central fiber tracker. Both are surrounded by the solenoid.

Silicon Vertex Detector

The Silicon Vertex Detector (SMT or SVX) is composed of barrels and disks. Figure (3.4) shows a 3-D drawing of the detector.

The barrels are each 12 cm long and have 4 radial layers, with the outer layers in barrel 1 and 3 being single-sided, layers 2 and 4 as well as the inner layers 1 and 3 being double-sided.

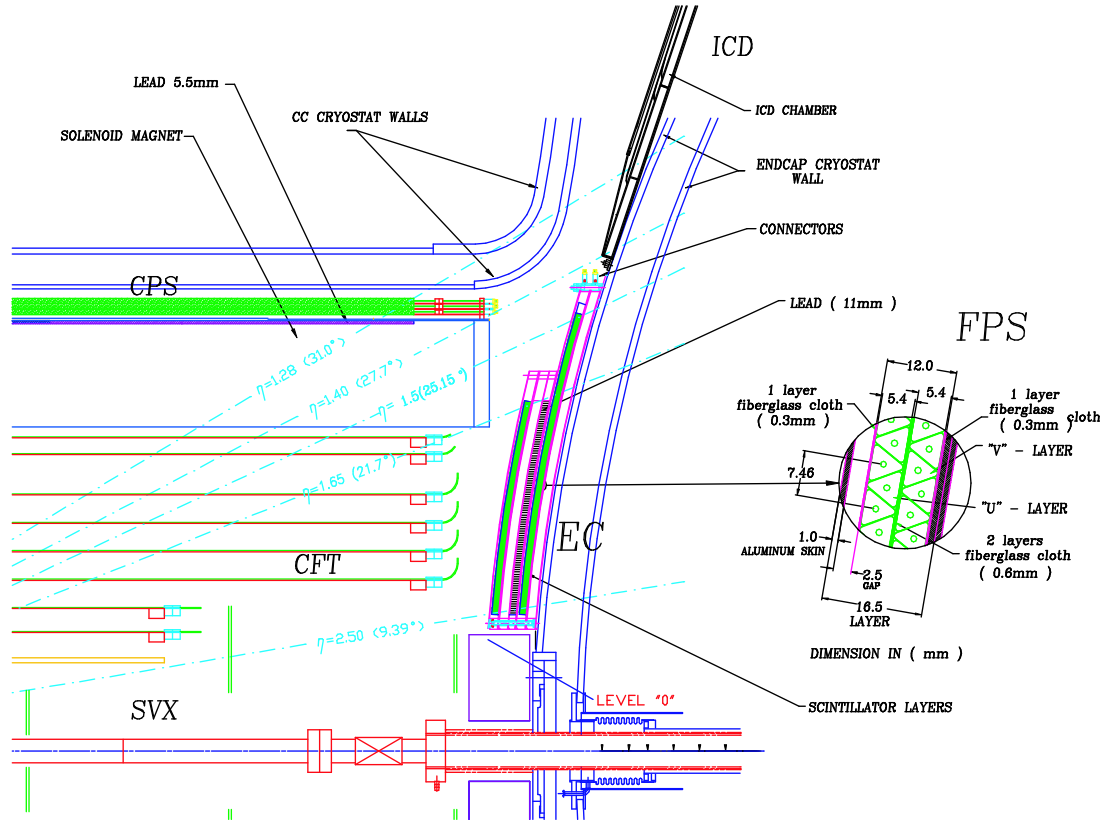


Figure 3.3.: Zoomed cross section of the DØ tracking system. The silicon vertex detector is close to the beam line, followed by the central fiber tracker. Both are surrounded by the solenoid.

The disks come in two types, the “F”-disks with 12 double-sided segments of 30° stereo and the larger “H”-disks with 24 single-sided segments of 15°. The sensor itself is a silicon microstrip detector, 300 μm thick, which is kept at a temperature of 10°C in order to reduce the risk of damage due to radiation. Assembled, the detector measures 2.30 m in z-direction and has radii between 10.5 cm (“F”-disks) and 26.0 cm (“H”-disks). Tracking within a region of $|\eta_{det}| < 3.0$ is possible with a spatial resolution of

$$\begin{aligned}\sigma_{point} &\sim 10 \mu\text{m}, \\ \sigma_{vertex} &\sim 40 \mu\text{m} (r - \phi), \\ &\sim 100 \mu\text{m} (r - z),\end{aligned}$$

where the barrels are used to measure in the $(r - \phi)$ -plane, the disks in the $(r - z)$ -plane. A total of 793,000 readout channels is needed for the vertex detector.

A cross section of the barrel and disks is shown in Figure (3.5). More details on the silicon tracker can be found in the literature cited above.

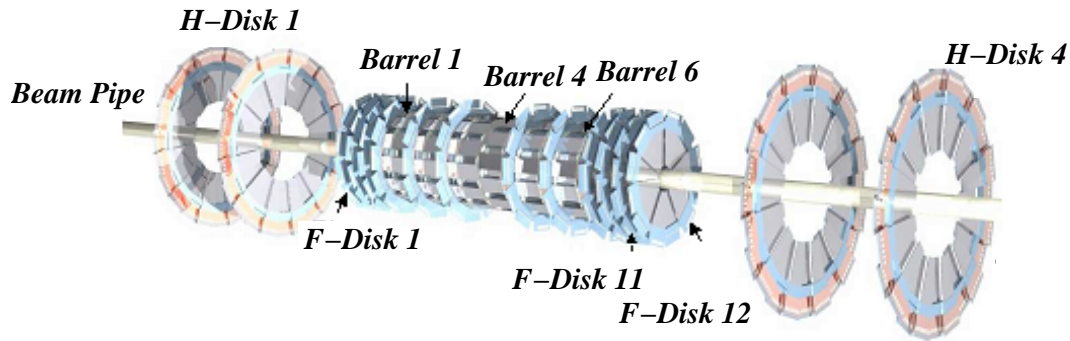


Figure 3.4.: Three-dimensional drawing of the Silicon Vertex Detector. The arrangement of barrels and disks can be seen.

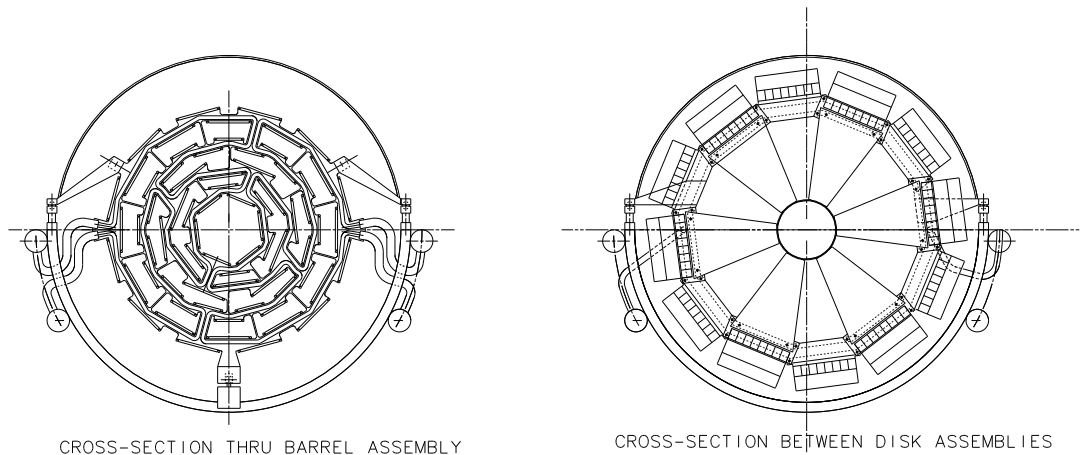


Figure 3.5.: Cross sectional view on the Silicon Vertex Detector. **Left:** Barrels, **right:** Disks.

Central Fiber Tracker

The Central Fiber Tracker (CFT) is located between the Silicon Vertex Detector and the Solenoid (see Figure (3.3)). It is used for momentum measurement and track reconstruction within a range of $|\eta_{det}| < 2.0$. It is also used to provide fast L1 track triggering within a range of $|\eta_{det}| < 1.6$.

The fibers are mounted on cylinders of radii between 19.5 cm and 51.5 cm in axial doublet layers. Odd numbered cylinders have two additional 2° to 3° stereo doublet layers. A total of 74,000 fibers, double cladded with a diameter of $835 \mu\text{m}$, is used. Approximately 10 m of light guide transfer the light to the “Visible Light Photon Counters” (VLPC). Those are a variant of solid-state photomultipliers with high quantum efficiency at high rates.

The spatial resolution of the fiber tracker is $\sigma \sim 100 \mu\text{m}$.

Solenoid Magnet

The superconducting solenoid magnet [15] is 2.7 m in length and provides a magnetic field of 2 Tesla. It has a two layer coil with a mean radius of 60 cm. The uniformity of the field is measured to be 0.5%. The magnet is operated at a temperature of 10 K.

3.2.2. The Calorimeter System

The calorimeter system consists of a uranium liquid argon calorimeter, preshower detectors and the intercryostat detector. It is used to measure the energy of particles from their interaction with matter. This is especially true for leptons and jets with the exception of muons and neutrinos. The former deposit only a tiny fraction of energy in the calorimeter because they are minimal ionizing particles (MIPs). The latter are not at all measured in the detector due to the weak interaction.

Uranium Liquid Argon Calorimeter

The uranium liquid argon calorimeter is divided into three parts, a central calorimeter (CC) and two end caps (EC). The central calorimeter is further parted into an electromagnetic (CEM), fine hadronic (CCFH) and coarse hadronic (CCCH) section. The endcaps are segmented into electromagnetic (ECEM), inner hadronic (ECIH), middle hadronic (ECMH) and outer hadronic (ECOH). The central calorimeter covers a region of $|\eta_{det}| < 1.3$; together with the end caps a total region of $|\eta_{det}| < 4.2$ is covered.

The electromagnetic and hadronic sections have 4 cylindrical floors (EM1 - EM4 and FH1 - FH3 and CH, respectively). The calorimeter is divided into lateral segments of $0.1 \times 2\pi/64 \simeq 0.1 \times 0.1$ in η and ϕ , except for the EM3 floor which has a 2-times larger granularity. Figure (3.6) shows a cross section of the calorimeter in z-direction. Here, the central region and endcaps together with the corresponding floors (and cells) are drawn.

An example for a calorimeter module is shown in Figure (3.7). A signal board, which measures the deposited energy, is sandwiched by uranium plates with argon gaps inbetween. Particles traversing such a module deposit energy in the dense uranium absorber in which showers develop. The subsequent ionization in the argon is measured by the signal boards. The ratio between electromagnetic and hadronic response is approximately 1, i.e. the calorimeter is compensating.

Details on the calorimeter upgrade can be found in [16].

Preshower and Intercryostat Detector

The Central Preshower Detector (CPS) is situated between the solenoid and the central calorimeter, the Forward Preshower (FPS) in front of the endcaps. Both are used to increase the electron-identification efficiency and recover the energy resolution due to the solenoid. The central preshower is made of three layers of scintillator from which one is axial and two are 23° stereo layers. They are installed in the central region $|\eta_{det}| < 1.2$. In order to induce showers with high efficiency a thin lead plate is placed in front of the fiber layers. The light signal is guided and read out the same way as the central fiber tracker. The spatial resolution is roughly $\sigma \sim 600 \mu\text{m}$. The design reports for both preshower detectors are found in [17, 18].

The Intercryostat Detector (ICD) is located in front of the endcap in order to increase coverage between central calorimeter and endcap. It consists of a ring of scintillating counters with a segmentation of $\Delta\eta \times \Delta\phi = 0.1 \times 0.1$.

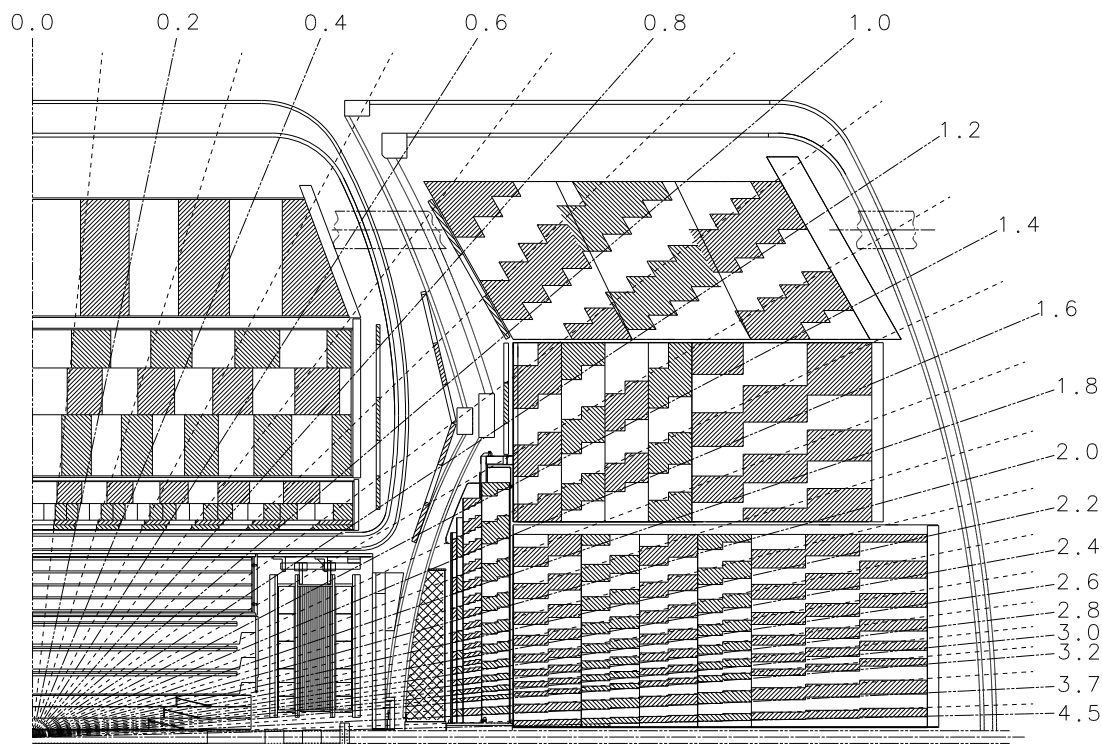


Figure 3.6.: Cross section of the calorimeter. The central calorimeter and the endcaps are drawn together with the corresponding floors and cells.

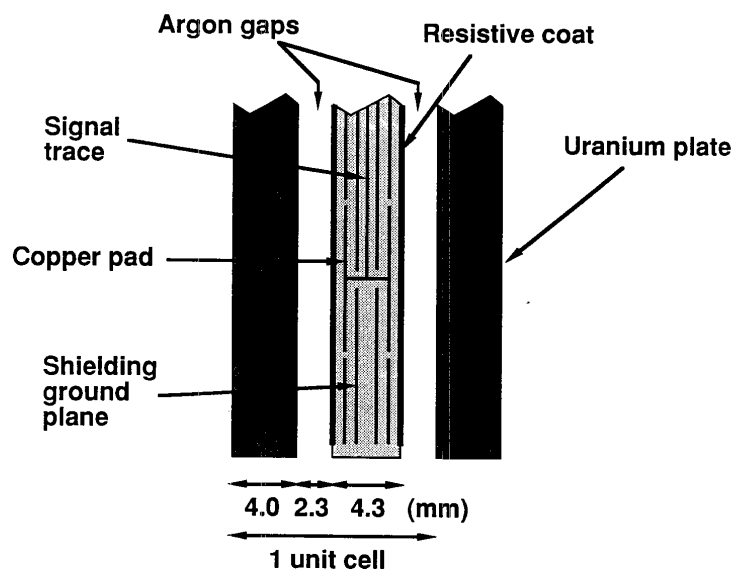


Figure 3.7.: Unit cell of the calorimeter. The showering is caused in the uranium plate. The ionization in the argon gaps is measured by the signal board sandwiched inbetween.

Energy Resolution

Since a calorimeter counts ionized particles, the error on the measured energy is proportional to the number of particles observed in the detector cluster. The number of particles N can fluctuate with Poisson errors, i.e. $\Delta N \propto \sqrt{N}$. Therefore, the relative resolution of the energy measurement is

$$\frac{\Delta E}{E} \propto \frac{\Delta N}{N} = \frac{1}{\sqrt{N}} \propto \frac{1}{\sqrt{E}}. \quad (3.2)$$

Emperically, the resolution is parameterized as

$$\left(\frac{\Delta E}{E}\right)^2 = C^2 + \frac{S^2}{E} + \frac{N^2}{E^2}. \quad (3.3)$$

The constants C , S and N correspond to calibration errors (C), sampling fluctuation(S) and noise contributions (N). The values for those quantities yielded in test-beam experiments with electrons and pions are summarized in Table (3.1).

Particle	C	S [$\sqrt{\text{GeV}}$]	N [GeV]
e	0.014	0.135	0.14
π	0.032	0.410	1.30

Table 3.1.: Parameters for the calorimeter resolution obtained in test-beam experiments with electrons and pions.

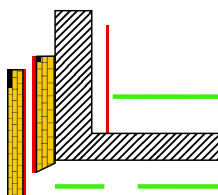
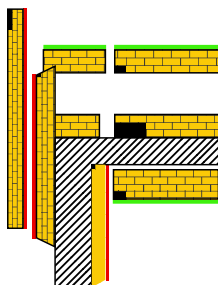
3.2.3. The Muon System

The Muon System consists of a central and a forward part. The central muon system consists of three layers (A, B, C) of Proportional Drift Tubes (PDTs) and a layer of scintillator covering a region of $|\eta_{det}| < 1.0$. The forward muon system consists of three layers (A, B, C) of Mini Drift Tubes (MDT) and extends the coverage to $|\eta_{det}| < 2.0$. The layers of scintillator are used for muon triggering and rejection (of cosmis muons for example). A toroidal magnet with a field of 1.8 Tesla allows the measurement of the muon momentum. The A layers of the central and forward region are found between the calorimeter and the toroid, the B and C layers are located outside the magnet.

Figure (3.8) shows a sketch of the muon system. More details can be found in [19, 20, 21].

3.2.4. Trigger

Since at hadron-colliders far too many events occur than can be recorded by the data aquisition, a trigger must filter events online. At the Tevatron every 396 ns bunches of protons are colliding with bunches of antiprotons. This translates into a rate of about 2.5 MHz where, in comparison, the offline reconstruction can only handle rates of 50 Hz. Therefore only events are kept that are interesting from a physics point of view. At DØ the trigger is divided into three levels (1 to 3) which are explained in the following. Figure (3.9) shows diagrammatically the procedure of accepting or rejecting events with the current trigger system.



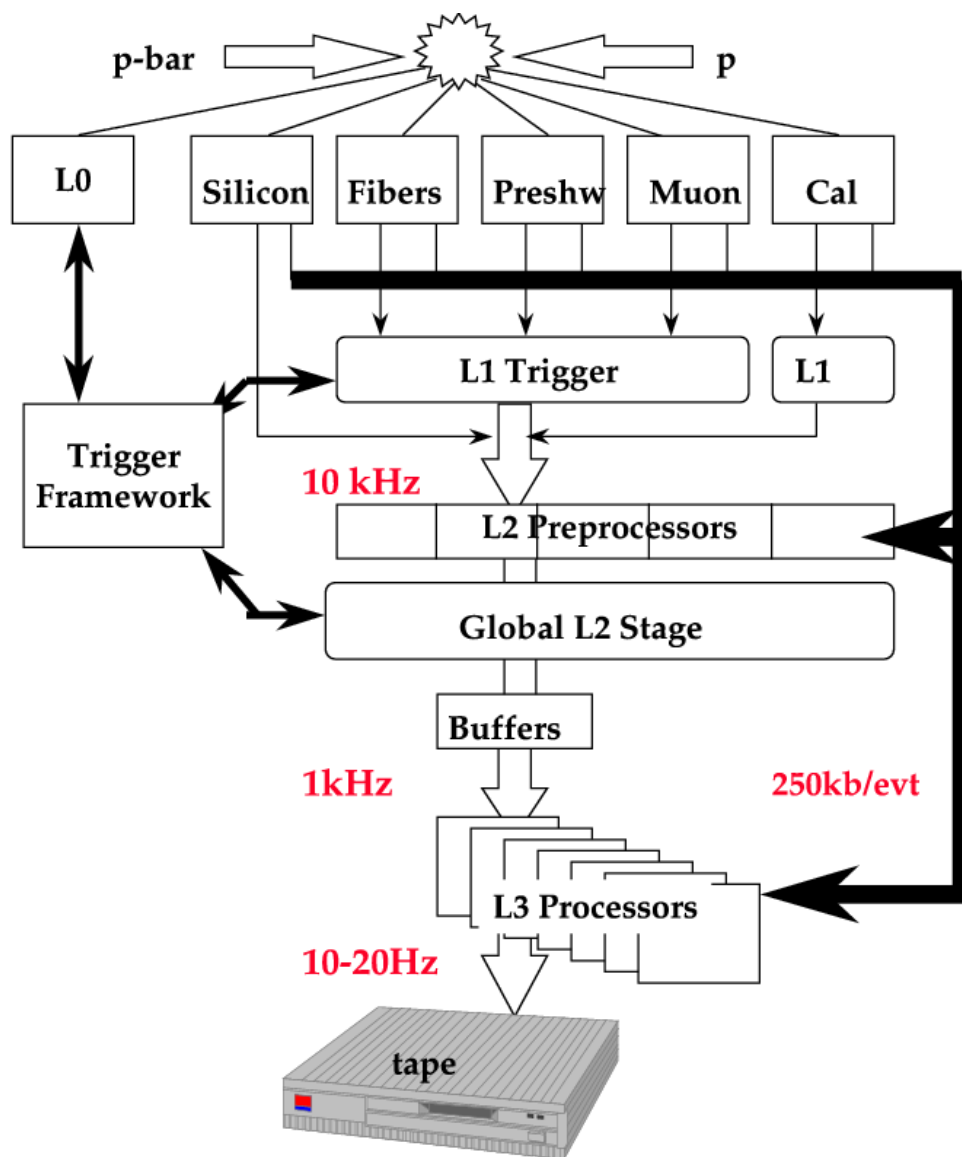


Figure 3.9.: The three-level process of triggering at DØ. The event rates are reduced step by step.

4. The Matrix Element Method

The main principle of the matrix element method is the calculation of the probability for each event to be produced in certain processes (here the $t\bar{t}$ signal and the $W + 4 \text{ jets}$ background processes) given its measured kinematics. A 2-dimensional likelihood is built from these two probabilities treating the mass of the top quark and the fraction of top events as parameters to be estimated. Using a maximum likelihood method, the relative fraction of signal and background events (the purity of the sample) and the mass of the top quark are extracted. Two processes are considered for the event probability determination: the $t\bar{t} \rightarrow l\nu + \text{jets}$ processes using a MADGRAPH matrix element [22, 23, 24] and the $W(\rightarrow l\nu) + \text{jets}$ processes calculated with a VECBOS matrix element [25].

In the following a general expression for the event probability is derived, taking into account the measurement process. Subsequently, the estimation of parameters is introduced and applied to the measurement of the top quark mass.

4.1. The Differential Cross Section as a Measure of the Production Probability

The probability for any scattering or decay process is proportional to its differential cross section. An interaction with an n-body final-state can be written as $q_1 + q_2 \rightarrow p_1 + \dots + p_n$, where q_1 and q_2 are the 4-momenta of the initial-state particles and p_1 to p_n are those of the final-state particles. In the $q_1 q_2$ rest frame, the differential cross section σ_{hs} (where the subscript “hs” refers to the hard scattering process as will be explained later) is given by Fermi’s Golden Rule:

$$d^m \sigma_{hs}(\mathbf{x}; \mathbf{a}) = \frac{(2\pi)^4 |\mathcal{M}(\mathbf{x}; \mathbf{a})|^2}{4\sqrt{(q_1 \cdot q_2)^2 - m_1^2 m_2^2}} \cdot d\Phi_n. \quad (4.1)$$

Here, \mathcal{M} is the matrix element for the given process, m_1, m_2 are the masses of the initial-state particles and $d\Phi_n$ is an element of the n-body phase space. The latter can be written as

$$d\Phi_n(q_1 + q_2; p_1, \dots, p_n) = \delta^{(4)}(q_1 + q_2 - \sum_{i=1}^n p_i) \prod_{i=1}^n \frac{d^3 p_i}{(2\pi)^3 2E_i}. \quad (4.2)$$

The matrix element (which gives the method its name) depends on the kinematics \mathbf{x} of the initial- and final-state particles and describes the reaction. It can be written as a function of any set of parameters \mathbf{a} , which in the current analysis is simply the mass of the top quark and the signal fraction (or purity). In QED and pQCD it can be obtained from perturbation theory (in principle up to any order).

As applied here, Fermi’s Golden Rule is only valid for parton interactions. For hadronic interactions it has to be taken into account that the momenta of the composite particles of, for

example, a proton, are not known. For that reason the process described by Equation (4.1) can be referred to as "hard scattering" process since it describes the parton-parton interaction only. In order to obtain the differential cross section for proton-antiproton interactions Equation (4.1) has to be convoluted with the parton density functions (PDF) for each hadron, which parameterize the distribution of longitudinal parton momenta. If x is the fraction of momentum carried by a parton and $f(x)$ is the parton density inside the (anti-)proton then $x \cdot f(x)dx$ is the probability that the parton has a momentum fraction between x and $x + dx$. Due to the different contributions of parton flavors to the (anti-)proton f depends on the type of parton. The corresponding differential cross section is then the sum over all contributions from different parton flavors, which in the case of $t\bar{t}$ production at leading order includes $u\bar{u}$, $d\bar{d}$, $c\bar{c}$, $s\bar{s}$, $b\bar{b}$ and gg :

$$d^n\sigma(\mathbf{x}; \mathbf{a}) = \sum_{i=flavor} \int_{x_1} \int_{x_2} d^n\sigma_{hs}(\mathbf{x}; \mathbf{a}) dx_1 dx_2 x_1 f_i(x_1) x_2 f_i(x_2). \quad (4.3)$$

From this an expression can be derived for the probability of an event to be produced by a certain process with the given kinematics. This expression of course has to be properly normalized. The integral of the differential cross section over the whole available phase space is the total cross section for a given process, i.e.

$$\sigma(\mathbf{a}) = \int d^n\sigma(\mathbf{x}; \mathbf{a}), \quad (4.4)$$

where \mathbf{x} is a vector in multidimensional phase space. Thus, the probability for an event to originate from that process can be written as

$$p(\mathbf{x}; \mathbf{a}) d^n x = \frac{1}{\sigma} d^n\sigma(\mathbf{x}; \mathbf{a}), \text{ with } \int p(\mathbf{x}; \mathbf{a}) d^n x = 1. \quad (4.5)$$

4.2. Detector Resolution

Since the kinematics of partons cannot be measured perfectly in a detector, two effects have to be taken into account when calculating the probability: the finite resolution of the detector and the detection efficiency. The treatment of those influences is discussed in the following.

Finite Energy Resolution

First, partons are not the observed quantities in a detector but jets, which are the hadronized final-states of partons produced in the interaction. The energy and angles of these jets can only be measured with finite resolution. For that reason the probability in Equation (4.5) has to be convoluted with the probability $W(\mathbf{x}, \mathbf{y})$ that a produced vector in phasespace, \mathbf{y} , is measured as a vector \mathbf{x} , i.e.

$$p(\mathbf{x}) = \frac{1}{\sigma(\mathbf{a})} \int d^n\sigma(\mathbf{y}; \mathbf{a}) \cdot W(\mathbf{x}, \mathbf{y}). \quad (4.6)$$

Of course the integration is carried out over the whole available phase space. $W(\mathbf{x}, \mathbf{y})$ is referred to as a transfer function. For each parton it can be factorized into functions of energy, angles and

other kinematic properties. In case of a perfect measurement, $W(\mathbf{x}, \mathbf{y})$ is a delta function, in case of no measurement it is a constant (e.g. for neutrinos, which are not observed in the detector due to the weak interaction). For finite resolutions the transfer function can be parameterized as any function normalized to one with respect to \mathbf{y} .

$$\int d\mathbf{y} W(\mathbf{x}, \mathbf{y}) = 1. \quad (4.7)$$

As is discussed in Chapter 6, the transfer functions depend on the flavor of the corresponding parton. This is due to the fact that, for example, gluons or heavy quarks hadronize differently than light quarks and therefore the behavior of partons varies in the detector. However, they do in principle not depend on the production process, even though the kinematics of the observed final-state particles differ for various processes.

Detector Acceptance and Efficiency

Second, the acceptance, the probability of observing a jet in the detector, is a function of the parton kinematics. Several factors account for the acceptance: detector geometry, trigger efficiency, event selection, reconstruction efficiency, etc. It is not dependent on the type of interaction that produced the parton. For example an electron produced in the leptonic decay of a top quark will have the same detector acceptance as an electron generated in Drell-Yan processes.

In order to make allowance for the events which were not observed in the detector, the normalization factor in Equation (4.4) has to be convoluted with the acceptance.

$$\sigma_{obs}(\mathbf{a}) = \int d^n \sigma(\mathbf{x}, \mathbf{a}) \cdot Acc(\mathbf{x}) \quad (4.8)$$

Combining Equation (4.5) with Equations (4.6) and (4.8) a formula to calculate the event probability for a certain process is obtained:

$$p(\mathbf{x}) = \frac{1}{\int d^n \sigma(\mathbf{x}; \mathbf{a}) \cdot Acc(\mathbf{x})} \int d^n \sigma(\mathbf{y}; \mathbf{a}) \cdot W(\mathbf{x}, \mathbf{y}). \quad (4.9)$$

Final Expression for the Event Probability

So far the probability for an event to be produced by a certain reaction (described by the corresponding matrix element) with observed kinematics \mathbf{x} was derived. Since the observed final state can not always be assigned to a single production process all possible contributions have to be taken into account. Therefore, the total probability for an event to be observed in the final-state is the weighted sum of probabilities of all contributing (non-interfering¹) processes i.

$$p(x) = \sum_i c_i \cdot p_i(x) \quad (4.10)$$

¹For interfering processes the amplitudes have to be added coherently. In case of the previously discussed final states, the processes do not interfere which allows to simply add the probabilities.

Since all probabilities involved are normalized to one, the sum over the coefficients c_i must obey the following sum rule:

$$\sum_i c_i = 1. \tag{4.11}$$

4.3. Estimation of Parameters

The previous section explained how the probability for an event to be produced by a certain process can be calculated. In order to estimate the properties of these processes or of any parton involved, a maximum likelihood method can be applied. For a given set of data (here: event kinematics = lepton and jets 4-vectors) $\mathbf{x}_1, \dots, \mathbf{x}_k$ the likelihood is defined as the product of the individual probabilities:

$$L(\mathbf{x}_1, \dots, \mathbf{x}_k; \mathbf{a}) := \prod_{i=1}^k p(\mathbf{x}_i; \mathbf{a}), \quad (4.12)$$

where \mathbf{a} is a set of parameters which have to be estimated. In order to estimate the most probable value of these parameters the likelihood is calculated for each value of \mathbf{a} . The set \mathbf{a}' that maximizes L is the most probable value for \mathbf{a} . Instead of maximizing L it is common to minimize the negative logarithm of L , which in turn can be written as the sum of logarithms of the individual probabilities:

$$-\ln L = -\sum_{i=1}^k \ln p(\mathbf{x}_i; \mathbf{a}). \quad (4.13)$$

In the context of this analysis \mathbf{a} is a 2-dimensional vector with the components being the top quark mass and the signal fraction (m_{top}, c_1) (in the next section it will be made clear that only two processes are taken into account, one for the $t\bar{t}$ signal, the other for $W + 4 jets$ background).

4.4. Application to $t\bar{t}$ Production and the Measurement of the Top Quark Mass

As discussed earlier, in the case of $t\bar{t}$ production the contributing background processes to the observed final state, i.e. 4 jets, a central lepton and missing transverse energy, are mainly $W + 4 jets$ and QCD multijet events. In the latter case one jet fakes a lepton or, in the $\mu + jets$ channel, the muon comes from a heavy flavor decay. Since there is no reliable matrix element for QCD events with jets faking leptons and because the relative amount of these events only counts up to 7–20% [1], the $W + 4 jets$ events are assumed to be the only source of background in the calculation. The uncertainty in the top quark mass measurement due to QCD events in the sample will be dealt with as a source of systematic uncertainty and is discussed later. From (4.10) it follows that the total production probability can be written as

$$p(\mathbf{x}; m_{top}) = c_1 \cdot p_{t\bar{t}}(\mathbf{x}; m_{top}) + c_2 \cdot p_{W+4jets}(\mathbf{x}) \quad (4.14)$$

where $p_{t\bar{t}}$ is the probability for $t\bar{t}$ production (with lepton + jets in the final state) and $p_{W+4 jets}$ the corresponding probability for $W + 4 jets$. These will be referred to as signal and background probability in the following. Since the mass of the top quark, m_{top} , is the property to be estimated, $p_{t\bar{t}}$ is written as a function of the top mass. From Equation (4.11) it follows that $c_2 = 1 - c_1$. The relative fraction of $t\bar{t}$ events, c_1 , is the second unknown parameter. From this probability a likelihood is constructed and the parameters are estimated using a maximum likelihood method introduced in the pervious section.

The following chapter describes the individual steps of the calculation in more detail.

5. Calculation of Event Probabilities

This chapter describes the calculation of the event probabilities for signal and background processes in case of $t\bar{t}$ production. First, the transfer functions are described briefly (a more detailed discussion about the derivation and parametrization can be found in Chapter 6). Subsequently, the integration of the differential cross section for $t\bar{t}$ and $W + 4 \text{ jets}$ events are explained including a transformation of variables in the former case. Also, numerical techniques and approximations are introduced.

5.1. Transfer Functions

The transfer functions $W(\mathbf{x}, \mathbf{y})$ are used to describe the resolution of the detector, i.e. they are a measure of the probability that an event with kinematics \mathbf{y} is measured as \mathbf{x} . It can be decomposed into a product of functions for each parton. In this analysis, the momentum of the charged lepton is assumed to be measured perfectly. Also, the angles of the produced partons (measured as jets) will be treated as measured without uncertainty (see Chapter 6 for details). The following decomposition is used:

$$W(\mathbf{x}, \mathbf{y}) = \delta^{(3)}(\vec{p}_{l, meas} - \vec{p}_l) \prod_{i=1}^4 W_{jet}^i(E_{jet}, E_{parton}) \prod_{i=1}^4 \delta^{(2)}(\Omega_{jet}^i - \Omega_{parton}^i), \quad (5.1)$$

where $\vec{p}_{l, meas}$ and \vec{p}_l are the momenta of the measured and produced charged lepton, Ω_{jet} and Ω_{parton} are the angles of the jets and the corresponding partons. The functions W_{jet}^i are used to describe the energy resolution and are derived in Chapter 6.

As found to be suitable from the energy distributions ([26] or Chapter 6), a double-gaussian is used as parametrization, where the parameters p_1 to p_5 depend linearly on the parton energy. The transfer functions can be written as

$$W_{jet}(E_{jet}, E_{parton}) = \frac{1}{\sqrt{2\pi}(p_2 + p_3 \cdot p_5)} \left(e^{\frac{-(\delta - p_1)^2}{2 \cdot p_2^2}} + p_3 \cdot e^{\frac{-(\delta - p_4)^2}{2 \cdot p_5^2}} \right), \quad (5.2)$$

where

$$\delta = E_{jet} - E_{parton}, \quad (5.3)$$

$$p_i = a_i + E_{parton} \cdot b_i. \quad (5.4)$$

The parameters used in this analysis are summarized in Tables (6.2) to (6.4). The derivation of the transfer functions is described in Chapter 6.

5.2. Calculation of the Signal Probability

The calculation of the signal probability requires knowledge of the kinematic properties of the particular reaction under study. As mentioned above, these properties are reflected in the matrix element (or transition amplitude) for that process. In perturbative theories the amplitude can be decomposed into matrix elements of the same order, for example in QED. There, the perturbation parameter α_{EM} is much smaller than 1 ($\alpha_{EM} \sim 1/128$), so terms of higher order are usually a correction to the so called Born level (i.e. first order). Therefore, it is sufficient for most purposes to restrict oneself to the leading (LO) order matrix element. However, QCD is not a purely perturbative theory, but since higher order elements are hard to calculate only the 4-jet leading order matrix element for $t\bar{t}$ -production is used in this analysis. In next-to-next-to-leading order (NNLO) cross section calculations it can be shown that this approximation is valid.

Several approaches for the calculation of the $l + jets$ leading order matrix elements are available. First, an approximation similar to that in the Run I analysis was used. It is based on the calculations of [27] neither including $t\bar{t}$ spin correlations nor the contributions from gluon-gluon fusion (which in Run II accounts to about 15%, compared to approximately 10% in Run I. As mentioned previously this is due to the increased center-of-mass energy of $\sqrt{s} = 1.96$ TeV). An expression for the matrix element can be found in the literature. Second, the ONETOP [28] and MADGRAPH [22, 23, 24] packages were used, which both include the latter features. All three approaches have been tested for the parton level analysis described in the following chapter and found to give similar results. For the analysis of reconstructed Monte Carlo and data, the matrix element used was taken from the MADGRAPH generator package. Because of that, the calculation described in the following refers to that particular matrix element.

5.2.1. Top Quark Mass and Total Cross Section

Since the top quark mass is the parameter under study it has to be taken into account that the decay width of the top quark is a function of its mass. This was done by implementing the calculations described in [29], which include QCD corrections. As can be seen on the left hand side of Figure (5.1) the width increases with increasing top mass.

In order to calculate the total cross section, which is required for the normalization of the top signal event probability, the integral of the differential cross section has to be performed over the whole available phase space. For that purpose a numerical integration method (VEGAS) is used. The calculation was repeated for different values of the on-shell top mass, ranging from 140 GeV/c² to 210 GeV/c². As a result, the total cross section as a function of the top quark mass in leading order is shown on the right hand side of Figure (5.1).

5.2.2. Integration of the Differential Cross Section

In order to calculate the probability for signal events the integrals in Equation (4.9) have to be performed. The phase space for a process $q_1 + q_2 \rightarrow p_1 + \dots + p_n$ with six particles in the final state is 20-dimensional, where 6×3 dimensions account for the 3-momenta of the final-state particles (with masses fixed). Assuming that the transverse momenta of the initial-state partons are zero, 2 dimensions are considered for their longitudinal momenta.

However, energy- and momentum-conservation as well as the measurement of kinematic properties of the interaction reduce the number of integrals to be performed. As described earlier the transfer functions characterize the resolution of the detector. Assuming the jet angles and the charged lepton momentum to be measured perfectly, the integration over those

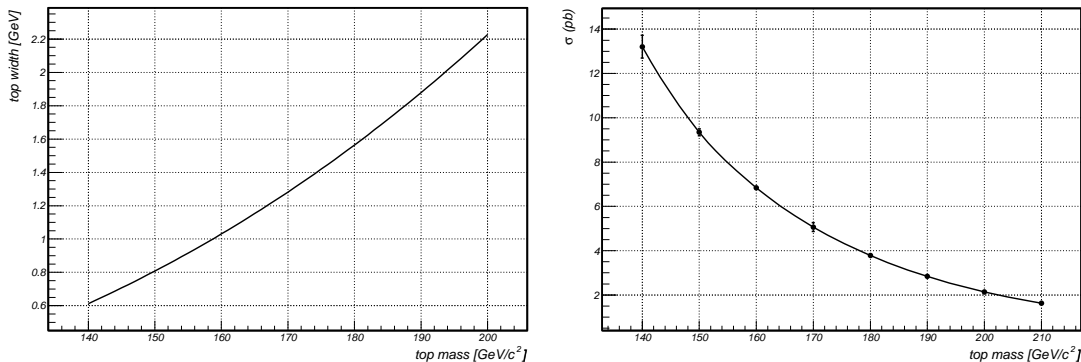


Figure 5.1.: **Left:** Calculated top width as function of the polemass of the top quark. **Right** Total cross section of $t\bar{t}$ production in leading order as function of the polemass of the top quark. The calculation was done using the MADGRAPH matrix element at a center of mass energy of $\sqrt{s} = 1.96$ TeV. As parton density functions the CTEQ5L set is used.

quantities is straight forward due to the delta-functions in Equation (6.1). The same is true for the energy- and momentum-conservation which is intrinsic to the phase space (4.2). By assuming the p_T of the $t\bar{t}$ -system to be zero (i.e. no initial state radiation) the transverse momentum of the neutrino can be calculated by balancing the total momentum. Table (5.1) summarizes the degrees of freedom in this calculation.

Still, the integration has to be carried out over 5 dimensions and is done numerically. It should be mentioned that several approaches have been compared and studied. The following describes the techniques which have been used for the analysis.

D.o.f.	Particles
$6 \times 3 = 18$	final state particles
+ 2	longitudinal momentum of initial-state partons
-4	energy-momentum conservation
-3	lepton measurement
-8	jet angle measurement
= 5	total

Table 5.1.: The degrees of freedom in the $t\bar{t}$ production and decay process.

Transformation of the Phase Space

Using numerical integration techniques the choice of variables of integration should be made such that the sampling is mostly performed in regions with large probability density. In case of $t\bar{t}$ production the probability peaks at the four poles of the top and W masses, arising from the Breit-Wigner terms in the matrix element. Since these terms have narrow widths (~ 1 GeV/c² and ~ 2 GeV/c² respectively) it is even more important because the sampling in 5 dimensions is very time-consuming. Therefore, the set of variables which was not accounted for by the delta-functions, i.e. the momentum of the four jets and the longitudinal momentum of the neutrino, is transformed into a new set: the invariant mass of the hadronic and leptonic top quark (m_{jjb} , $m_{l\nu b}$), the mass of the hadronic W boson (m_{jj}), the absolute value of the up-type light quark momentum (ρ_1) (from the W decay) and the longitudinal momentum of the neutrino (p_ν^z).

The Jacobian resulting from the transformation of variables is derived in Appendix A. The phase space factor $d\Phi_n$ in Equation (4.2), where $n = 6$, is transformed into:

$$\begin{aligned}
\int dp_\nu^x \int dp_\nu^y d\Phi_6 &= \int dp_\nu^x \int dp_\nu^y \delta^{(4)}(q_1 + q_2 - \sum_{i=1}^6 p_i) \prod_{i=1}^6 \frac{d^3 p_i}{(2\pi)^3 2E_i} \\
&= \int dp_\nu^x \int dp_\nu^y \delta^{(4)}(q_1 + q_2 - \sum_{i=1}^6 p_i) \prod_{i=1}^4 \frac{\rho_i^2 d^2 \Omega_i d\rho_i}{(2\pi)^3 2E_i} \cdot \frac{d^3 p_l}{(2\pi)^3 2E_l} \cdot \frac{d^3 p_\nu}{(2\pi)^3 2E_\nu} \\
&= \delta(E_{q_1} + E_{q_2} - \sum_{i=1}^6 E_i) \delta(p_{q_1}^z + p_{q_2}^z - \sum_{i=1}^6 p_i^z) \cdot \Phi_6 \\
&\quad \times \prod_{i=1}^4 d^2 \Omega_i \cdot dm_{jjb}^2 dm_{l\nu b}^2 dm_{jj}^2 d^3 p_l dp_\nu^z,
\end{aligned} \tag{5.5}$$

where

$$\begin{aligned}
\Phi_6 &= \prod_{i=1}^4 \frac{\rho_i^2}{(2\pi)^3 2E_i} \cdot \frac{1}{(2\pi)^3 2E_e} \frac{1}{(2\pi)^3 2E_\nu} \\
&\quad \times \frac{1}{2(E_2 \frac{\rho_3}{E_3} - \rho_2 \cos \theta_{23} + E_1 \frac{\rho_3}{E_3} - \rho_1 \cos \theta_{13})} \\
&\quad \times \frac{l}{2(E_\nu \frac{\rho_4}{E_4} - \rho_\nu \cos \theta_{\nu 4} + E_l \frac{\rho_4}{E_4} - \rho_l \cos \theta_{l4})} \\
&\quad \times \frac{1}{2(E_1 \frac{\rho_2}{E_2} - \rho_1 \cos \theta_{12})}
\end{aligned} \tag{5.6}$$

and 1, ..., 4 refer to the two light (up-type 1, down-type 2) and two b quarks (hadronic 3, leptonic 4) with $\rho_i = |\vec{p}_i|$. Here, the integration over the transverse momentum of the neutrino was carried out, so the following terms have to be taken at the calculated values of p_ν^x and p_ν^y .

Constraints on the Integration

Together with Equations (5.5) and (5.6) the differential cross section (including the transfer functions) can be written as

$$\begin{aligned}
d^n \sigma(\mathbf{x}; m_{top}) &= \int d^n \sigma_{hs}(y) dx_1 dx_2 x_1 f(x_1) x_2 f(x_2) \cdot W(\mathbf{x}, \mathbf{y}) \\
&= \int d\Phi_6 dx_1 dx_2 \frac{(2\pi)^4 |\mathcal{M}(\mathbf{y}; m_{top})|^2}{4\sqrt{(q_1 \cdot q_2)^2 - m_1^2 m_2^2}} x_1 f(x_1) x_2 f(x_2) \cdot W(\mathbf{x}, \mathbf{y}) \\
&= \int dx_1 dx_2 \prod_{i=1}^4 d^2 \Omega_i \cdot dm_{jjb}^2 dm_{l\nu b}^2 dm_{jj}^2 d^3 p_l dp_\nu^z \\
&\quad \times \delta(E_{q_1} + E_{q_2} - \sum_{i=1}^6 E_i) \delta(p_{q_1}^z + p_{q_2}^z - \sum_{i=1}^6 p_i^z) \\
&\quad \times \frac{(2\pi)^4 |\mathcal{M}(\mathbf{y}; m_{top})|^2}{4\sqrt{(q_1 \cdot q_2)^2 - m_1^2 m_2^2}} x_1 f(x_1) x_2 f(x_2) \cdot W(\mathbf{x}, \mathbf{y}),
\end{aligned} \tag{5.7}$$

where this formula has to be summed over all flavor contributions of parton flavors in the proton.

As mentioned above the transverse component of the initial-state particles is assumed to be zero. By integrating over x_1 and x_2 the two delta-functions in Equation (5.7) vanish. After inserting the transfer functions and integrating over the angles of the jets and the momentum of the lepton, the above equation simplifies to

$$d^n\sigma(m_{top}) = \int dm_{jjb}^2 dm_{l\nu b}^2 dm_{jj}^2 d\rho_1 dp_\nu^z \frac{(2\pi)^4 |\mathcal{M}(\mathbf{y}; m_{top})|^2}{4|\vec{q}_1||\vec{q}_2|} \cdot \Phi_6 \\ \times x_1 f(x_1) x_2 f(x_2) \cdot \prod_{i=1}^4 W_{jet}(E_{jet}, E_{parton}), \quad (5.8)$$

where the masses of the initial-state particles are neglected.

Parton Density Functions

Since the matrix element used for the calculation is of leading order the set of parton density functions is also chosen to be of leading order. Therefore, any double counting or other inconsistency are avoided. Throughout the analysis the CTEQ5L set is used. Uncertainties in the mass measurement due to the choice of PDFs are discussed in the Chapter 8 on systematic uncertainties.

Performing the 5-Dimensional Integration

The integrals in Equation (5.8) are performed numerically. Since multidimensional integrations are time-consuming three integrals are calculated using valid approximations explained in the following.

The matrix element for $t\bar{t}$ -production contains Breit-Wigner terms for both, the top quark and the W boson. Since the decay widths of both particles are very small ($\mathcal{O}(2 \text{ GeV})$) the Breit-Wigner terms can be approximated by the narrow width approximation [30], i.e. treating these terms as delta-distributions:

$$\frac{1}{(p^2 - m^2)^2 + (m\Gamma)^2} \xrightarrow{\Gamma \rightarrow 0} \frac{\pi}{m\Gamma} \delta(p^2 - m^2), \quad (5.9)$$

where in this case p^2 is the invariant mass square of a particle, m its polemass and Γ the corresponding decay width.

Thus, the number of dimensions is decreased by three. The integration over ρ_1 and p_ν^z is carried out by scanning over the $\rho_1 - p_\nu^z$ -plane in an appropriate step size using a 2-dimensional Simpson algorithm. This procedure is described in more detail in Appendix B. Also, other numerical methods (adaptive and gaussian integrations; the implementations can be found in the CERN library [31]) were used and compared, but found to be insufficient in terms of CPU time with the chosen binning. As will be made clear in the appendix, the integration is a trade-off between CPU time and accuracy.

5.2.3. Jet-Parton Assignments and Multiple Solutions

The expression for the signal probability was derived from the differential cross section using the matrix element and phase space for $t\bar{t}$ production. The input variables for these formulae

are the 4-momenta of the final-state particles. Since in case of the jets it is not possible to mark a particular jet with a certain flavor, all $(4 \times 3 \times 2 \times 1 =) 24$ possible jet parton combinations have to be taken into account. Technically, the integral in Equation (5.8) is carried out for all permutations and averaged. Techniques like b-tagging could reduce the number of combinations, but are not yet used in this analysis. This issue is discussed in Chapter 9.

Since the longitudinal momentum of the neutrino is a variable of integration, the kinematic equations dealt with during the calculations can be solved by more than one constellation of kinematics. In that case all possible solutions are averaged. The way the kinematic equations are solved in the analysis is described in Appendix C.

5.2.4. Acceptance for $t\bar{t}$ Events

As mentioned in the previous section, the probability has to be normalized properly. This is accomplished by the prefactor in Equation (4.9). To calculate the denominator the term

$$N(m_{top}) = \int Acc(\mathbf{x}) d^n \sigma(\mathbf{x}; m_{top}) \quad (5.10)$$

has to be calculated. However, N can be decomposed into the total cross section and the average acceptance. Clearly, the latter does not depend on the kinematic properties of single jets but can be parameterized as a function of the top quark mass. One can show that the following equation holds:

$$\langle Acc \rangle (m_{top}) = \frac{1}{\sigma(m_{top})} \cdot \int Acc(x) d^n \sigma(\mathbf{x}, m_{top}) = \frac{N_{obs}}{N_{gen}}, \quad (5.11)$$

where N_{obs} and N_{gen} are the number of observed and generated events, respectively. The event selection in case of data and Monte Carlo is discussed in the following section. As an example, Figure (7.12) shows the average acceptances for the muon and electron channel as a function of the top quark mass. The points are obtained from Monte Carlo samples with different polemasses for the top quark. A 2^{nd} order polynomial is fitted to the points and used as parameterization. As expected, the acceptance increases with increasing polemass. Geometrically, this is due to the fact that for higher top masses the final-state particles are more central, whereas in case of light top quarks the decay particles are boosted in the direction of the intermediate gluon (usually $x_1 \gg x_2$ or $x_1 \ll x_2$). The average acceptance used in this analysis is described in Chapter 7.

5.3. Calculation of the Background Probability

In principle, the background probability is calculated in the same way as the signal probability, i.e. Equation (4.9) is the starting point. However, the technical implementation, the matrix element and the integration technique (together with the variables of integration), is different.

As mentioned earlier, the background is assumed to consist of events from $W + 4 \text{ jets}$ processes only. For that reason, the VECBOS [25] matrix element was used in the calculation of the probability. Since no reliable Monte Carlo generator for QCD (or multijet processes) exists, these background contributions have to be dealt with as a systematic uncertainty. Because multijet processes behave like $W + 4 \text{ jets}$ events it is adequate to use the $W + 4 \text{ jets}$ matrix element for the description.

In Chapter 7 ensemble tests are done in order to test the method on data sets according in size to that measured by the experiment. For these ensemble tests a small fraction of QCD events ($\sim 7\% - 20\%$) taken from data is added to the background.

5.3.1. Integration of the Differential Cross Section

Similar to the signal probability, the integration has to be performed over the 20-dimensional phase space. Again, energy- and momentum-conservation as well as the assumption of a perfect measurement of the jet angles and the lepton momenta reduces the number of dimensions to five. Numerical methods are used to carry out the integrations.

Since, apart from the Breit-Wigner of the W boson, no sharp peaks occur in the matrix element for $W + 4 \text{ jets}$ processes, no transformation of integration variables is done. The narrow width approximation, introduced in the previous section, cannot be applied here. Instead, the integration over the energies is done using a simple hit and miss algorithm, where the transfer functions are interpreted as probability densities. The integration over the longitudinal momentum of the neutrino is performed by a gaussian quadrature method (CERNLIB). More details on the integration in case of the background probability can be found in the appendix B.

As in the case of the signal probability, all 24 combinations of jet parton assignments are taken into account. Also, the acceptance for $W + 4 \text{ jets}$ is calculated using Equation (5.11). Because it is not dependent on the top quark mass, a constant value is found for the corresponding event selection.

6. Derivation of the Transfer Functions

As outlined in the previous chapter, the transfer functions are used to describe the mapping between produced and measured quantities. The following chapter motivates the decomposition into several adequate variables and explains the derivation of the functions. Also, the additional corrections applied to jets are briefly discussed. Details on the issue of transfer function are found in [26].

In the initial phase of this analysis the derivation of the transfer functions was done for the p13 reconstruction version. Alan Magerkurth, University of Michigan, has continued this work for the p14 reconstruction version in context of the $D\bar{O}$ mass analysis [26].

6.1. General Parameterization

The transfer functions $W(\mathbf{x}, \mathbf{y})$ introduced in Section (5.1) are decomposed into contributions of the individual partons, i.e. both leptons and the four jets. The choice of functions in Equation (5.1) is motivated in the following.

Since the segmentation of the calorimeter is very good, the angles of the observed jets are assumed to agree with the angles of the produced partons. Figure (6.1) shows the ΔR distribution for leptons and jets and verifies this assumption. As is the case for leptons, the resolution of jet angles is described by delta-functions.

Due to the detector resolution it is assumed that the momentum of the charged lepton is measured with infinite precision. This is validated by Figure (6.2) which shows the distributions of ΔE between the produced and the measured lepton in simulated $t\bar{t}$ events. Therefore, delta-functions are used to describe the corresponding resolution. In case of electrons this assumption is valid (comparing the electron resolution with the jet resolution). For muons, however, the energy resolution is worse but is also treated as perfectly measured. In principle, an integration over the lepton resolution has to be performed which was not done in the present analysis due to the CPU time limitations. A proposal on that issue is given in Chapter 9. In this analysis the resolution effect is dealt with as a systematic uncertainty and is discussed in Chapter 8.

Because the neutrino only interacts weakly it is not observed. A constant term is therefore assigned for the resolution.

As mentioned previously the energy resolution of jets is not compatible with the corresponding resolution of electrons. Therefore, the mapping between jet and parton energies has to be described by transfer functions with finite width. The following section explains the parametrization and derivation of parameters.

6.2. Energy Mapping

In order to find an adequate parameterization for the jet energy resolution, Figure (6.3) shows the energy difference for light and heavy flavor partons. Those are treated separately due to the different hadronization processes of light and heavy partons. As can be seen from these plots the

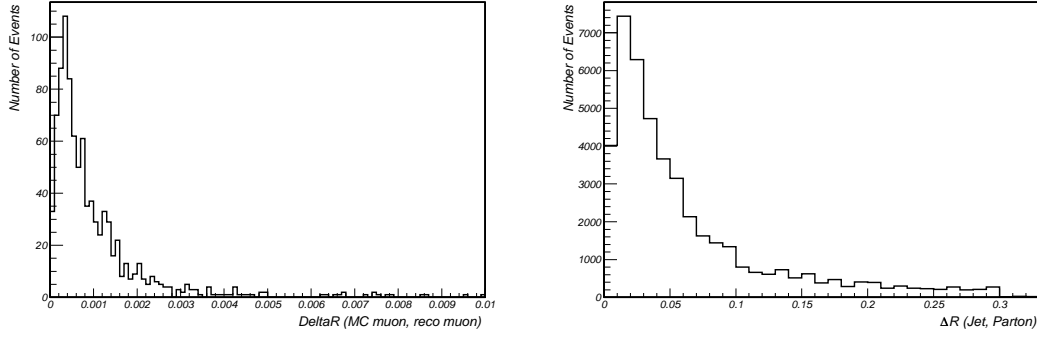


Figure 6.1.: Distribution of ΔR for muons (left) and jets (right). The angular resolution is assumed to be measured well and is described by δ -functions.

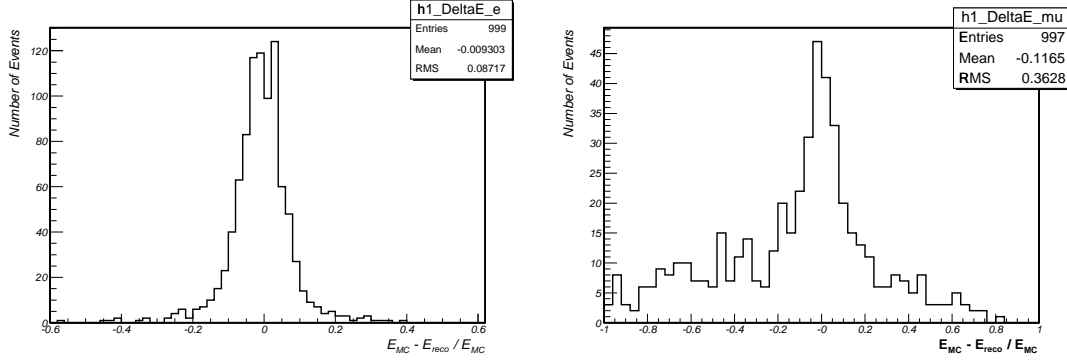


Figure 6.2.: Distribution of relative energy difference between reconstructed and true lepton energy. **Left:** electrons, **right:** muons. The resolution is assumed to be perfect and described by δ -functions.

distributions are not centered around 0 GeV and have non-gaussian tails. Since the concept of transfer functions takes the shape of the energy resolution into account an average correction (for example assuming a gaussian resolution) is not precise enough. A double-gaussian is therefore used to account for the tails. As found in various studies [26, 32] the parameters p_1 to p_5 depend linearly on the parton energy. The transfer functions can be written as

$$W_{jet}(E_{jet}, E_{parton}) = \frac{1}{\sqrt{2\pi}(p_2 + p_3 \cdot p_5)} \left(e^{\frac{-(\delta - p_1)^2}{2 \cdot p_2^2}} + p_3 \cdot e^{\frac{-(\delta - p_4)^2}{2 \cdot p_5^2}} \right), \quad (6.1)$$

where

$$\delta = E_{jet} - E_{parton}, \quad (6.2)$$

$$p_i = a_i + E_{parton} \cdot b_i. \quad (6.3)$$

Since the energy deposition depends on the parton flavor three different classes are introduced: light quarks (u, d, s, c), b quarks and b quarks tagged with a soft muon. The latter is expected to behave differently from the b quark due to the neutrino in the final state. For each of these classes the parameters are derived separately.

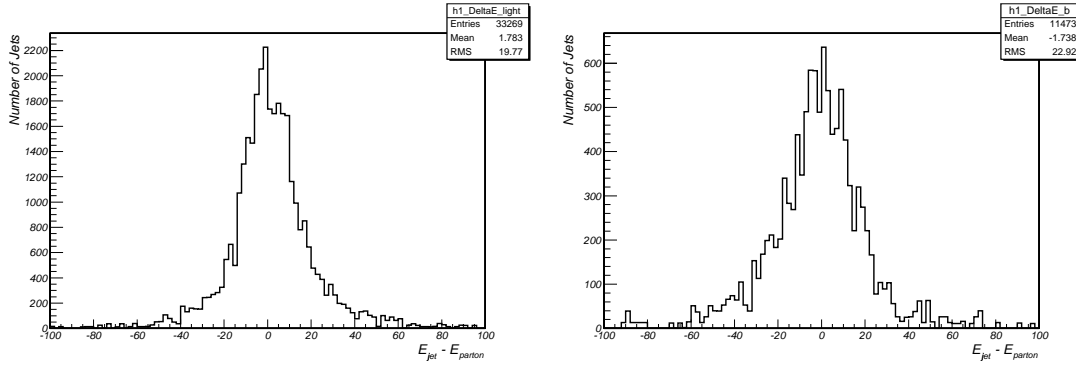


Figure 6.3.: Distribution of the ΔE between jets and partons for light quarks (**left**) and heavy quarks (**right**). The distributions are obtained from $t\bar{t}$ Monte Carlo using a jet-parton-matching of $\Delta R < 0.5$.

It is also found that the various calorimeter regions show a different behavior in terms of energy resolution. Therefore, the classes are subdivided into regions of η_{det} . These correspond to the values shown in Table (6.1)

Region	η_{det}
Central Calorimeter (CC)	$0.0 < \eta_{det} < 0.7$
Intercryostat Region (ICR)	$0.7 < \eta_{det} < 1.8$
Endcap (EC)	$1.8 < \eta_{det} < 2.5$

Table 6.1.: Calorimeter regions.

The parameters for the transfer functions are determined from $t\bar{t}$ Monte Carlo. Samples with top quark polemasses from 150 GeV/c² to 200 GeV/c² are used. The measured energy differences are fitted to the parameterization (6.1) using Minuit [33]. The parameter a_3 is fixed to 0 in order to suppress an interchange of both gaussians¹. The fit was furthermore constraint to the central region, i.e. $|\Delta E| < 100$ GeV. Because it is a priori not obvious which jet belongs to which parton, a jet-parton-matching criterion of $\Delta R < 0.5$ is required. No further event selection is applied to the sample. The parameters obtained from the Monte Carlo sample are summarized in Tables (6.2) to (6.4).

p_i	light quarks		b quarks		μ tagged b quarks	
	a_i	b_i	a_i	b_i	a_i	b_i
p_1	1.5142523	-0.0046015	-1.0909721	0.0435889	-4.3974654	0.0757411
p_2	3.4869614	0.1038399	4.1037500	0.1089371	13.9044167	0.0775983
p_3	0.0000000	0.0005679	0.0000000	0.0011010	0.0000000	0.0030358
p_4	40.9175703	-0.3190310	17.1947255	-0.2336131	11.0602161	-0.1045415
p_5	27.6811911	-0.0081009	18.4153637	0.1075442	17.1776951	0.2719917

Table 6.2.: Transfer function parameters for light, b and muon tagged b jets in the CC region.

As an example for the functional form, Figure (6.4) shows transfer functions for parton energies between 10 GeV and 250 GeV for light and b quarks separately. The parameters p_1 to

¹The parameterization is chosen such that the first gaussian accounts for the peak and second one for the tails. It is obvious that the second contribution is treated as a small distortion to the dominating gaussian form.

p_i	light quarks		b quarks		μ tagged b quarks	
	a_i	b_i	a_i	b_i	a_i	b_i
p_1	2.6141864	-0.0341720	0.2792247	-0.0012560	1.7073751	0.0751120
p_2	2.8410319	0.1527113	2.8484498	0.1766203	5.7015008	0.1269471
p_3	0.0000000	0.0006705	0.0000000	0.0005233	0.0000000	0.0020146
p_4	39.5960027	-0.1583219	27.056039	-0.1949308	20.2409154	-0.0571302
p_5	27.2056889	0.0005969	26.910188	0.0736229	29.1609261	0.2804977

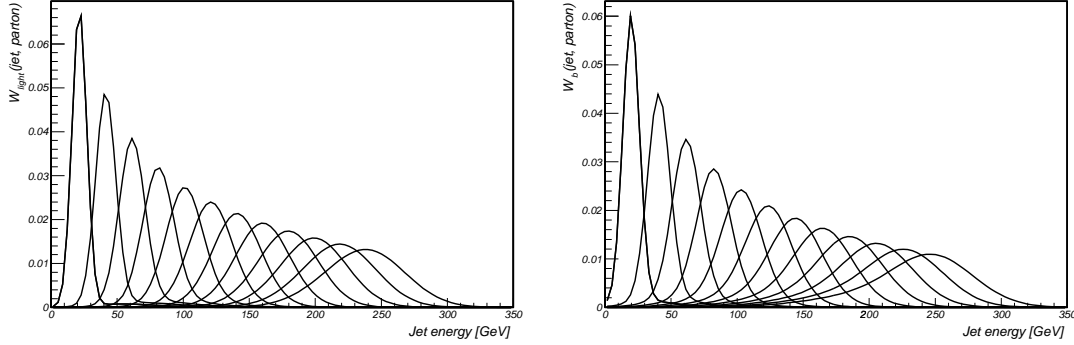
Table 6.3.: Transfer function parameters for light, b and muon tagged b jets in the ICR region.

p_i	light quarks		b quarks		μ tagged b quarks	
	a_i	b_i	a_i	b_i	a_i	b_i
p_1	43.2233050	-0.3329035	13.0231503	0.0958643	23.7877953	-0.1860100
p_2	16.2033350	0.1097911	17.1328564	0.0385995	6.0943296	0.1466943
p_3	0.0000000	0.0714187	0.0000000	0.0337702	0.0000000	0.0007603
p_4	9.1657811	-0.0454625	-0.2936919	-0.0081156	186.3178830	-0.8531883
p_5	8.5964739	0.1067287	1.8167135	0.1818514	68.7850770	-0.5303422

Table 6.4.: Transfer function parameters for light, b and muon tagged b jets in the EC region.

p_5 are calculated from the corresponding tables.

Figure (6.5) shows the distribution of energy difference between jets and partons in different intervals of the parton energy (in this case the light jets in the central region are shown). The black histograms correspond to the measured values from Monte Carlo, the red/grey histograms display the energy difference taken from parton level events smeared with the corresponding transfer function. As can be seen from these plots the agreement is reasonable, especially in the regions with larger statistics.

**Figure 6.4.:** Example for the parameterization of the transfer functions. Parton energies between 10 GeV and 250 GeV in steps of 12.5 GeV (from left to right) are used to calculate the parameters p_1 to p_5 . **Left:** Light quarks in the CC region. **Right:** b quarks in the CC region.

As a further cross-check the invariant mass distributions for the hadronic top and W are shown in Figure (6.6). Again, the black histogram corresponds to the measured jets, the red/grey histogram to the smeared partons. Both histograms are compatible within the given statistics.

More details on the derivation and the transfer functions in general can be found in [26]. The parameters are derived from the Monte Carlo samples listed in Appendix D by Alan Magerkurth.

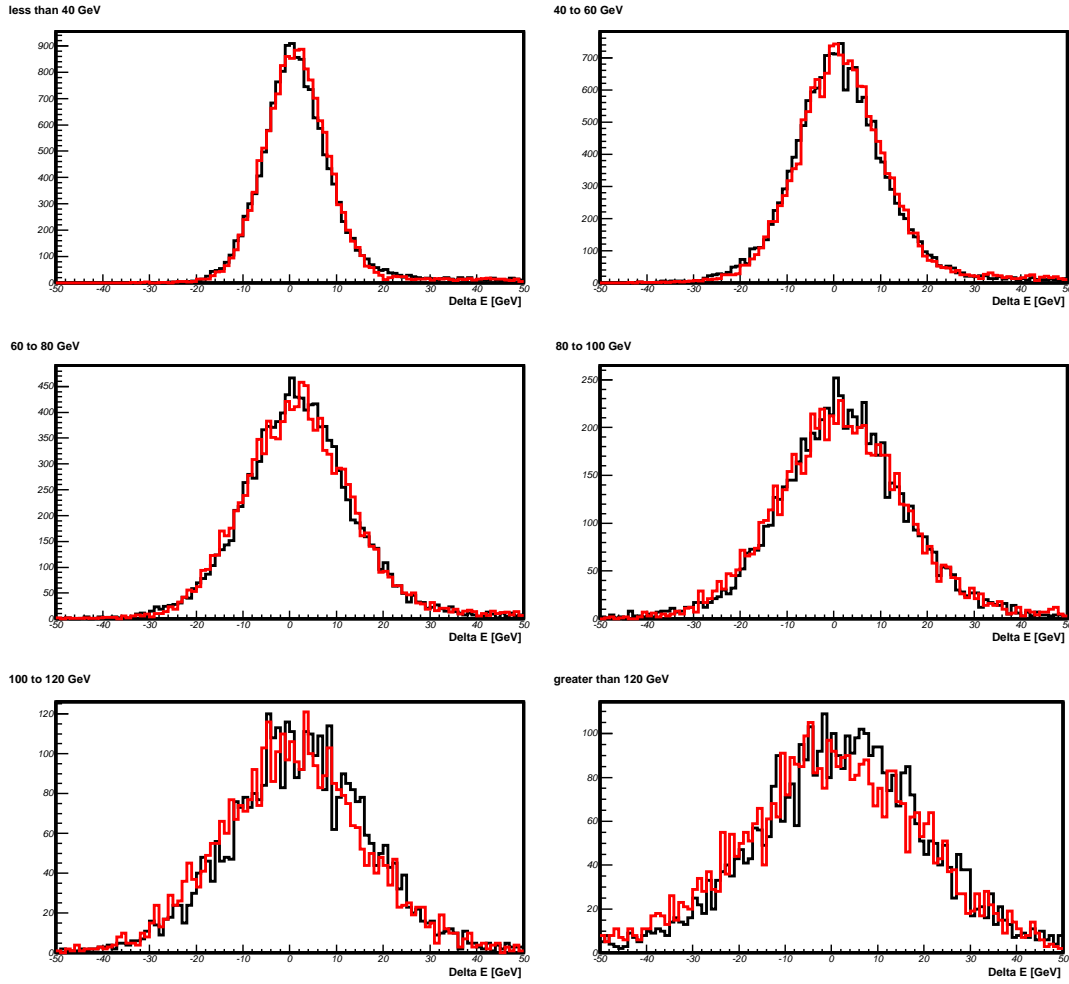


Figure 6.5.: Distribution of energy differences of light jets for reconstructed (black) events and events smeared according to the transfer functions (red/grey). Each plot corresponds to an interval of parton energy. The description of the energy distribution by the transfer functions are sufficiently good given the limited statistics.

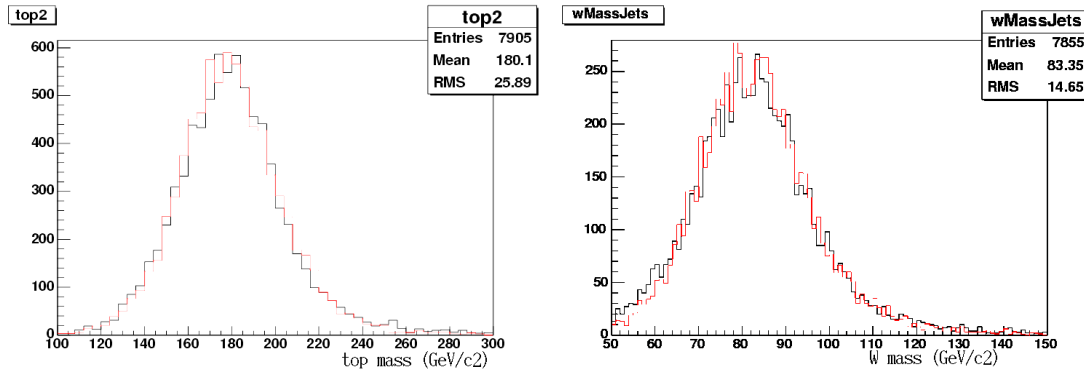


Figure 6.6.: Invariant masses of the hadronic top (left) and W (right). The black histograms correspond to the reconstructed mass, the red/grey histograms to smeared partons. Both histograms agree within the given statistics.

6.2.1. Comparison to Run I

Since in the Run I analysis the transfer functions were parameterized in the same way as is done here, a comparison of the jet energy resolution is possible. Figure (6.7) shows examples for light and b quarks at a parton energy of 100 GeV. As can be seen, the Run II transfer functions are broader than the ones used previously due to the resolution of the calorimeter being degraded by the new tracker and the solenoid. As is observed in the analysis, the statistical error is therefore larger than in the Run I. Also, a clear shift in both examples can be seen. The parameters for the Run I transfer functions are taken from [32], where no further corrections have been applied.

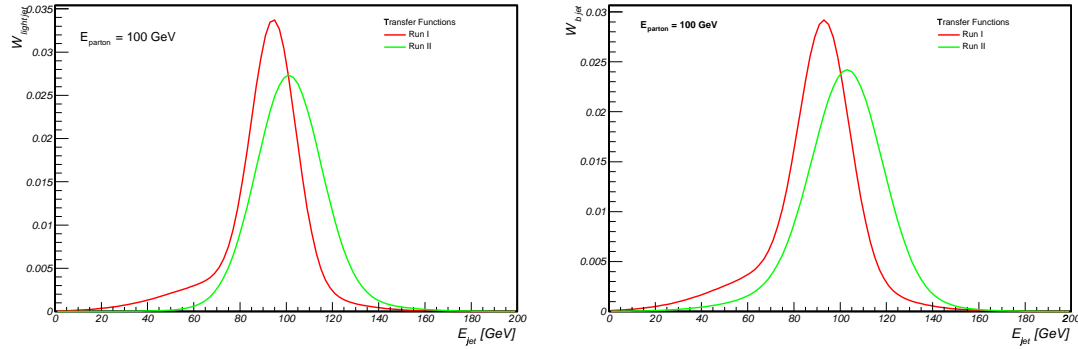


Figure 6.7.: Comparison of transfer functions from the Run I and the present analysis for light (**left**) and b quarks (**right**) in the central calorimeter. The latter ones are broader due to the resolution of the calorimeter and shifted towards higher energies. Both functions are calculated at a parton energy of 100 GeV.

6.3. Corrections and Normalization

Before the transfer functions are obtained from the Monte Carlo several corrections are applied to the jet energies. These have to be taken into account when integrating over the transfer functions. Two factors are described in the following: parton-level corrections and η -dependent corrections.

6.3.1. Parton-Level Corrections

The jet energies obtained from the Monte Carlo (as well as from data) are corrected for the jet energy scale (JES) by the ROOT tuple maker `top_analyze` [34]. In order to account for effects such as hadronization, out of cone corrections etc. additional parton-level corrections are applied to the jet energies, which are described in [35]. These corrections are simple scale factors multiplied to the jet energy. The parameterization for the parton-level corrections is chosen in the following way:

$$f_{pc} = \frac{-q_1 + \sqrt{q_1^2 - 4 \cdot q_2 \cdot (q_0 - E_{jet})}}{2q_2 \cdot E_{jet}}, \quad (6.4)$$

where q_0 , q_1 and q_2 are parameters to be estimated from Monte Carlo and stated in Table (6.3.1). Since they are different for light and heavy flavor (no distinction is made between muon tagged or untagged jets), two separat sets of parameters are obtained. As in case of the transfer functions the correction factors vary with the η_{det} region and therefore a discrimination is also done here.

q_i	light quarks			b quarks		
	CC	ICR	EC	CC	ICR	EC
q_1	-2.001	-0.76	5.5686	-4.246	-3.27	-4.318
q_2	1.0485	0.9862	0.8992	1.0181	0.9658	0.9674
q_3	$1.342 \cdot 10^{-4}$	$4.496 \cdot 10^{-4}$	$7.905 \cdot 10^{-4}$	$3.412 \cdot 10^{-5}$	$2.836 \cdot 10^{-4}$	$3.44 \cdot 10^{-4}$

Table 6.5.: Parameters for the parton-level corrections for light and heavy flavors in three different regions of η_{det} .

6.3.2. η -dependent Corrections

Since the jet energy scale is found to be dependent on the η region, further corrections are applied to account for this effect. Details on the derivation can be found in [35]. Again, scale factors are obtained from Monte Carlo and data separately using the following parameterization:

$$f_\eta = \frac{1}{1 + \Delta S(\eta)}, \quad (6.5)$$

Figure (6.8) shows ΔS as a function of η_{det} for both, data and Monte Carlo.

6.3.3. Normalization

Since Equation (4.7) forces the transfer functions to be normalized to one, a proper normalization has to be applied. Naturally, the double-gaussian parameterization fulfils this requirement, but

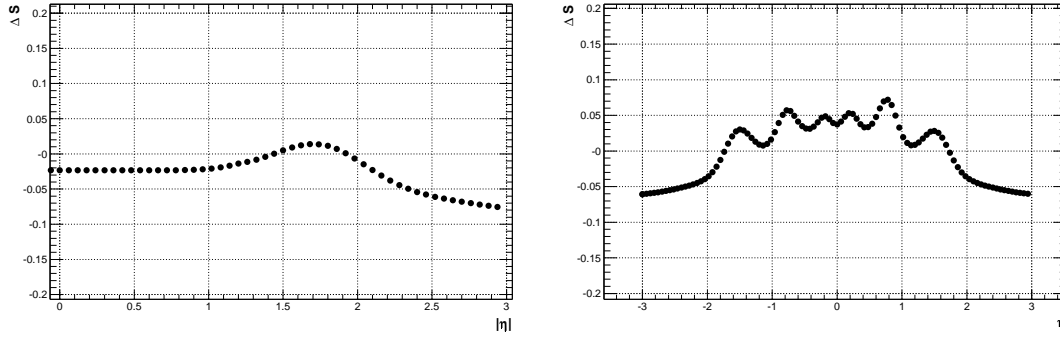


Figure 6.8.: η -dependent corrections: ΔS as a function of η_{det} for Monte Carlo (left) and data (right). In case of Monte Carlo the curve is symmetric around $\eta = 0$, in the case of data the function was measured and parameterized with a superposition of Gaussians. These functions translate into a scale factor for the jet energies.

only with respect to energies in the range of $-\infty$ GeV to $+\infty$ GeV which is unphysical because parton energies are positive. Therefore, the transfer functions are integrated over the jet energies in the interval (0 GeV, 300 GeV) and parameterized as a function of the parton energy:

$$N = \int_{0 \text{ GeV}}^{300 \text{ GeV}} W(E_{parton}, E_{jet}) dE_{jet} \quad (6.6)$$

These integrals are the normalization factors by which the transfer functions are divided in order to account for the physical region. Figure (6.9) shows the example for light quarks.

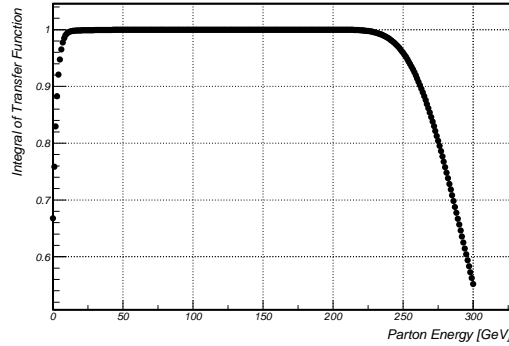


Figure 6.9.: Additional normalization factor due to a cut on the physical region.

Due to the finite range of integration in case of the light jet (0, 300 GeV), the integral of the transfer function is also lower for larger values of the parton energy. This is accounted for during the integration.

7. Monte Carlo Studies and Application to Data

The following chapter describes the application of the method to Monte Carlo events and data. First, parton level information is used in order to test the method and study features of the matrix elements involved. As a next step, these events are used to study the finite energy resolution of the detector. Therefore, the energies of the quarks are smeared according to the expected resolution, i.e. the transfer functions derived in the previous chapter. Also, the purity of the sample is varied by adding $W + 4 \text{ jets}$ events and the effect on the mass measurement is studied. Before applying the method to data, ensemble tests with reconstructed Monte Carlo events are done. Here, all effects expected in data (contamination by $W + 4 \text{ jets}$ and QCD events, initial (ISR) and final (FSR) state radiation, lepton resolution effects, etc.) are included. The application to data follows subsequently.

Since this thesis is part of the $D\bar{O}$ mass analysis effort [26] the ensemble tests and the application to data are done in collaboration with Philipp Schieferdecker, LMU Munich.

7.1. First Studies of Parton Level Monte Carlo

As a first step, the method is applied to simulated $t\bar{t}$ events using the parton level information. This corresponds to a perfect measurement of the kinematic properties of an event and no mixup of partons and jets. Even though this is a rather unrealistic case it is done in order to study the method and understand features of the ingredients such as the matrix elements. For that reason only $t\bar{t}$ events are used in this section, where no further event selection was applied to the sample. The influence of background contributions is studied separately and is discussed in the next section.

The $t\bar{t}$ events used in this step are generated with the MADGRAPH generator, where no parton level cuts are applied. Samples of 1000 events are produced for top quark polemasses ranging from 140 GeV/c² to 200 GeV/c².

Figure (7.1) shows the distribution of both, top quark and W boson masses (hadronic and leptonic separatly). Since no detector resolution is involved, the widths of all four distributions are essentially close to their nominal value, i.e.

$$\begin{aligned}\Gamma_{top} &\sim 1.4 \text{ GeV}/c^2 \\ \Gamma_w &\sim 2.0 \text{ GeV}/c^2\end{aligned}\tag{7.1}$$

Assuming a perfect detector with full geometric coverage the acceptance is a constant ($Acc(\mathbf{x}) = 1$).

The transfer functions, discussed in the previous chapters, are set to δ -functions in order to account for a perfect angular and energy resolution. Thus, the integrals in Equation (5.8)

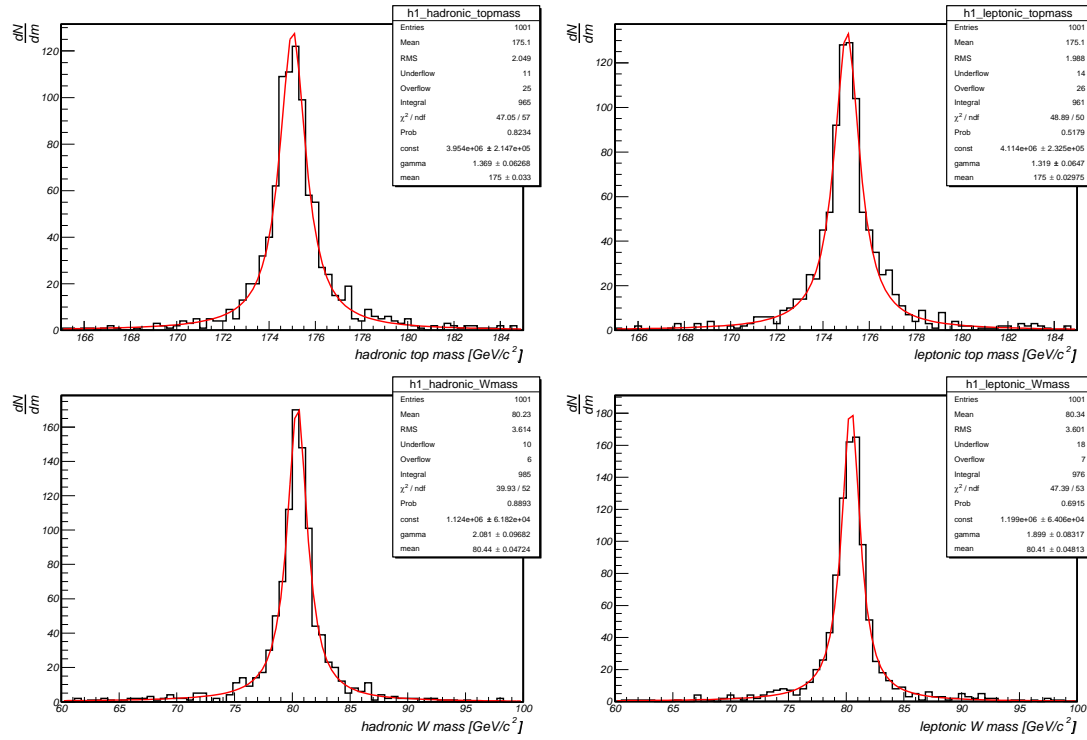


Figure 7.1.: Top: hadronic (left) and leptonic (right) invariant mass spectrum of the top quark calculated from the decay products. **Bottom:** hadronic (left) and leptonic (right) invariant mass spectrum of the W boson calculated from the decay products. The polemass of the top quark in this particular sample is $175 \text{ GeV}/c^2$. The fits to the histograms are Breit-Wigner functions.

simplify in such a way that the integrand has to be evaluated at the measured (in that case the produced) values. In this scenario, only the correct jet parton combination is taken into account. Also, since all kinematic objects (leptons and jets) are known precisely only one neutrino solution contributes. The kinematic solver is not used in this case.

The probability for each event is calculated taking into account the constraints mentioned. Figure (7.2) shows the likelihood for single, typical events as a function of the top mass hypothesis. The events are taken from a sample with $175 \text{ GeV}/c^2$ top quark polemass. As expected the likelihoods in (a) - (c) peak nicely in a region close to $175 \text{ GeV}/c^2$. (d) shows a likelihood with two peaks. This is due to the fact that in this particular event the values for the hadronic and leptonic top quark mass differ. Even though the top width is of the order of $1.4 \text{ GeV}/c^2$ (see Figure (7.1)) events with different top masses occur frequently. As can be seen from these plots, the probability is fully dominated by the Breit-Wigner terms in the matrix element. The observed likelihood curves fully agree with the expectation.

As a closure test, the likelihood of the whole sample is calculated for each sample, i.e. for different top quark polemasses. Figure (7.3) (left) shows the likelihood for the $175 \text{ GeV}/c^2$ sample. In Figure (7.3) (right) the measured top quark mass is plotted as a function of the true mass. A straight line fit is performed obtaining parameters which are consistent with a slope of 1 and an offset of $0 \text{ GeV}/c^2$. In order to minimize the correlation between slope and offset, the values are shifted into the center of gravity of the points during the fit. This procedure is followed throughout the whole analysis.

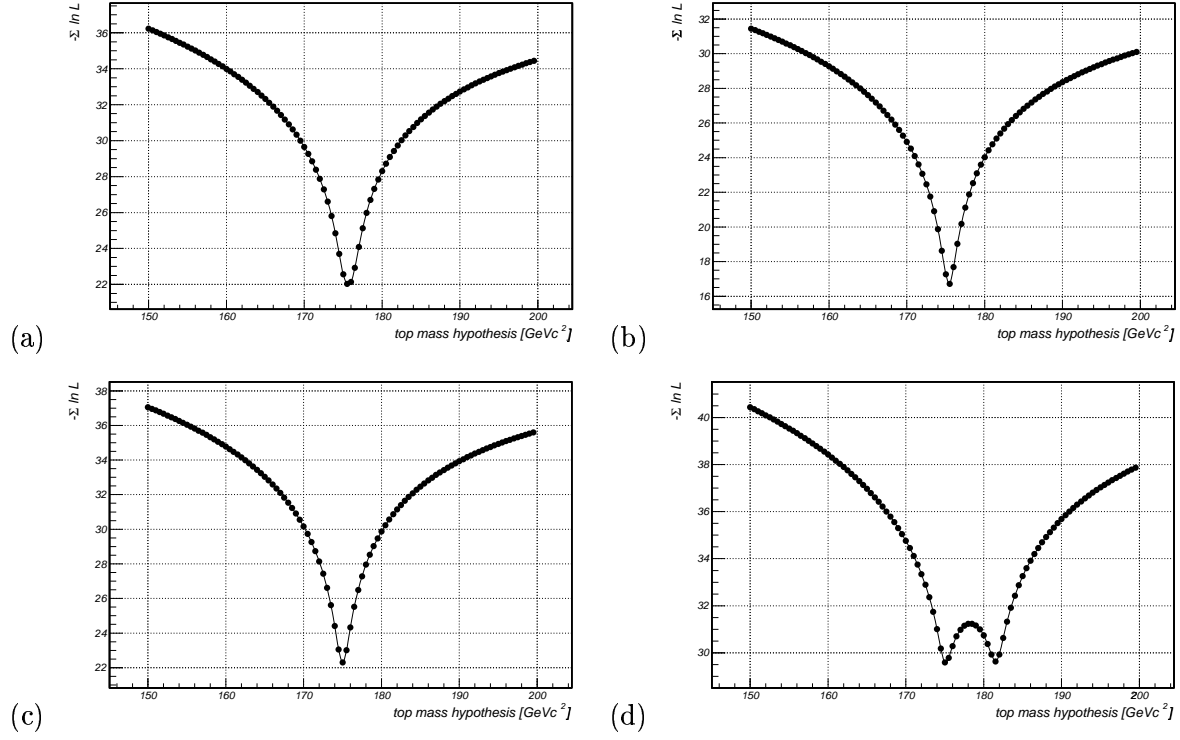


Figure 7.2.: Likelihood for single $t\bar{t}$ events as a function of a top quark mass hypothesis. The events are taken from a sample with a top quark polemass of $175 \text{ GeV}/c^2$. The likelihood curves in (a) - (c) peak nicely in a region close to $175 \text{ GeV}/c^2$. In (d) two peaks are observed. These occur because the hadronic and leptonic top mass differ (here: $m_{top}^{had} = 175.04 \text{ GeV}/c^2$, $m_{top}^{lep} = 181.64 \text{ GeV}/c^2$).

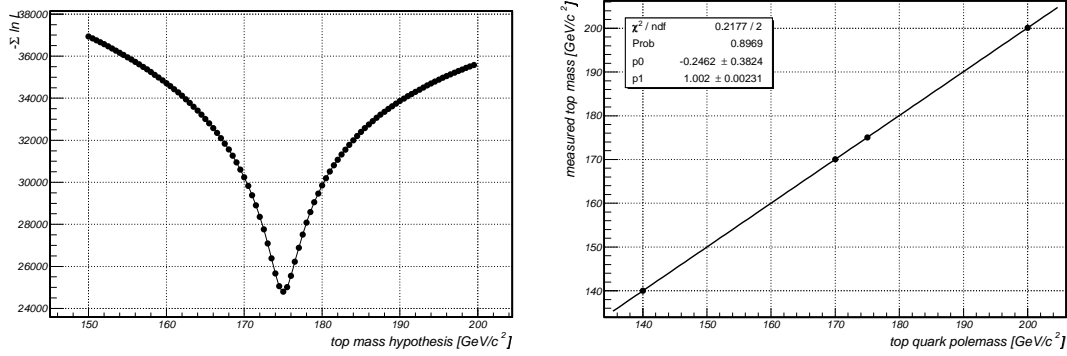


Figure 7.3.: **Left:** Likelihood of all events in the sample with a top quark polemass of $175 \text{ GeV}/c^2$. **Right:** Measured top quark mass vs. polemass. The fitted straight line is consistent with a line of slope 1 and offset $0 \text{ GeV}/c^2$.

Concluding the studies done based on parton level information, an unbiased estimator of the top quark mass is found. Figure (7.3) shows the consistency and stability of the estimator. As mentioned previously, no detector resolution effects or background contributions are taken into account so far. The former is introduced in the next section.

7.2. Studies of Smeared Parton Level Monte Carlo

As a next step, the influence of a finite jet energy resolution is studied. Therefore, Monte Carlo events are generated (again using the MADGRAPH generator for $t\bar{t}$ events) and the jet energies are smeared according to the energy resolution. Also, $W + 4 \text{ jets}$ events are generated using the ALPGEN generator and also here the energies are smeared. Two different sets of smearing functions are used to account for the detector resolution. First, a gaussian function with a width proportional to the square root of the parton energy is used (this is motivated by the energy resolution expected from calorimeters), and second the set of transfer functions used in the analysis of reconstructed Monte Carlo and data events (i.e. a double gaussian). Of course both, the smearing of the parton level energies and the resolution (transfer functions) used in the calculation of the probability have to be the same. In the following the case of double gaussian transfer functions is discussed only.

7.2.1. Comparison on Event by Event Basis

Figure (7.4) shows the masses of the two top quarks and W bosons reconstructed from the decay products. As expected the finite energy resolution leads to a broadening of these distributions compared to those displayed in figure (7.1).

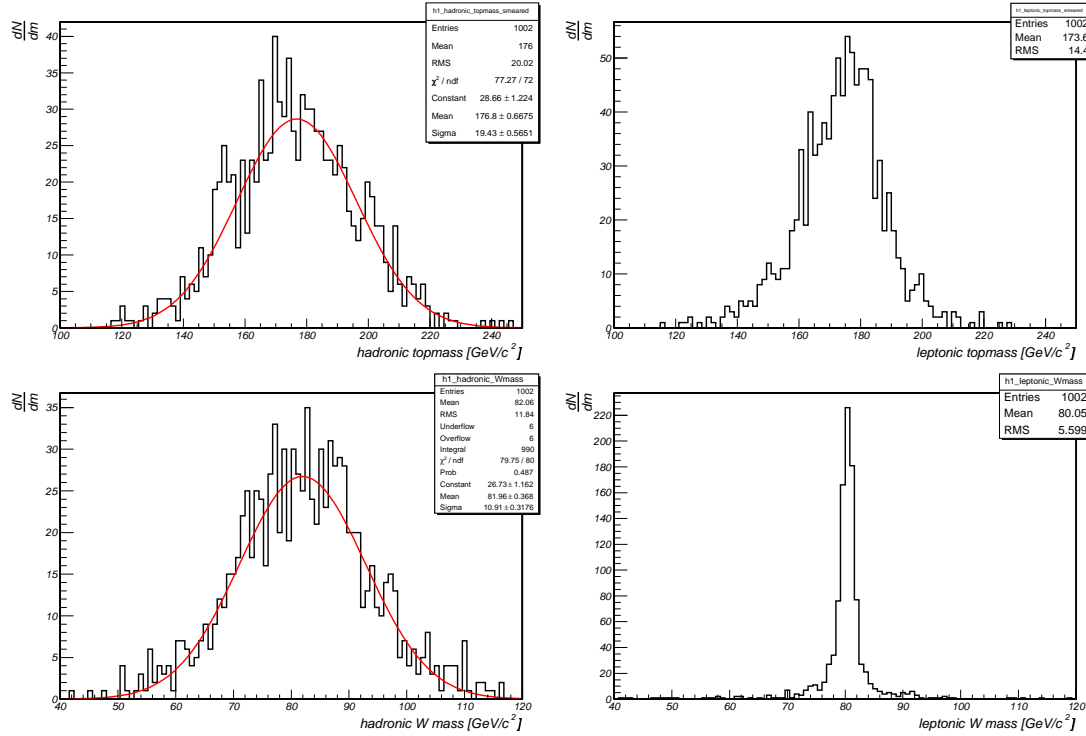


Figure 7.4.: **Top:** hadronic (**left**) and leptonic (**right**) invariant mass spectrum of the top quark calculated from the decay products. **Bottom:** hadronic (**left**) and leptonic (**right**) invariant mass spectrum of the W boson calculated from the decay products. In this case the energies of the jets are smeared according to the energy resolution leading to broader distributions.

Since the energy resolution is assumed to be finite, the integrals in Equation (5.8) have to be performed numerically. The techniques used in case of the signal and background probability

are described in the previous chapters. All combinations of jet parton assignments as well as all solutions obtained from the kinematic solver are taken into account. It should be mentioned that all jets considered in the variety of combinations come from the $t\bar{t}$ or $W + 4 \text{ jets}$ event, i.e. there are no contributions from initial state (ISR) or final state radiation (FSR) at this stage of the analysis. Those influences are dealt with in the next section. At the reconstruction level, it is not possible to assign jets to partons.

In this part, the influence of the geometrical acceptance is not taken into account. Therefore, no cuts on the events are introduced and the average acceptance is again set to 1.

Figure (7.5) shows the calculated likelihood of one particular $t\bar{t}$ event taking into account only the signal probability. On the left hand side the jet energies are not smeared (so the calculation is identical to that described in the previous section, only that all jet parton combinations are taken into account), on the right hand side the jet energies are smeared according to the assumed resolution. From the comparison of both figures it is obvious that a finite energy resolution will increase the statistical uncertainty, i.e. the curve on the right hand side is much broader than the one on the left hand side. The shift of the minimum value of the likelihood can be explained by the fact that the invariant mass of the sum of decay particles does not have to be close to the polemass of the sample, as can be seen in Figure (7.4).

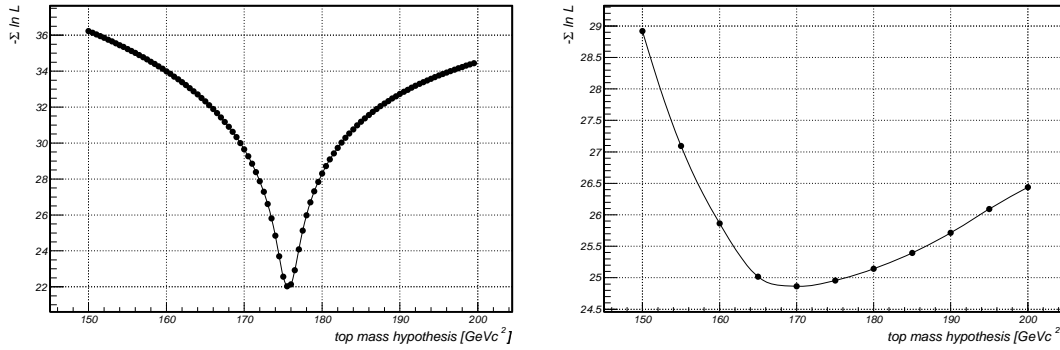


Figure 7.5.: Comparison of a single event with (left) perfect and (right) finite energy resolution. Again, the $t\bar{t}$ sample with a top quark polemass of 175 GeV/c² is used. In this particular case, the purity of the sample was set to 1.

Figure (7.6) shows four more examples of the likelihood (again using only the signal probability). (a) - (c) are $t\bar{t}$ events, (d) is a $W + 4 \text{ jets}$ event. In the former case the curves peak around the polemass whereas in the latter case the negative log-likelihood increases steadily, i.e. the likelihood increases to low masses.

So far, only the signal probability is taken into account. In order to estimate the mass of the top quark correctly, also the purity of the sample has to be estimated. This is done by minimizing the negative likelihood with respect to the purity (c_1) for each mass hypothesis and then minimize the negative likelihood according to the mass hypothesis at these points. Figure (7.7a) explains this procedure graphically. An example for the minimization with respect to c_1 (with $m_{top} = 170.0$ GeV/c² fixed) is displayed on the right hand side of Figure (7.7).

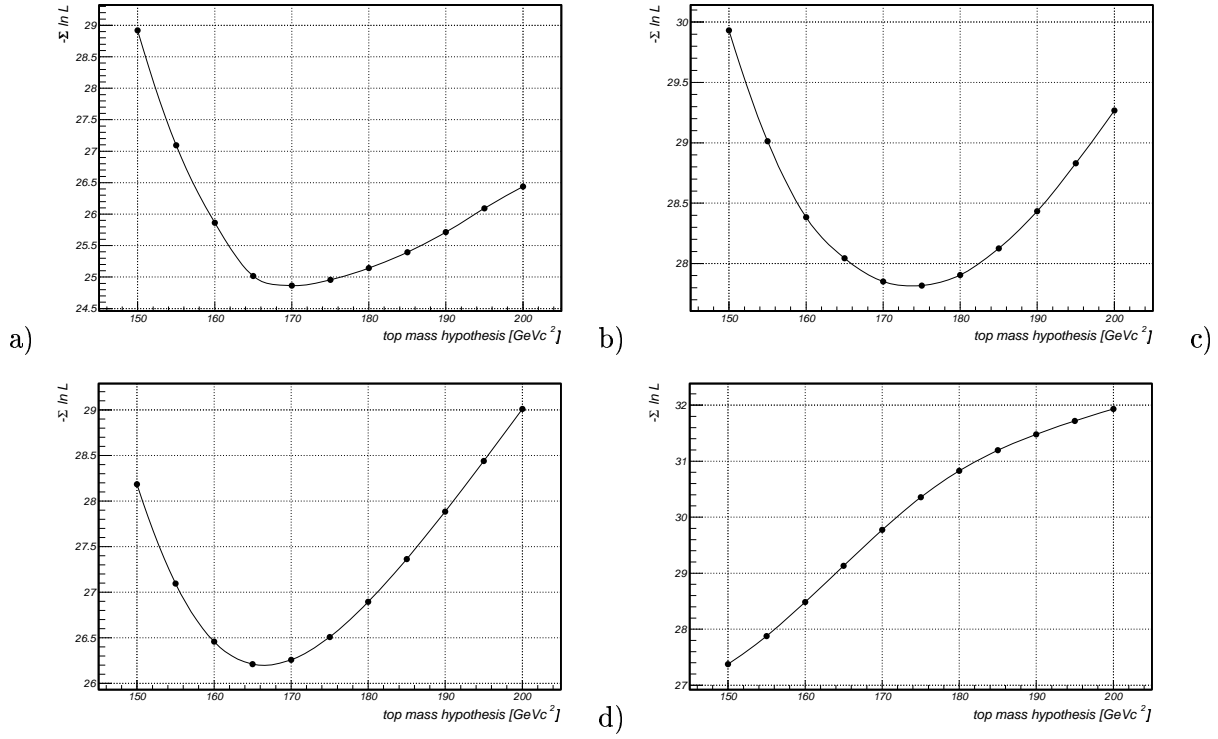


Figure 7.6.: Examples of likelihood curves for four single events. (a) - (c) show $t\bar{t}$ events, (d) shows a $W + 4 \text{ jets}$ event.

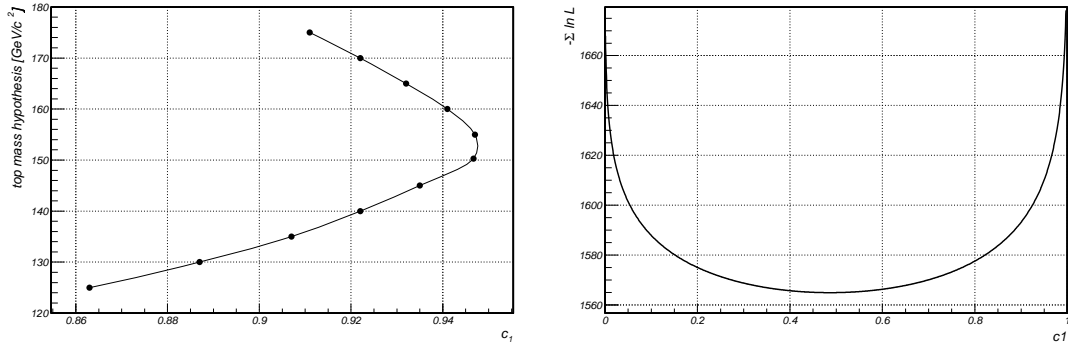


Figure 7.7.: **Left:** Minimizing the negative likelihood: for each mass hypothesis the negative likelihood is minimized with respect to c_1 and afterwards with respect to the top mass at the calculated values for c_1 . The plot shows the minima in the c_1 -likelihood. **Right:** Minimization of the likelihood with respect to c_1 . In this example the top mass hypothesis equals the polemass ($170 \text{ GeV}/c^2$) and the input purity of the sample is 0.5.

7.2.2. Ensemble Tests

In order to reduce the statistical uncertainty and to account for the expected number of $t\bar{t}$ events in the measured sample, ensemble tests are done. From a pool events are drawn randomly and ensembles of 60 events are built for which the negative likelihood is minimized. Since the final calibration to data is done with reconstructed Monte Carlo events, the procedure of ensemble tests is described in more detail in the next section.

Using a sample with a top quark polemass of $170 \text{ GeV}/c^2$ these tests are done for varying purities. For a pure signal sample, i.e. $c_1 = 1$, the distribution of measured masses is plotted on the top left of Figure (7.8). As can be seen from there, a slight shift ($\approx +2.6 \text{ GeV}/c^2$) towards higher masses is found. In order to estimate the effect, the distribution of the statistical uncertainties and the pull distribution are shown in the bottom plots of Figure (7.8). In case of a gaussian distributed error, the width of the pull is supposed to be unity, which is almost the case here ($\sigma \sim 1.1$). A discussion of the shift and the pull width follows in section 7.2.4.

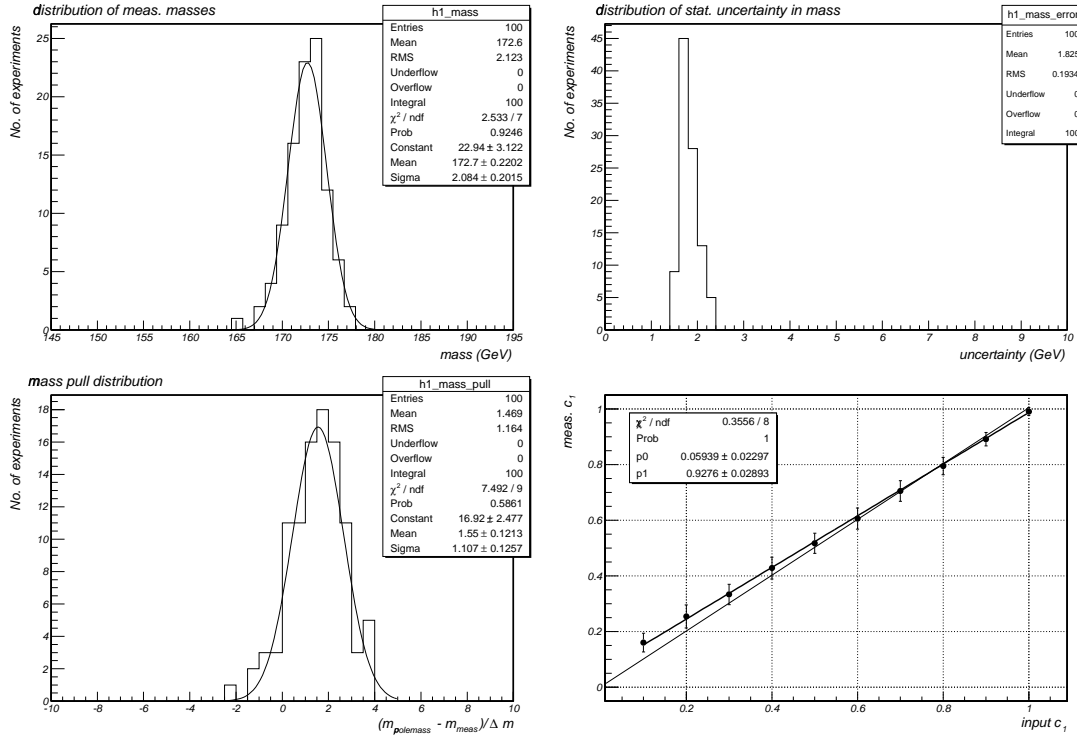


Figure 7.8.: **Top left:** Distribution of measured masses in ensemble tests. Each ensemble consists of 60 $t\bar{t}$ events without background contribution. The polemass of the sample is $170 \text{ GeV}/c^2$, so a slight shift towards higher masses is observed. **Top right:** Distribution of the statistical uncertainty of each ensemble. **Bottom left:** The pull distribution for the ensembles described in the text. Although the width of the pull is consistent with 1, the mean value is slightly shifted towards higher masses as can also be observed in the top left plot. **Bottom right:** Calibration curve for the purity. Fitting a straight line to the points, a slope less than one is found.

The influence of background contamination is shown in Figures (7.8) and (7.9). Figure (7.8) shows the estimated purity as a function of the actual input purity. The straight line fit gives a slope of 0.93 ± 0.03 and an offset of 0.06 ± 0.02 . Figure (7.9) shows the measured mass as a function of the input c_1 . It can be concluded that (given the limited statistics) no systematic

shift occurs due to adding background events (in this case only $W + 4 \text{ jets}$), although the overall shift is still visible. In order to obtain a measure of the expected statistical uncertainty, Figure (7.9) shows the uncertainty multiplied by the width of the pull. This is done in order not to underestimate the statistical error.

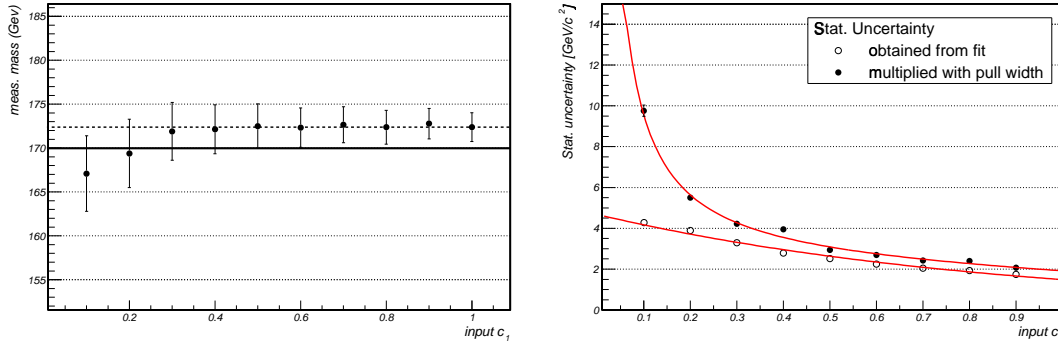


Figure 7.9.: Left: Measured mass as a function of purity. Within the statistical uncertainty no systematic effect due to background contributions is observed. Towards very low purity, however, a small trend toward lower masses might show up. **Right:** Statistical uncertainty as a function of the purity of the ensembles. In order to not underestimate the error, the values are multiplied with the width of the pull (between 1.0 and 1.5).

7.2.3. Discrimination between Signal and Background

Since event probabilities for $t\bar{t}$ and $W + 4 \text{ jets}$ production are calculated, a certain discrimination power between signal and background samples is expected. Figure (7.10) shows a scatter plot of signal vs. background probability for a pure $t\bar{t}$ and $W + 4 \text{ jets}$ sample. Also displayed is the line of equal probabilities. The signal probability is evaluated at the polemass of the sample in order not to bias the distribution. As can be seen from there, both samples can be separated quite well. As taken advantage of in the Run I analysis, the background probability has a certain discriminative power. However, since effects like mismatching due to ISR/FSR and QCD events are missing at this stage of the analysis, the study can only determine qualitative behaviour. Additional studies on the discrimination are done for the case of reconstructed Monte Carlo.

7.2.4. Calibration of the Mass Estimator

Concluding from the measurement of smeared parton level events, a systematic shift in the top mass is observed. This bias does not depend on the fraction of background events in each ensemble so it can be calibrated. The reason for the observed shift are under investigation. Because the parton-level tests are all successful, the technical implementation of the integration might bias the result. Also, the narrow width approximations for the top and W masses can be an error source. These effects have to be revisited and studied in detail and are, for the time being, considered as systematic uncertainties from the signal modeling. A calibration curve for the mass estimator (as well as for the expected uncertainty, etc.) is derived from reconstructed Monte Carlo since in that case all additional effects expected in data (detector acceptance and efficiency, ISR/FSR, QCD contributions, etc.) are included. The evaluation of the signal and background probabilities are very CPU-time intense so any further studies are discussed in the next section.

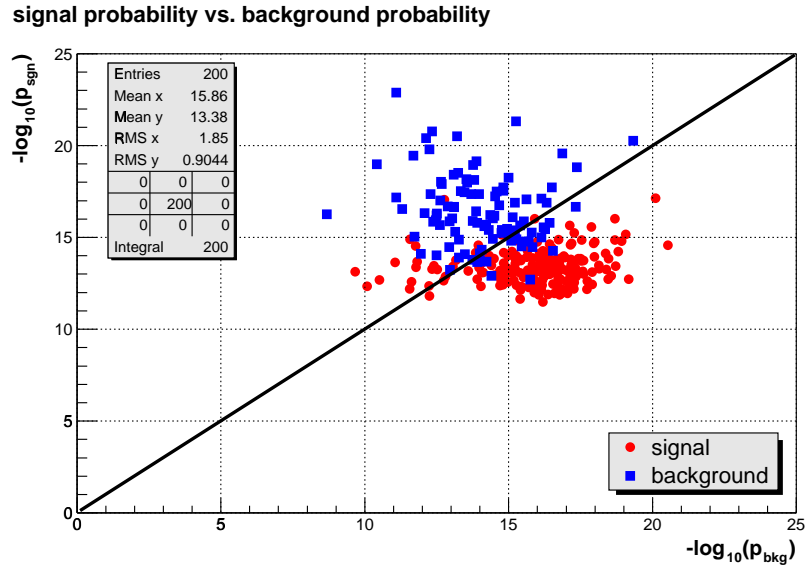


Figure 7.10.: Signal vs. background probability for pure $t\bar{t}$ and $W + 4 \text{ jets}$ samples. A certain discrimination between the two physics processes involved is possible.

7.3. Studies of Reconstructed Monte Carlo Events

Before applying the method to data, ensemble tests have been performed using reconstructed Monte Carlo events. These are generated using the ALPGEN event generator (interfaced to PYTHIA [36] in order to simulate the showering process) and subsequently reconstructed in the GEANT detector simulation¹. A list of samples used in the following can be found in Table (7.1) and in Appendix D. $t\bar{t}$ samples with different polemasses are available in the reconstruction version p14. In case of the background, $W + 4 \text{ jets}$ events are generated and reconstructed in the same way as the signal events. For the QCD contributions, data events are selected using the selection criteria described in [1] since no Monte Carlo generator for “misreconstruction” is available for the processes involved. The relative mixture of the $t\bar{t}$, $W + 4 \text{ jets}$ and QCD events for the ensemble testing are determined from data, as described in the following section.

Sample	Number of events	comments
150 GeV/c ² $t\bar{t}$	600	no MPI
160 GeV/c ² $t\bar{t}$	300	no MPI
170 GeV/c ² $t\bar{t}$	300	no MPI
175 GeV/c ² $t\bar{t}$	1000	no MPI
175 GeV/c ² $t\bar{t}$	300	MPI
180 GeV/c ² $t\bar{t}$	300	no MPI
190 GeV/c ² $t\bar{t}$	300	no MPI
200 GeV/c ² $t\bar{t}$	600	no MPI
$W + 4 \text{ jets}$ (I)	1000	hard parton level cuts, no MPI
$W + 4 \text{ jets}$ (I)	1000	hard parton level cuts, MPI
$W + 4 \text{ jets}$ (II)	1000	soft parton level cuts, MPI

Table 7.1.: Monte Carlo samples used in this analysis. The roman numbers refer to Samples I and II in Table (7.2)

Due to a bug in the ALPGEN interface to PYTHIA both, the $t\bar{t}$ and $W + 4 \text{ jets}$ sample do not account for multi parton interactions (MPI), i.e. no soft underlying events are added to the events. For that reason the $t\bar{t}$ sample with a polemass of 175 GeV/c² and the $W + 4 \text{ jets}$ sample were regenerated. The effect of multi parton interactions on the mass measurement is discussed in Chapter 8 on systematic uncertainties.

As discussed in the next chapter, the $W + 4 \text{ jets}$ sample was also regenerated with different settings. This is done because the data to Monte Carlo comparison shows much better agreement with the alternative setting (sample II in Table 7.1) of parton level cuts (for settings see Table (7.2)).

Figure (7.11) shows the masses of the hadronic top quark and the W boson reconstructed from their daughter particles. As expected, the finite energy resolution leads to a broadening of these distributions compared to those displayed in Figure (7.1).

¹Since in principle it would be much more consistent to use the same matrix element for the event generation and subsequent analysis, no fully reconstructed MADGRAPH events are available at the moment.

Cut	Sample I	Sample II
jet p_T	> 12 GeV	> 8 GeV
jet $ \eta $	< 3.5	< 3.0
dR(jet, jet)	> 0.4	> 0.4
neutrino p_T	> 8 GeV	-
lepton $ \eta $	< 2.7	-
MPI	no	yes
PDF set	CTEQ6.1M	CTEQ5L
Factorisation scale	$Q^2 = M_W^2/4$	$Q^2 = M_W^2 + \sum p_T^2$

Table 7.2.: Settings of the $W + 4$ jets samples. Sample I has harder parton-level cuts than Sample II.

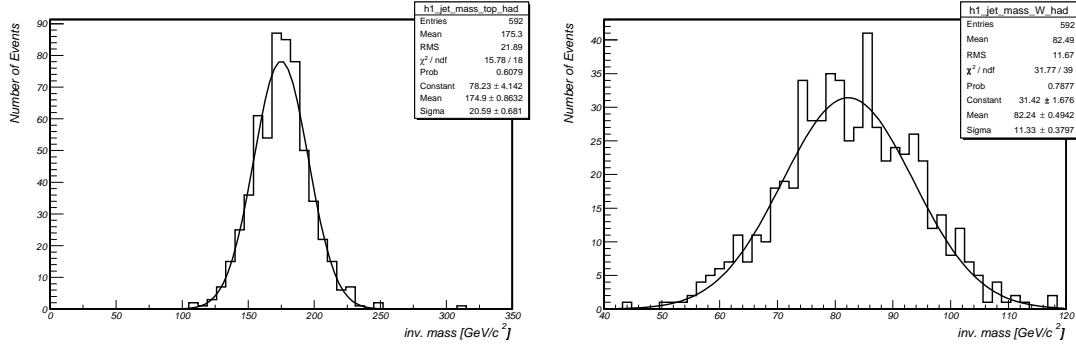


Figure 7.11.: Left: Hadronic top mass for a generated value of $m_{top} = 175$ GeV/c². Right: Hadronic W mass. Both masses are reconstructed using the correct (parton matched) jets. Due to the finite energy resolution the distributions are much broader than those shown in Figure (7.1).

Event Selection and Acceptance

The selection criteria used for the mass analysis follow those of the $t\bar{t}$ cross section measurement [1]. Table (7.3) summarizes the cuts applied to the samples. In contrast to the cross section measurement no soft lepton veto is required since this analysis is not intended to be orthogonal to the soft-lepton tag analysis. Also, only events with exactly 4 jets are selected. This requirement accounts for the fact that the matrix element describes 4 jets at leading order, i.e. no additional jets (ISR/FSR) enter the calculation of the probability. This way it is possible to match each jet to a parton in the matrix element. Further studies on how to include events with more than 4 jets will be done in the future.

As mentioned earlier, the average acceptance depends on the top mass given the kinematic constraints of the event selection. It is calculated using Equation (5.11), but instead of using the number of observed events, each event is given a certain weight according to the trigger efficiency. For that reason N_{obs} is replaced by the sum of the weights of all events passing the criteria displayed in Table (7.3). A more detailed description of the event selection can be found in the cross section analysis [1]. The acceptance for $t\bar{t}$ events is calculated for each sample and plotted as a function of the top mass (Figure (7.12)). Note that in case of the electron channel only the central calorimeter (CC) is used for the lepton reconstruction. In case of the background, the average acceptance is calculated for $W + 4$ jets events:

Criterion	$e + jets$	$\mu + jets$
Vertex		
$ z_{PV} $	< 60 cm	< 60 cm
N_{tracks} attached to vertex	≥ 3	≥ 3
Muon		
Muon quality	-	medium, nseg=3
track match	-	required
Cosmic veto	-	required
p_T	-	> 20 GeV
Isolation	-	tight isolation
DCA significance	-	< 3 , $\Delta z(\mu, PV) < 1$ cm
Electron		
emf	> 0.9	-
iso	< 0.15	-
hmx8	< 75	-
associated track	required	-
p_T	> 20 GeV	-
Likelihood	> 0.75 (CC)	-
Neutrino		
Missing E_T	> 20 GeV	> 17 GeV
$\Delta\Phi(l, met)$ cut	applied	applied
$\Delta\Phi(leadingjet, met)_{cut}$	-	applied
Jets		
p_T	> 15 GeV	> 15 GeV
$ \eta $	< 2.5	< 2.5
Additional Vetoes		
Second Electron Veto	required	-

Table 7.3.: Event preselection criteria used in this analysis. In addition to the cross section analyses, the number of jets is restricted to exactly 4. Also, no soft lepton veto is applied here.

$$\begin{aligned}
\langle Acc \rangle_{W(\rightarrow e\nu)+4jets} &= (3.1 \pm 0.1)\%, \\
\langle Acc \rangle_{W(\rightarrow \mu\nu)+4jets} &= (3.0 \pm 0.1)\%.
\end{aligned}$$

In order to further increase the purity of the sample the background probability is used as a discriminative quantity. Figure (7.13) shows the background probability distributions for $t\bar{t}$, $W + 4 jets$ and QCD events in both channels. The distributions are all normalized to 1 to study their discriminative power. From the plots it follows that $W + 4 jets$ and QCD events look similar in terms of background probability as is expected since the jets in both event classes are produced by the same QCD mechanism. Furthermore, the $t\bar{t}$ and background distributions overlap.

Note, that the background probabilities in Figure (7.13) are not corrected for the acceptance because the latter depends on the cut value. This can be seen on the right hand side of Figure (7.12), where the efficiency of the background probability cut on the $t\bar{t}$ sample with respect to the preselected sample is plotted as a function of the top polemass. For softer cuts the efficiency approaches values close to 1, while for harder cuts a mass dependence becomes

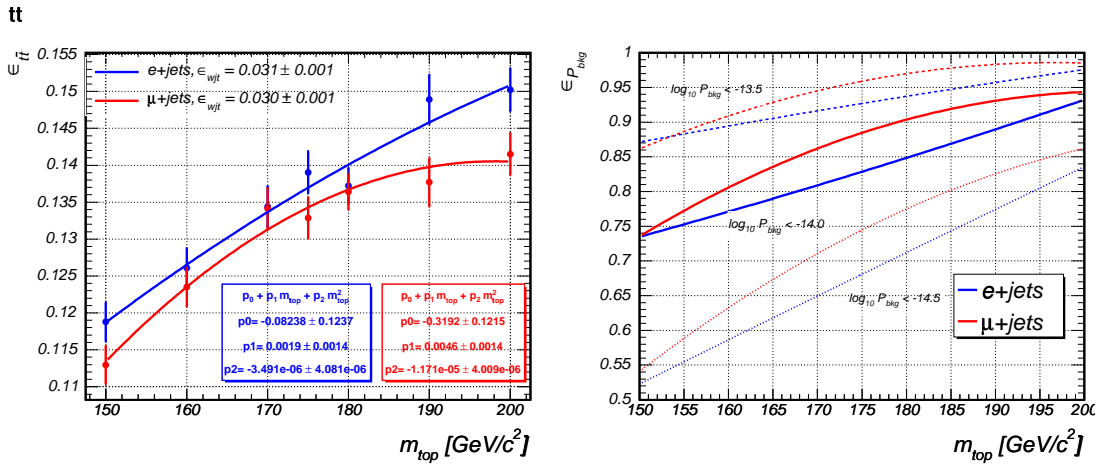


Figure 7.12.: Left: Average acceptance for muon and electron channel as a function of the top quark mass for the event selection before background probability cut (=preselection). The points are obtained from Monte Carlo and fitted with 2nd order polynomials. The selection criteria are described in Table (7.2) **Right:** Efficiency of the background probability cut with respect to the preselection.

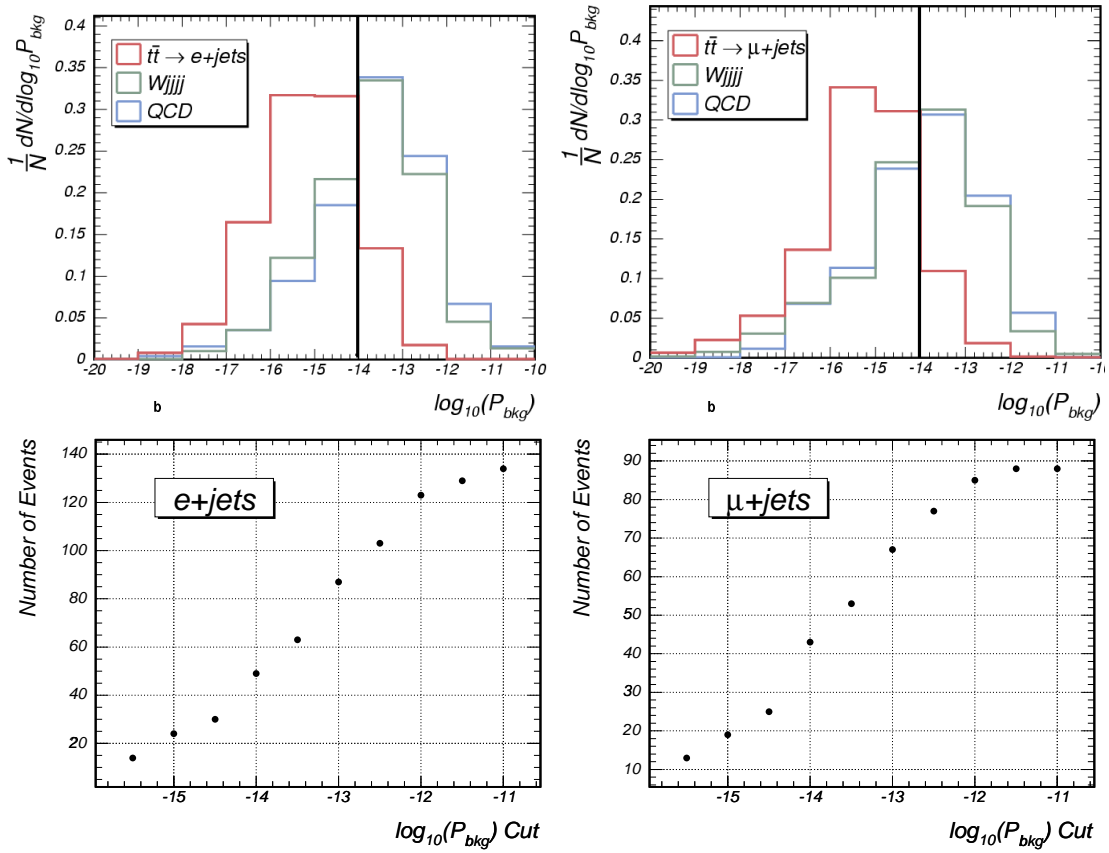


Figure 7.13.: Top: Distributions of background probabilities for $t\bar{t}$, $W + 4 jets$ and QCD events. The cut on the background probability is placed at $10^{-14.0}$. **Bottom:** Number of events vs. the background probability cut. **Left:** $e + jets$ channel. **Right:** $\mu + jets$ channel.

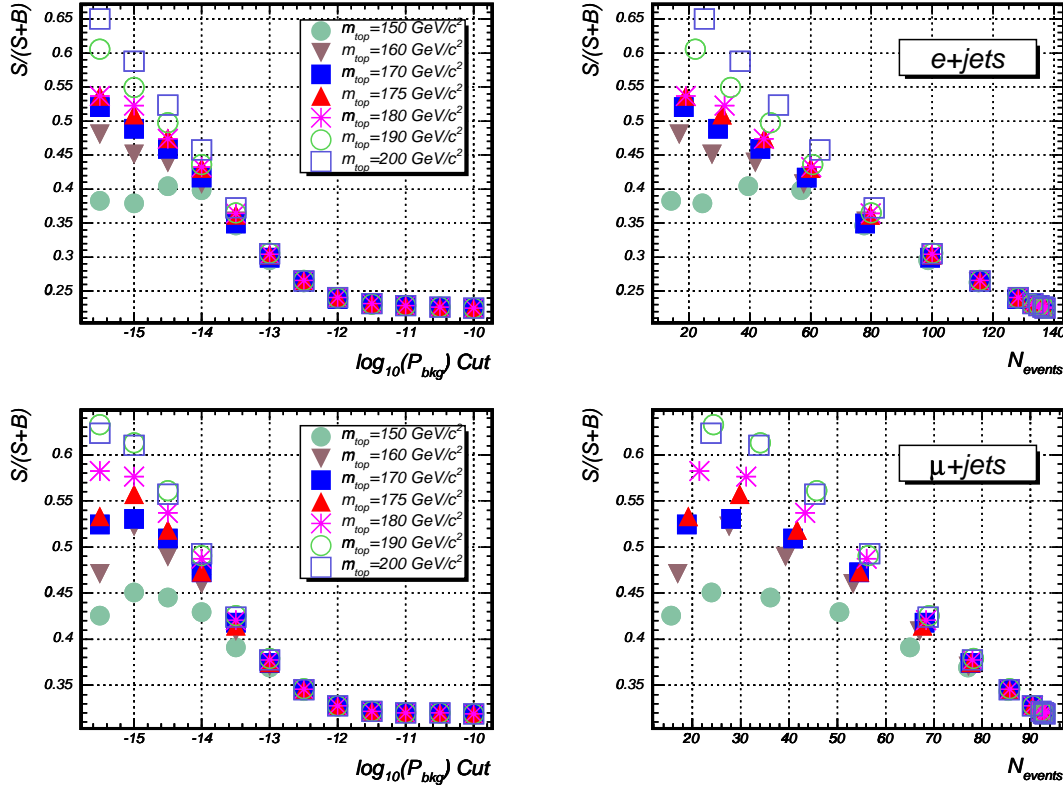


Figure 7.14.: Purity vs. background probability cut value for $e + \text{jets}$ (top) and $\mu + \text{jets}$ (bottom) together with the number of events.

visible.

The cut value is chosen such that on the one hand the discrimination between signal and background is reasonable and on the other hand that not too many top events are cut out. From the distributions in Figures (7.13) and (7.14) it is concluded that a cut on the background probability of

$$p_{bkg} < 10^{-14.0}$$

is appropriate. Variations of $10^{-14 \pm 0.5}$ in the cut value are studied in analogy to the Run I analysis and confirm its stability (see ensemble tests and Chapter 8 on the systematic uncertainties). Also, events are not included that have a signal probability of 0 for at least one mass hypothesis. This is done to ensure the continuity of the likelihood curve.

Due to the fact that partons from initial or final state radiation might be misidentified as partons from the $t\bar{t}$ process, an additional source of uncertainty enters the mass estimation. Since the Matrix Element Method does not account for this possibility, the influence of ISR/FSR has to be studied and calibrated. This procedure is introduced further in this section. Figure (7.15) shows the distribution of matched jets in the 4th jet multiplicity bin using varying ΔR radii as matching criterion. For $\Delta R < 0.3$ the matching efficiency for 4 jets is roughly 60%.

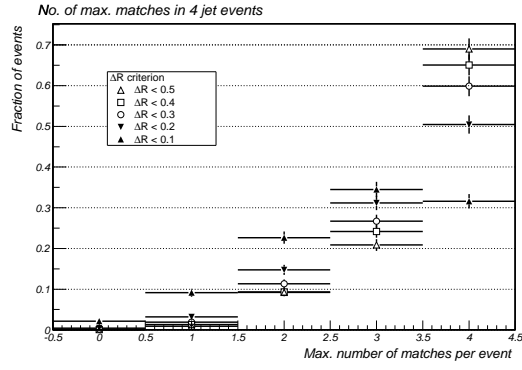


Figure 7.15.: Efficiency for jet-parton matching in the 4th jet-multiplicity bin using different ΔR -criteria.

Ensemble Tests

Following the descriptions given in the previous sections, the signal and background probability for each event are calculated and corrected for the acceptance. Since an estimate on the number of $t\bar{t}$ events in the data sample is given from the cross section measurement, ensemble tests are done for this estimated value of $t\bar{t}$, QCD and $W + 4 \text{ jets}$ fraction in the event sample. In order to obtain the relative fractions of events, the 1st and 2nd matrix methods are used which are also described in [1]. First, the QCD events in the data sample are separated from the rest. In the second step, the remaining events are divided into $t\bar{t}$ and $W + 4 \text{ jets}$ contributions, where the 2nd matrix method is used to separate the samples. Additionally, only those events are selected that have exactly 4 jets. The numbers obtained for the $e + \text{jets}$ and $\mu + \text{jets}$ channels after the preselection are summarized in Table (7.4).

Contribution	$e + \text{jets}$	$\mu + \text{jets}$
$t\bar{t}$	$30.8^{+14.3}_{-13.1}$	$29.7^{+11.9}_{-10.7}$
$W + 4 \text{ jets}$	$81.2^{+17.4}_{-16.8}$	$56.5^{+13.3}_{-12.6}$
QCD	$25.0^{+2.2}_{-2.1}$	$6.7^{+0.8}_{-0.8}$
observed	137	93

Table 7.4.: Contributions of $t\bar{t}$, $W + 4 \text{ jets}$ and QCD in the data sample before the background probability cut. The numbers are calculated using the first and second matrix method.

The numbers obtained for the $e + \text{jets}$ and $\mu + \text{jets}$ channels after the background probability cut (final event selection) are summarized in Table (7.5)

Contribution	$e + \text{jets}$	$\mu + \text{jets}$
$t\bar{t}$ -fraction	$0.438^{+0.203}_{-0.186}$	$0.471^{+0.187}_{-0.170}$
QCD-fraction	0.110	0.053
observed number of events	49	44

Table 7.5.: Contributions of $t\bar{t}$, $W + 4 \text{ jets}$ and QCD in the data sample after the background probability cut. The numbers are calculated using the first and second matrix method.

Ensembles with contributions according to the numbers in Table (7.5) are built for samples with masses 150 GeV/c², 160 GeV/c², 170 GeV/c², 175 GeV/c², 180 GeV/c², 190 GeV/c², and 200 GeV/c². Although the Standard Models predicts a cross section which depends on the top quark mass, the number of top events in the ensemble is not varied for the different polemasses. This is done in order to be independent of the cross section constraint, rather the estimate from data is used. 500 ensembles are built from the pool available with a number of events such that the sum of (trigger-)weights equals the sum in Table (7.5) stated above. The following describes the ensemble tests at a top quark polemass of 175 GeV/c² in the $e + \text{jets}$ and $\mu + \text{jets}$ channels. Afterwards, the calibration curves for the mass measurement are derived.

$e + jets$ channel

Figure (7.16) shows the distribution of measured masses for the $175 \text{ GeV}/c^2$ sample in the $e + jets$ channel. A gaussian is fitted to the distribution giving a mean of $178.6 \pm 0.3 \text{ GeV}/c^2$ and a sigma of $6.94 \pm 0.25 \text{ GeV}/c^2$. The observed shift is expected from the analysis with smeared parton level events as discussed in the previous section. A calibration curve is derived in the following and applied to the following distributions. Figure (7.16) also shows the distribution of the statistical uncertainties of the ensembles, as well as the pull distribution. For an unbiased estimate with gaussian errors one expects a mean of zero and a width of unity for the pull distribution. A gaussian fit applied here yields a mean of -0.28 ± 0.06 and a sigma of 1.26 ± 0.05 . The slight difference from 0 in the mean is due to an overcorrection at a top mass of $m_{top} = 175 \text{ GeV}/c^2$ as will be seen in the following. The expected statistical uncertainty is defined as the width of the gaussian fit to the mass distribution, which in this case is $6.9 \text{ GeV}/c^2$.

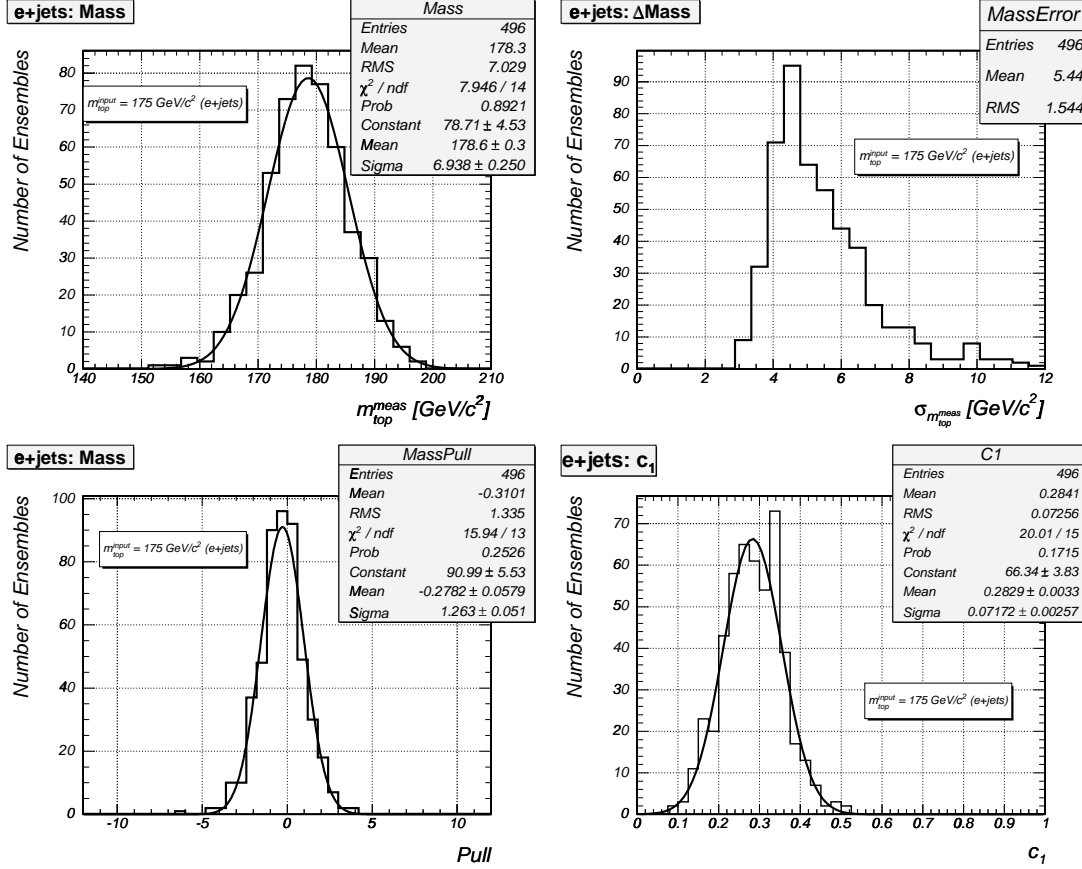


Figure 7.16.: **Top left:** Distribution of the uncorrected measured masses for 500 ensembles in the $e + jets$ channel. The gaussian fit gives a mean of $178.6 \pm 0.3 \text{ GeV}/c^2$ and a sigma of $6.94 \pm 0.25 \text{ GeV}/c^2$. **Top right:** Distribution of the statistical error as obtained from the likelihood. The mean is $5.44 \text{ GeV}/c^2$. **Bottom left:** Pull distribution. The gaussian fit gives a mean of -0.28 ± 0.06 and a sigma of 1.26 ± 0.05 . **Bottom right:** Distribution of the estimated purity. The latter three plots are made after the mass calibration correction.

Since the width of the pull is significantly different from unity, further cross checks have been done. Figure (7.17) shows the pull for a second ensemble test similar to the previous one, but without QCD contribution. As can be seen from there, the width of the pull does not decrease and it is therefore concluded that, although the QCD contribution in the $e + jets$ channel is larger than in the $\mu + jets$ channel, the effect comes from a different source. Section (7.4) shows a comparison of data to Monte Carlo for several important quantities which led to speculations on the quality of the electron identification.

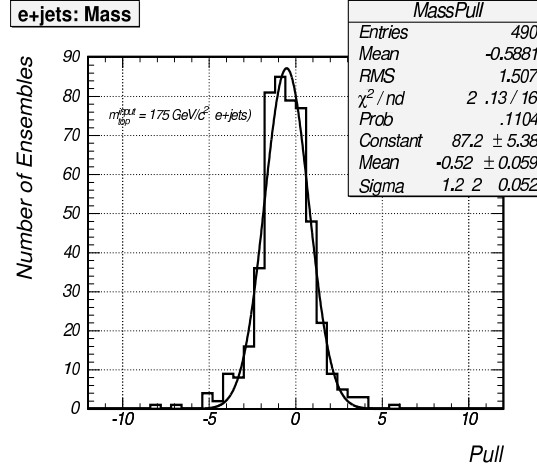


Figure 7.17.: Pull for a second ensemble test similar to the previous one, but without QCD contribution. The width of the pull does not decrease.

The ensemble tests are repeated for the different mass samples. Figure (7.18) shows the measured mass as a function of the input polemass fitted with a straight line. The parameters are a slope of 1.02 ± 0.03 and an offset of $4.90 \pm 0.53 \text{ GeV}/c^2$. This linear correction is applied to the bare measured mass in the $e + jets$ channel. The shift in the mass distribution was also observed in the previous chapter. In the case of reconstructed Monte Carlo multiple solutions from the kinematic solver and contributions from wrong jet/parton combinations can have an additional impact on the mass. Also, wrong assignments of jets due to initial and final state radiation have an impact on the measured mass. Additionally, it is worth mentioning that the Monte Carlo generator used to produce the partons is not the same as the one used in the analysis. The former does, for example, not account for the finite width of the top quark and the W boson. These issues will be studied in more detail in the future. Figure (7.18) also shows the statistical uncertainty on the mass measurement, taken from the width of the measured top mass distribution (so this is implicitly corrected for the width of the pull), and the width of the pull assuming ensembles similar in size and contributions to those described earlier. In the bottom right of Figure (7.18) the calibration curve for c_1 is plotted as a function of the input purity and also fitted with a straight line.

In order to check the stability of the background probability cut, Figure (7.19) shows the measured mass and the statistical uncertainty as a function of the cut value for the $175 \text{ GeV}/c^2$ sample. The stability is reasonable within an interval of $\pm 1 \text{ GeV}/c^2$ and is dealt with as a source of systematic uncertainty. Cutting at background probabilities of $10^{-14.5}$ or lower one starts

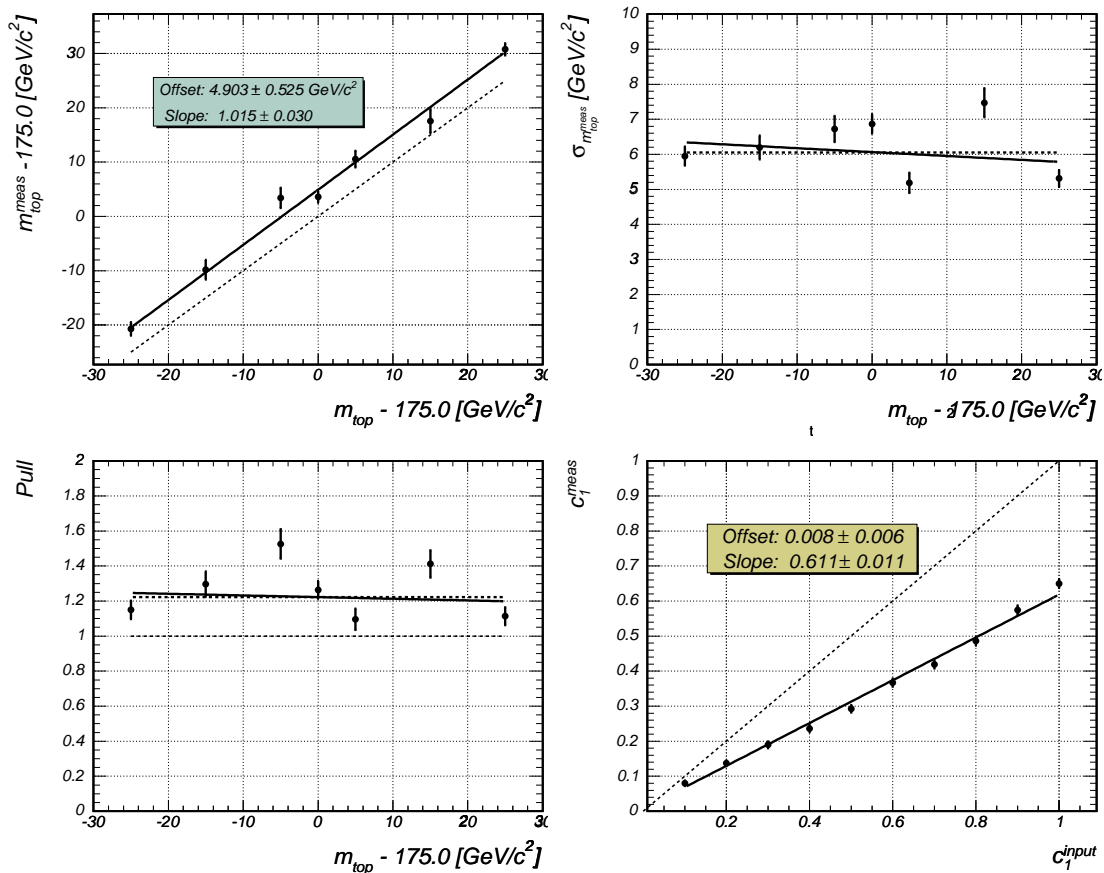


Figure 7.18.: $e + jets$ channel. **Top left:** Mass calibration, a constant offset of 4.90 GeV/c² is observed. **Top right:** Statistical uncertainty as a function of the top mass. **Bottom left:** Width of the pull distribution as a function of the top mass. **Bottom right:** Measured c_1 as a function of the input purity.

cutting into the signal, starting to cause a slight bias in mass and an increase in the statistical error. Also shown is the mass and the statistical error as a function of the sample purity c_1 . It can be seen that at purities below $\sim 20\%$ the method has difficulties to measure the mass in an unbiased way, while the statistical error decreases continuously with increasing sample purity. In addition, Figure (7.19) demonstrates by how much the calibrated measured mass distribution increases or decreases when varying the sample purity c_1 by one sigma around its measured value. More on these cross-checks is discussed in Chapter 8 on systematic uncertainties.

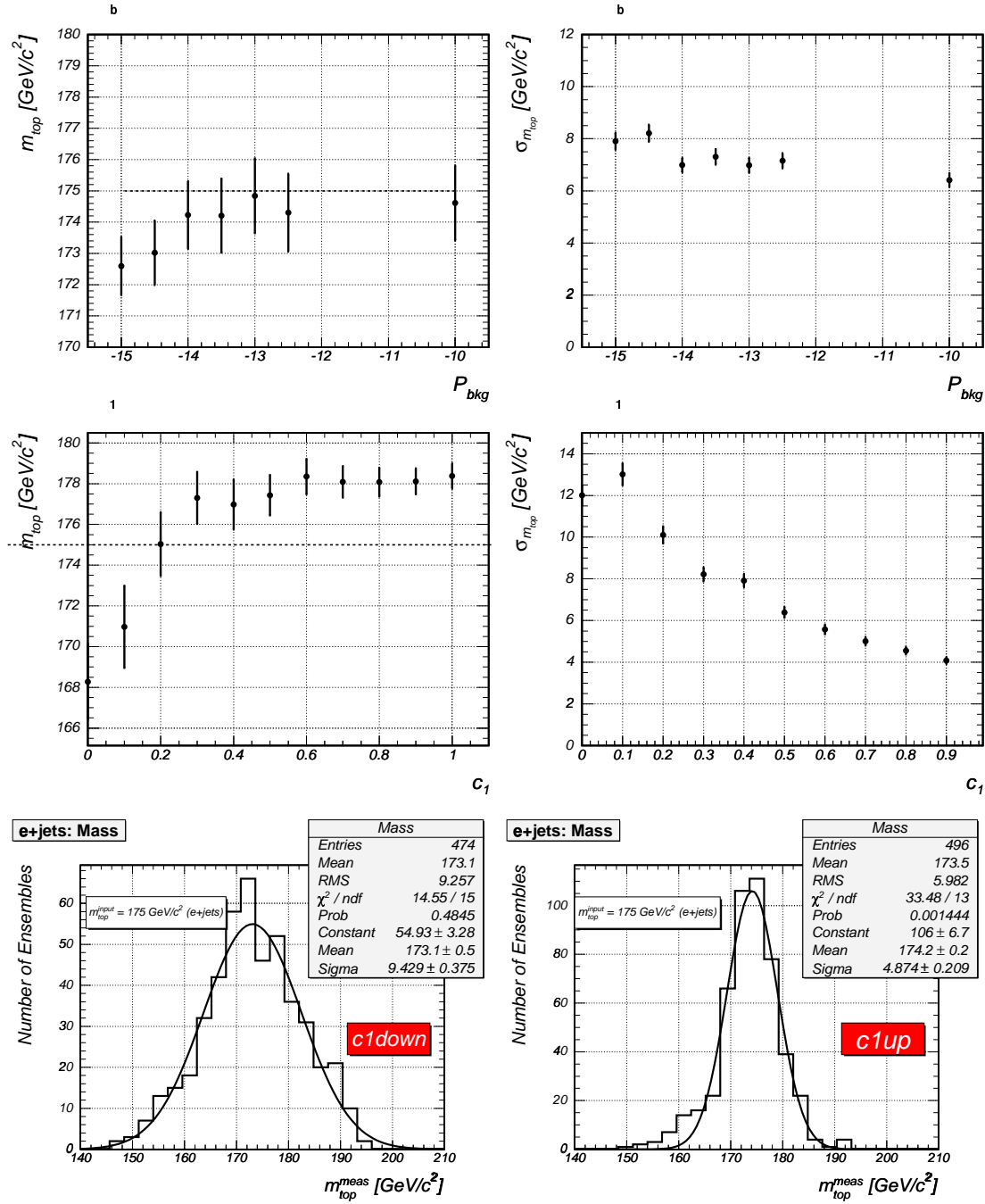


Figure 7.19.: $e + jets$ channel. Top: Calibrated measured mass (left) and statistical uncertainty (right) as a function of the background probability cut for the $175 GeV/c^2$ sample. Both are stable within $\pm 1 GeV/c^2$. **Middle:** Uncalibrated measured mass (left) and statistical error (right) as a function of the sample purity c_1 . As expected, the uncertainty increases with decreasing top contribution. **Bottom:** Corrected measured top mass for ensembles with the top purity increased (left) and decreased (right) by one sigma of the measured c_1 value.

$\mu + jets$ channel

For the $\mu + jets$ channel the ensemble tests are done following the same procedure as in the $e + jets$ channel. Again, the $t\bar{t}$ sample with a polemass of $175 \text{ GeV}/c^2$ is shown as an example. Figure (7.20) shows the distribution of the measured top mass, exhibiting a shift of $\sim 5 \text{ GeV}/c^2$, the distribution of the statistical errors with a mean of 5.6 GeV and the pull distribution with a mean of 0.08 ± 0.05 and a width of 1.08 ± 0.04 . This indicates that the error calculation is essentially unbiased and does not need any further correction.

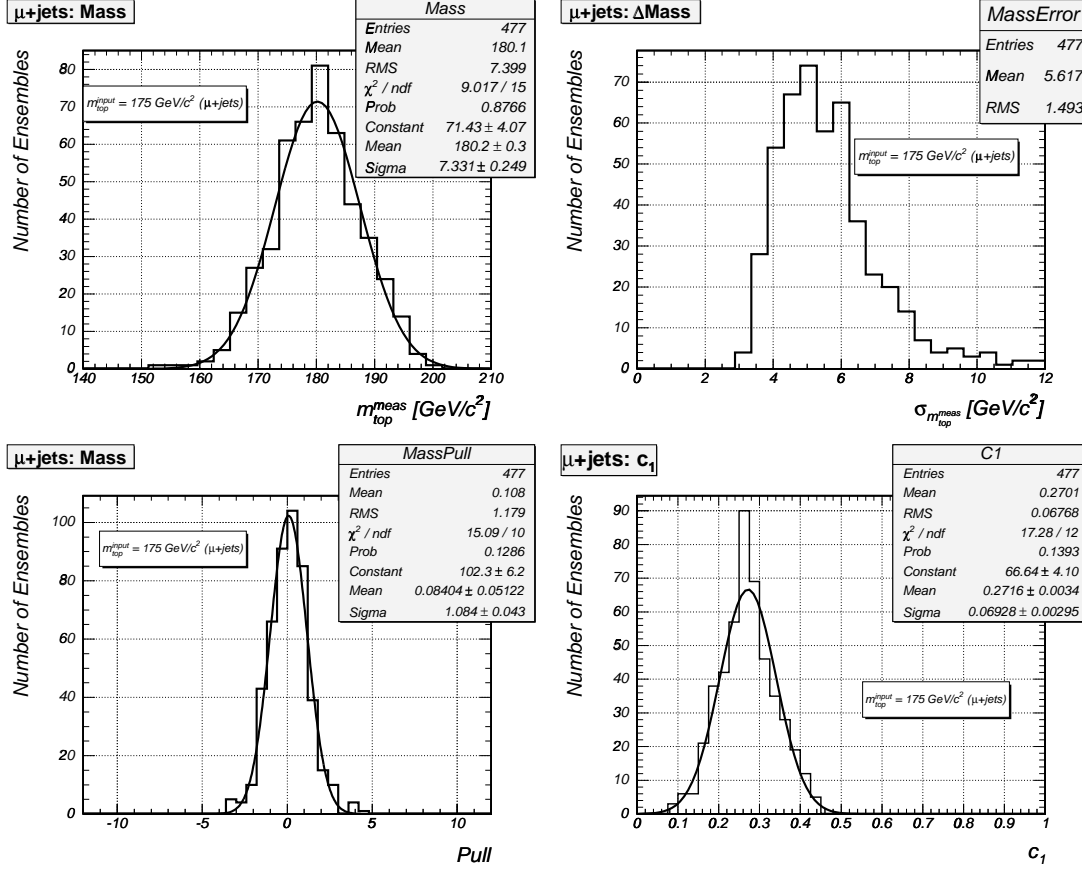


Figure 7.20.: **Top left:** Distribution of the uncorrected measured masses for 500 ensembles in the $\mu + jets$ channel. The gaussian fit gives a mean of $180.2 \pm 0.3 \text{ GeV}/c^2$ and a sigma of $7.33 \pm 0.25 \text{ GeV}/c^2$. **Top right:** Distribution of the statistical error as obtained from the likelihood. The mean is $5.6 \text{ GeV}/c^2$. **Bottom left:** Pull distribution. The gaussian fit gives a mean 0.08 ± 0.05 and a sigma of 1.08 ± 0.04 . **Bottom right:** Distribution of the estimated purity. The latter three plots are made after mass calibration.

Here, a straight line calibration of slope 1.19 ± 0.04 and an offset of $4.43 \pm 0.58 \text{ GeV}/c^2$ is observed and applied to the $\mu + jets$ data. The corresponding mass calibration curve is shown in Figure (7.21). Figure (7.21) also shows that the expected statistical uncertainty is $\sigma_{exp} \approx 6 \text{ GeV}/c^2$ before a correction is applied. The pull and c_1 distributions are shown in the bottom right plot of Figure (7.21).

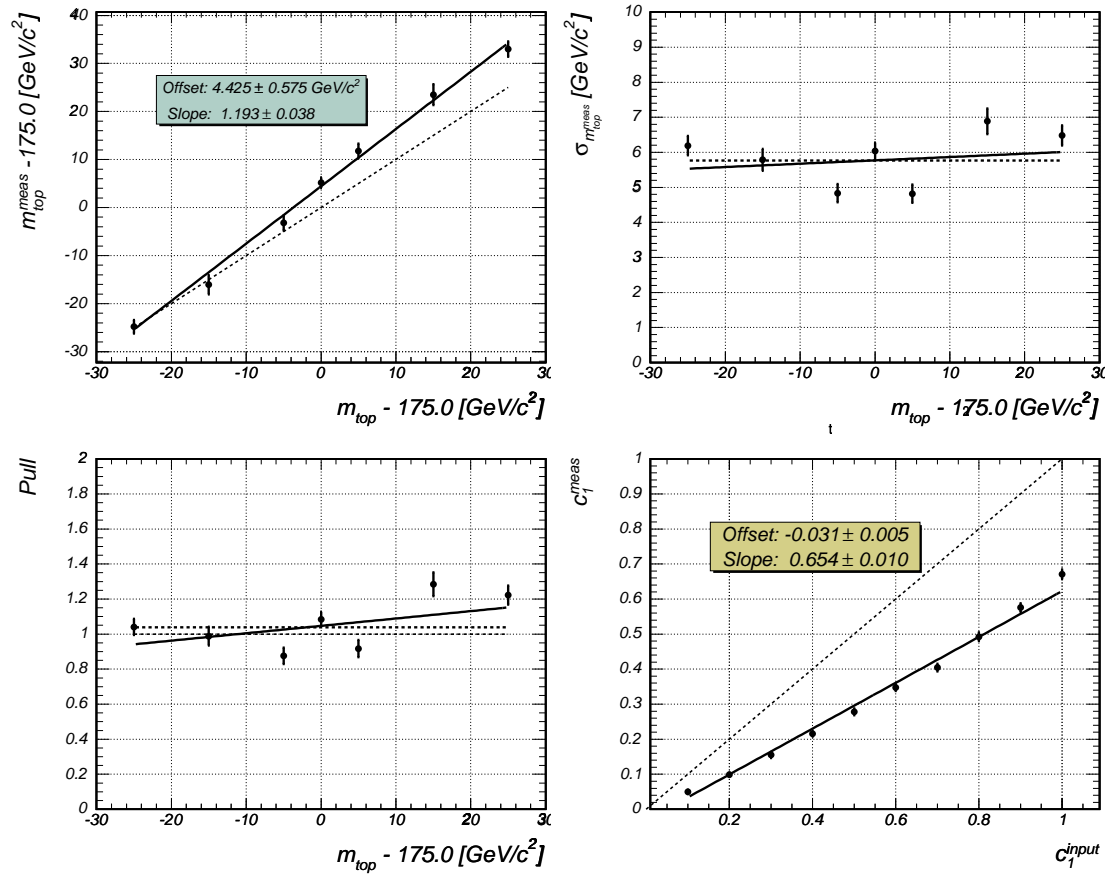


Figure 7.21.: $\mu + jets$ channel. **Top left:** Mass calibration, a linear correction of slope 1.19 and offset of $4.43 \pm 0.58 \text{ GeV}/c^2$ is observed. **Top right:** Statistical uncertainty as a function of the top mass. **Bottom left:** Width of the pull distribution as a function of the top mass. **Bottom right:** Measured c_1 as a function of the input purity.

In order to check the stability of the background probability cut, Figure (7.22) shows the measured mass and the statistical uncertainty as a function of the cut value for the $175 \text{ GeV}/c^2$ sample. The stability is good within an interval of $\pm 1 \text{ GeV}/c^2$ and is considered as a source of systematic uncertainty. Cutting at background probabilities of $10^{-14.5}$ or lower one starts cutting into the signal, starting to cause a slight bias in mass and an increase in the statistical error. Also shown is the mass and the statistical error as a function of the sample purity c_1 . It can be seen that at purities below $\sim 20\%$ the method has difficulties to measure the mass in an unbiased way, while the statistical error decreases continuously with increasing sample purity. In addition, Figure (7.19) demonstrates by how much the calibrated measured mass distribution increases or decreases when varying the sample purity c_1 by one sigma around its measured value.

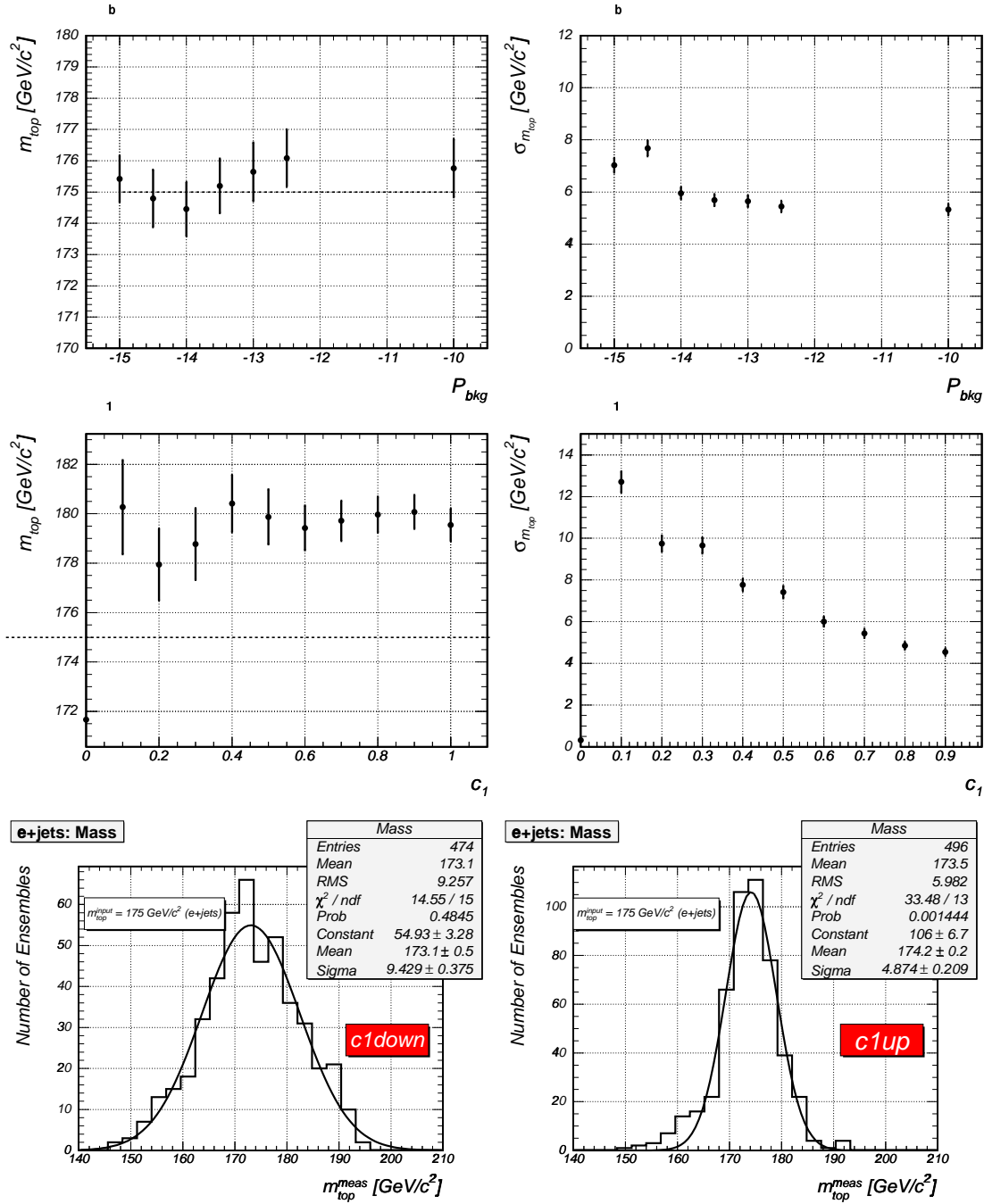


Figure 7.22: $\mu + jets$ channel. **Top:** Corrected measured mass (left) and statistical uncertainty (right) as a function of the background probability cut for the $175 GeV/c^2$ sample. Both are stable within $\pm 1 GeV/c^2$. **Middle:** Uncorrected measured mass (left) and statistical error (right) as a function of the sample purity c_1 . **Bottom:** Corrected measured top mass for ensembles with the top purity increased (left) and decreased (right) by one sigma of the measured c_1 value.

7.4. Application to Data

Having studied the method in reconstructed p14 Monte Carlo events it is applied to data in the following. The event selection is the same as described in Table (7.3). For e +jets and μ +jets a data set of 168.7 pb^{-1} and 158.4 pb^{-1} is analyzed respectively, yielding 49 e +jets candidates and 44 μ +jets candidates.

A data to Monte Carlo comparison of the most important variables is shown in Appendix E. The data to Monte Carlo comparison of the background probability distribution has been studied in some more detail, in particular with respect to improvements in the simulation of $W + 4 \text{ jets}$ events. Three sets of $W + 4 \text{ jets}$ Monte Carlo events are used for this comparison: $W + 4 \text{ jets}$ events without underlying events added in (the result of a bug in the ALPGEN generator), $W + 4 \text{ jets}$ events with the soft underlying event added according to the so-called tuneA parametrization, and $W + 4 \text{ jets}$ events with the soft underlying event added and lower parton level cuts on the generator level. The resulting distributions of the background probability are shown in Figure 7.23 and Figure 7.24 in comparison to the data for the e +jets and μ +jets channel, respectively.

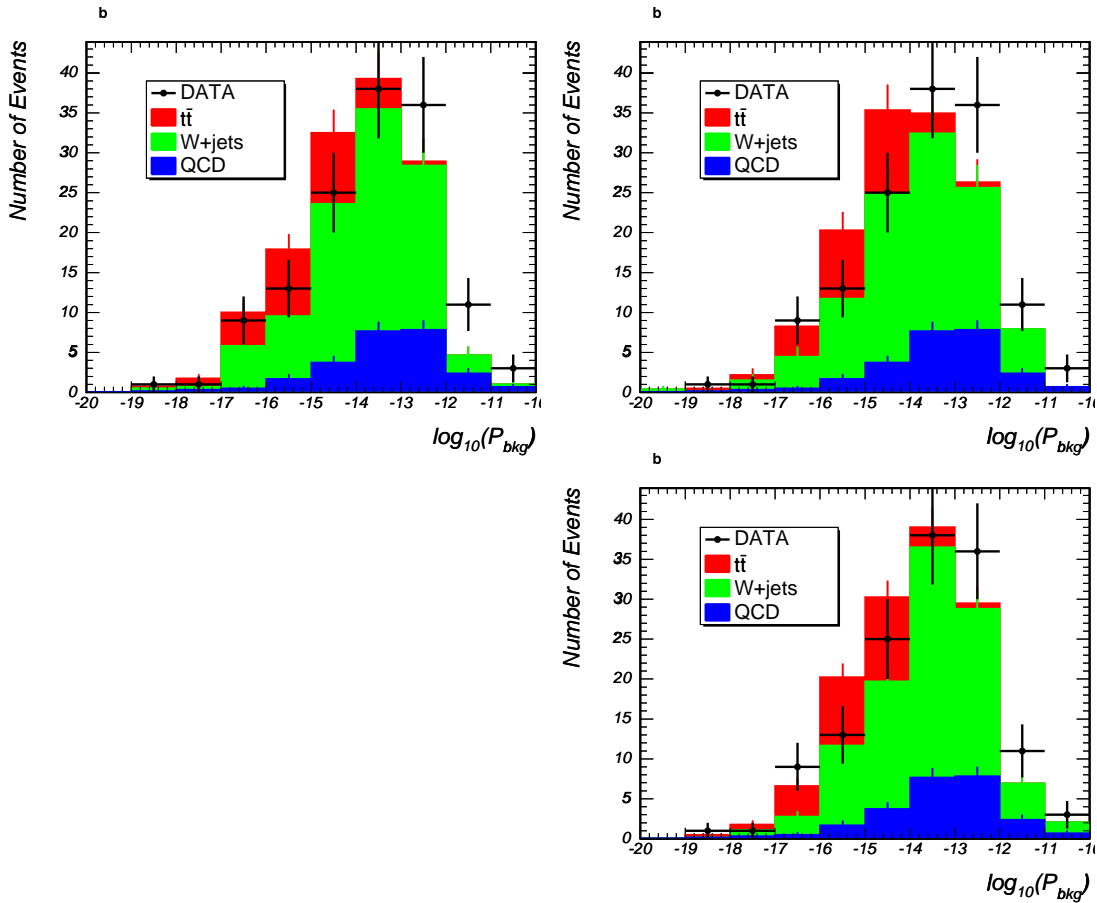


Figure 7.23.: Data to Monte Carlo comparison of the background probability distributions for $W + 4 \text{ jets}$ Monte Carlo without soft underlying event (**top left**), with soft-underlying event (**top right**), and with soft-underlying event for lower parton level cuts on the generator level (**bottom right**) in the e +jets channel.

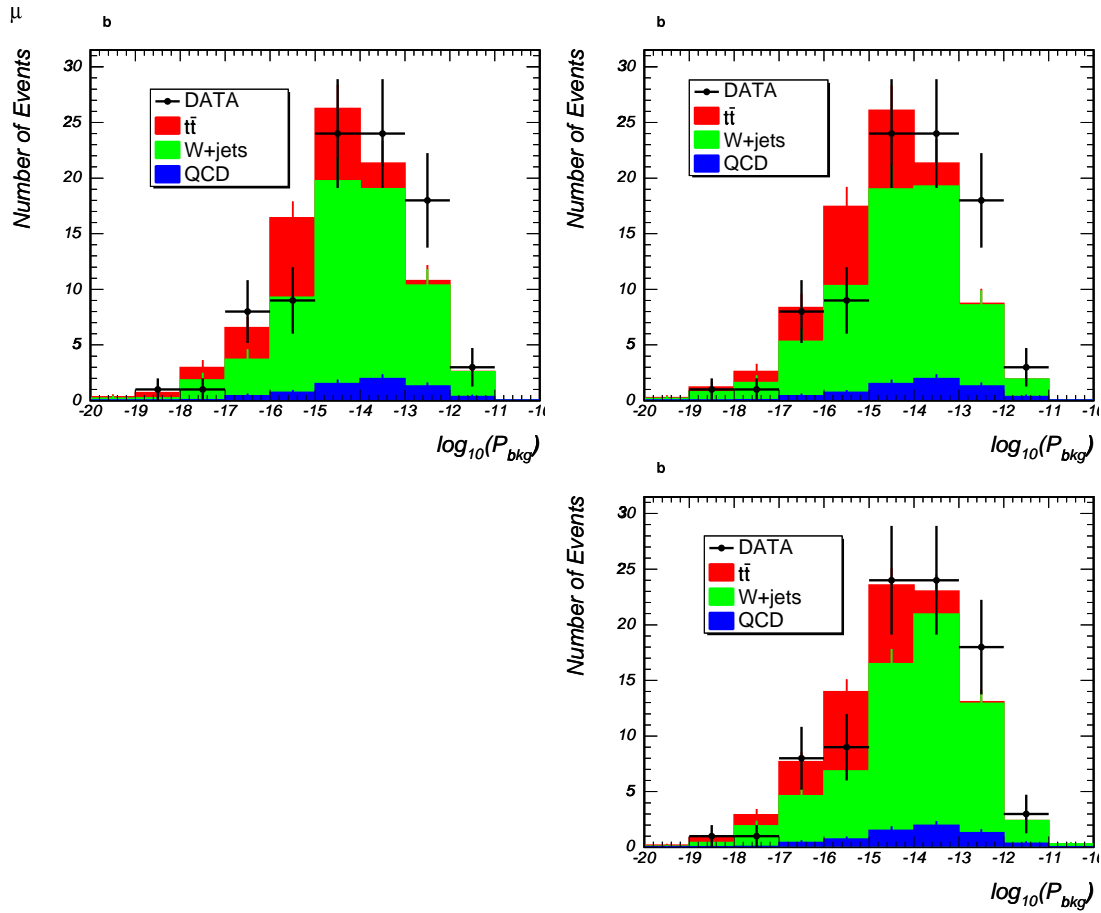


Figure 7.24.: Data to Monte Carlo comparison of the background probability distributions for $W + 4 \text{ jets}$ Monte Carlo without soft underlying event (**top left**), with soft-underlying event (**top right**), and with soft-underlying event for lower parton level cuts on the generator level (**bottom right**) in the $\mu + \text{jets}$ channel.

As can be seen from these plots, in the $e + \text{jets}$ and $\mu + \text{jets}$ channel the latest Monte Carlo events do give a good description of the data, also at high background probabilities, a background dominated region.

Applying the above described procedure to the selected $l + \text{jets}$ events, event likelihoods as a function of top mass hypotheses are obtained, where the top mass hypothesis is already corrected for the offset and slope observed in the ensemble testing using Monte Carlo events (see previous section). A 4th-order polynomial is fitted to the likelihood points in the likelihood minimum $^{+20}_{-10}$ GeV. Also shown is the likelihood as a function of the uncalibrated purity c_1 for the top mass hypothesis of the global likelihood minimum. The resulting c_1 value, after calibration, is the measure of the $t\bar{t}$ fraction in the selected data sample. Figures (7.25) and (7.26) show the corresponding plots for the $e + \text{jets}$ channel, Figures (7.27) and (7.28) for the $\mu + \text{jets}$ channel.

The results of the likelihood fits are summarized in Table (7.4).

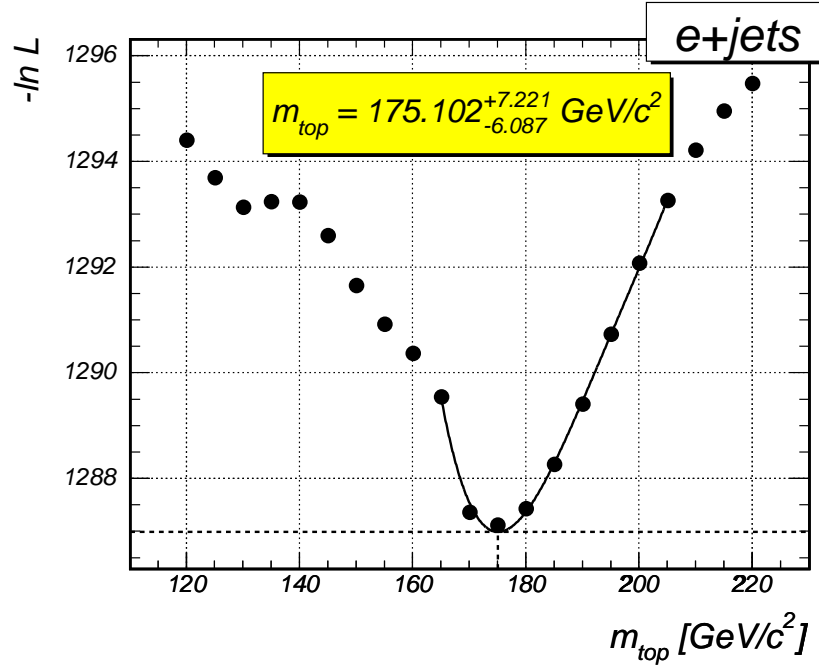


Figure 7.25.: Event likelihood as a function of the calibrated top mass hypothesis in the $e+jets$ channel.

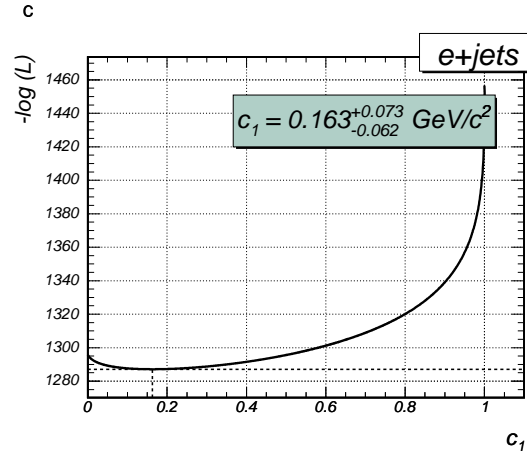


Figure 7.26.: Event likelihood as a function of the uncalibrated sample purity c_1 in the mass minimum for the $e+jets$ channel.

channel	mass fit	c_1 fit (uncalibrated)
$e+jets$	$175.1^{+7.2}_{-6.1} (stat.) \text{ GeV}/c^2$	$0.16^{+0.07}_{-0.06}$
$\mu+jets$	$170.1^{+11.8}_{-11.4} (stat.) \text{ GeV}/c^2$	$0.05^{+0.06}_{-0.04}$

Table 7.6.: Result of the likelihood fit with respect to the top mass and the purity c_1 in the $e+jets$ and the $\mu+jets$ channel.

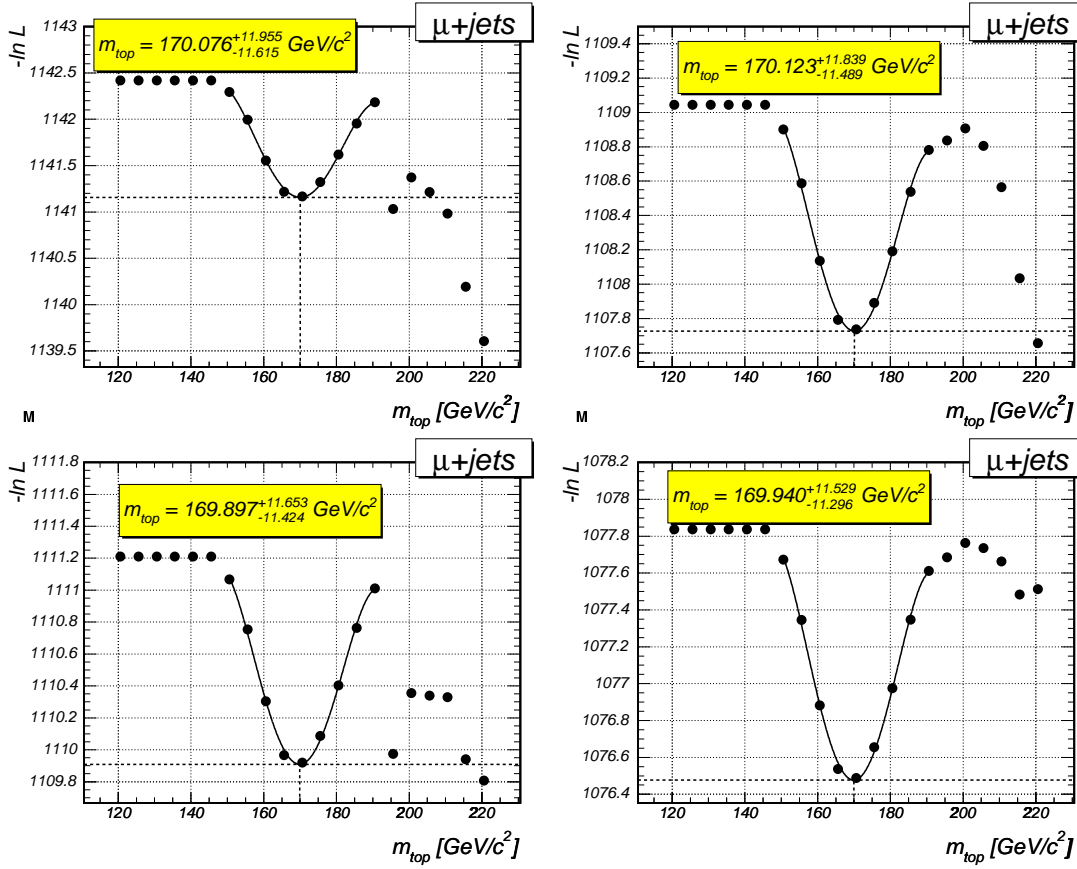


Figure 7.27.: Event likelihood as a function of the calibrated top mass hypothesis in the μ +jets channel. **Top left:** Likelihood including all μ +jets events. **Top right:** Likelihood without run 163527 event 12847872. **Bottom left:** Likelihood without run 179306 event 25499994. **Bottom right:** Likelihood without both aforementioned events.

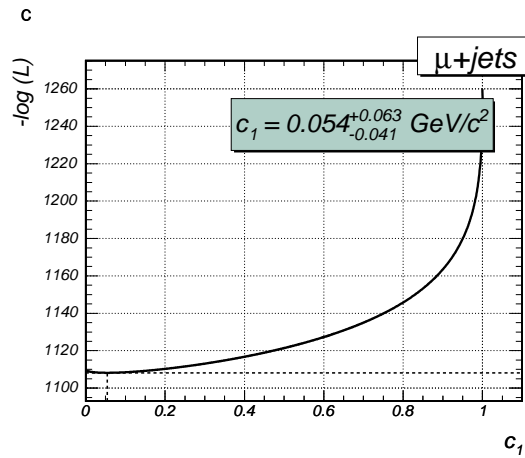


Figure 7.28.: Event likelihood as a function of the uncalibrated sample purity c_1 in the mass minimum for the μ +jets channel.

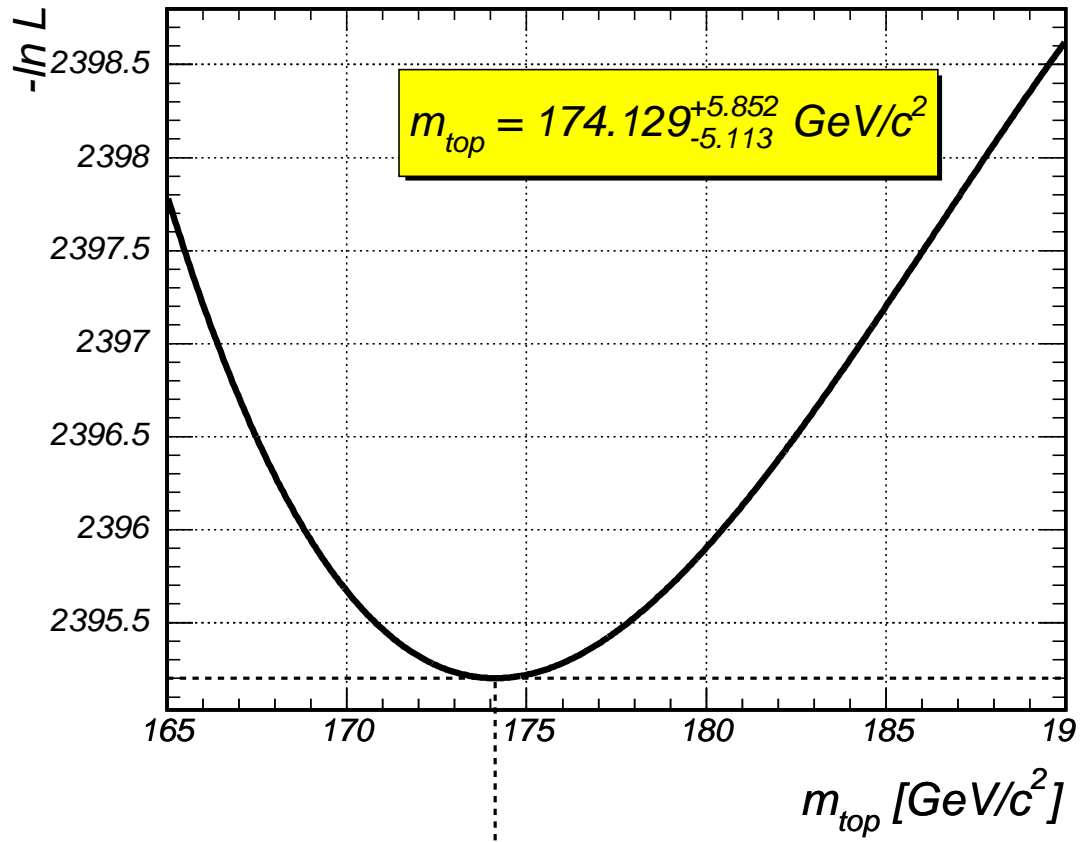


Figure 7.29.: Event likelihood as a function of the calibrated top mass hypothesis, combined for $e + jets$ and $\mu + jets$ channels by adding the likelihood curves.

The top mass for the combined sample is obtained from adding the likelihood fit curves obtained in the single channels and finding its minimum and its statistical error (Figure (7.29)). The top mass obtained from this combination procedure is

$$m_{top} = 174.1^{+5.9}_{-5.1}(stat.) \text{ GeV}/c^2 \quad (7.2)$$

7.4.1. Single Event Likelihoods and Muon Resolution

In case of the muon channel the likelihood “jumps” at values around $m_{top} = 200 \text{ GeV}/c^2$ and drops to larger values of top masses. After reviewing the single event likelihoods two events are found to give rise to this behaviour. Also, defined in the standard procedure of this analysis, events with a signal probability of 0 are removed. This does not happen in the $e + jets$ channel, but for 5 events in the $\mu + jets$ channel (one of these five events fails the background probability cut). It is concluded that the observed effects are due to the muon resolution and its parameterization by a δ -function. In principle an integration over the muon resolution has to be performed which is not done here in order to keep the CPU consumption in an acceptable limit.

Figure (7.30) shows the single likelihood curves of an event which caused the jump in the likelihood. For each plot the transverse momentum of the muon is changed with respect to the measured momentum in steps of $5 \text{ GeV}/c$. The measured value in this case is $p_T = 157.9 \text{ GeV}/c$ (top right), the variation ranges from $-15 \text{ GeV}/c$ to $+60 \text{ GeV}/c$ (for smaller transverse muon momenta the signal probability is zero). This variation is done in order to estimate the effect of considering the muon resolution. As can be seen the jump in the likelihood vanishes for higher muon momenta. Figure (7.31) shows the average of the likelihoods displayed. From this it can be concluded that an integration over the muon momentum would lead to continuous likelihood curves as is found in the case of electrons. The same argument holds for the events which had to be removed because the signal probability is zero.

Table (7.7) shows the kinematic properties of the two events which cause a jump in the likelihood curve and the strong drop off to higher top mass hypotheses. From the data to Monte Carlo comparison in Appendix E it can be seen that these two events are exceptional. The first one has a large transverse momentum of the muon (the largest in the data distribution), the second has large missing momentum (also the largest in the data distribution) and a very high transverse momentum of the leading jet.

	event 12847872 run 163527	event 25499994 run 179306
muon		
p_T	157.33 GeV	52.22 GeV
η	-0.47	0.66
ϕ	4.26	0.71
1.jet		
p_T	64.37 GeV	146.95 GeV
η	1.86	-0.48
ϕ	1.40	2.34
2.jet		
p_T	57.63 GeV	85.37 GeV
η	1.06	-0.04
ϕ	2.44	3.54
3.jet		
p_T	49.98 GeV	61.83 GeV
η	-1.32	-1.56
ϕ	6.25	4.93
4.jet		
p_T	24.61 GeV	58.92 GeV
η	-0.81	0.09
ϕ	0.59	4.61
missing E_T	25.48 GeV	126.29 GeV
H_T	343.62 GeV	523.33 GeV
$\log_{10}(p_{bkg})$	-18.07	-17.13

Table 7.7.: Kinematic properties of the two events causing jumps and a drop off at higher masses.

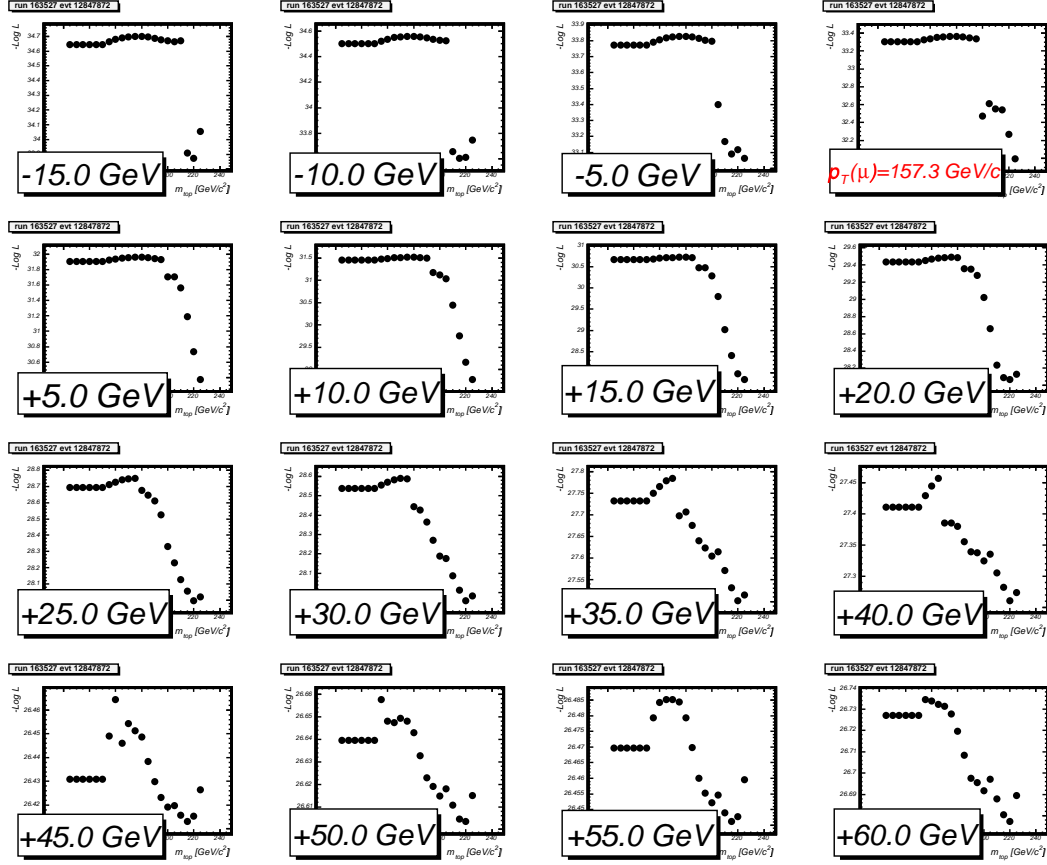


Figure 7.30.: Likelihood for event 12847872, run 163527 for different values of muon momentum, estimating the effect of the finite muon resolution. For large values of the muon momentum the jump in the likelihood vanishes.

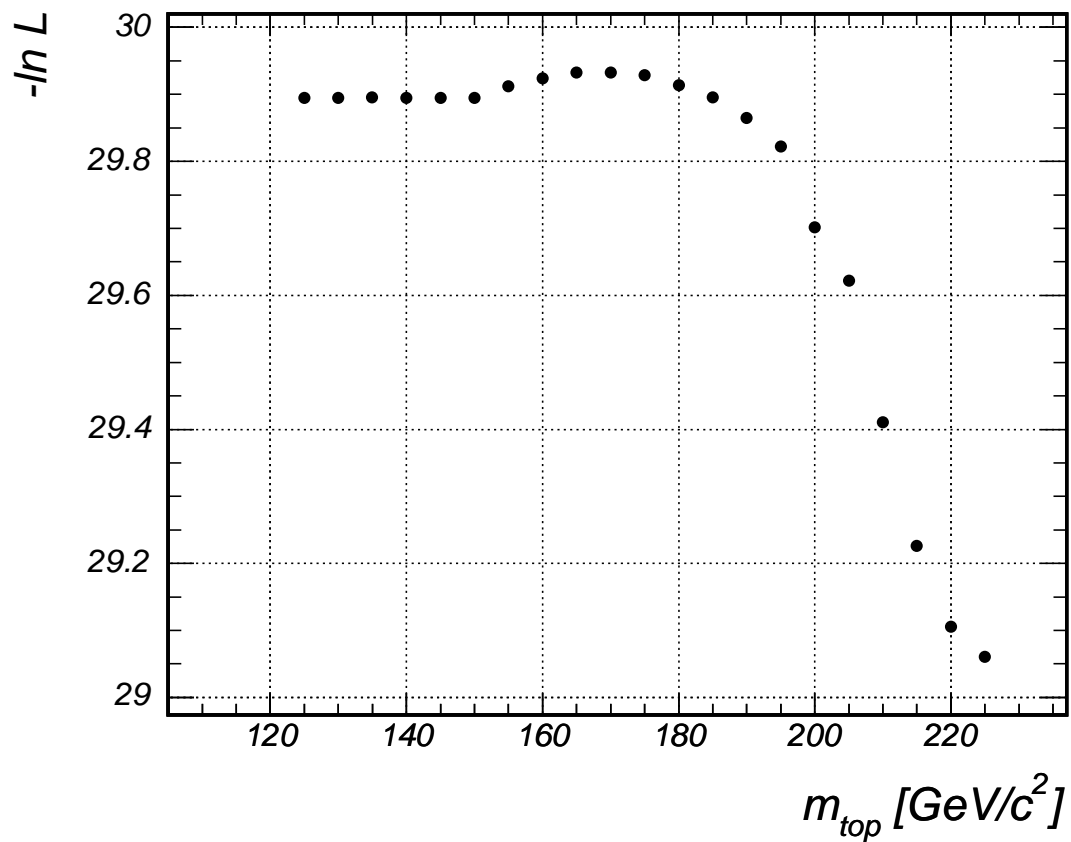


Figure 7.31.: Likelihood for event 12847872, run 163527 averaged over the muon momenta in Figure (7.30). This estimates the effect of an integration over the muon momentum.

7.4.2. Event Display

As an example for the $t\bar{t}$ candidate events in data several event displays are shown in Figure (7.32) for run 180402, event 4558647. On the top left, the likelihood curve for that specific event is shown together with its kinematic properties.

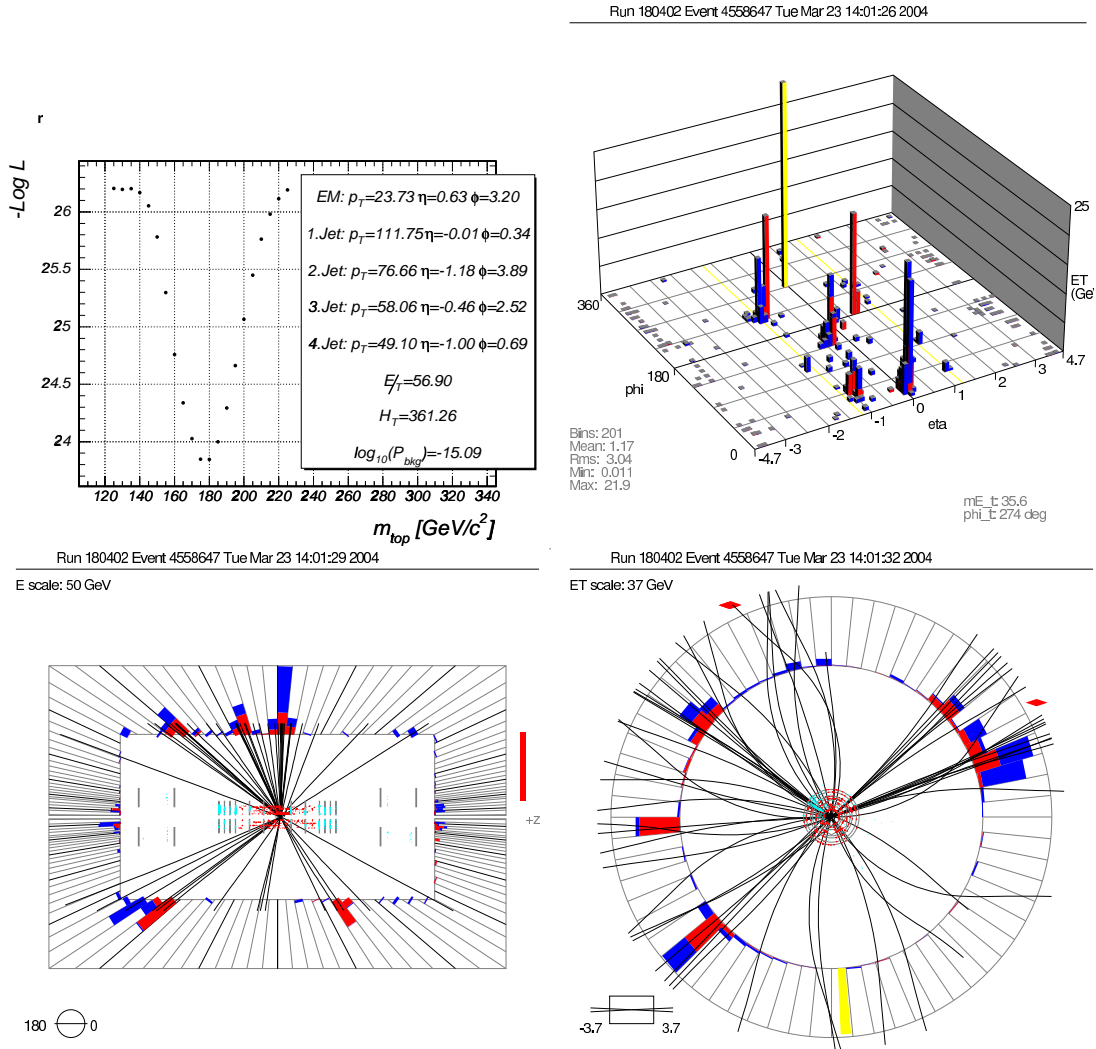


Figure 7.32.: Example for a $t\bar{t}$ candidate event (run 180402, event 4558647). **Top left:** Likelihood as obtained from the data sample. **Top right, bottom:** Event Displays in different views.

8. Systematic Uncertainties

In the following the systematic uncertainties on the top mass measurement are discussed. The procedure to estimate the uncertainty is to redo the Monte Carlo calibration for the sample with a top mass of $175 \text{ GeV}/c^2$ including a systematic variation. The difference between the measured mass in the varied and not varied sample is quoted as systematic uncertainty, assuming only the offset of the calibration straight line to change, not the slope. Details on the estimation of the systematic uncertainties are discussed in [26].

The major uncertainties are the jet energy scale (JES) and the modelling of the signal and background. The results are summarized in Table (8) and combined by adding all uncertainties in quadrature.

Calibration Correction Since the mass calibration curve is not consistent with a slope of 1 and an offset of $0 \text{ GeV}/c^2$ a linear correction is applied to the measured mass. Due to the limited statistics of the Monte Carlo samples the maximal fluctuation around the input mass is quoted as systematic uncertainty. From the Figures (7.18) and (7.21) the errors are estimated to be:

$$\begin{aligned}\Delta M_{calib}^{e+jets} &= \pm 3.5 \text{ GeV}/c^2, \\ \Delta M_{calib}^{\mu+jets} &= \pm 3.5 \text{ GeV}/c^2.\end{aligned}\tag{8.1}$$

Likelihood Fit Procedure The likelihood as a function of the top mass hypothesis is fit to a 4th order polynomial. Since the likelihood does not perfectly follow the shape of a parabola or a 4th order polynomial (due to non-gaussian error contributions) the likelihood is only fit in a certain mass window around its minimum. Varying the fit range by $\sim \pm 10 \text{ GeV}/c^2$ on the lower and the upper mass range independently allows to quantify the sensitivity of the fit central mass to the chosen mass range. The corresponding error estimates are:

$$\begin{aligned}\Delta M_{fit}^{e+jets} &= \pm 0.5 \text{ GeV}/c^2, \\ \Delta M_{fit}^{\mu+jets} &= \pm 0.5 \text{ GeV}/c^2.\end{aligned}\tag{8.2}$$

Jet Energy Scale The uncertainty on the mass measurement due to the uncertainty of the jet energy scale (JES) is studied by varying the energy of all jets. This is done for the $175 \text{ GeV}/c^2$ sample. The jets in $t\bar{t}$ as well as in $W + 4 \text{ jets}$ events are rescaled up and down according to the quoted uncertainty (5% for high transverse p_T , increasing linearly for values lower than $30 \text{ GeV}/c$) after application of the parton level and η -dependent correction. The uncertainty on the JES is parameterized the following way:

$$\begin{aligned}
p_T < 30 \text{ GeV}/c : \Delta E &= 0.3 + p_T \cdot (0.05 - 0.3)/30\%, \\
p_T > 30 \text{ GeV}/c : \Delta E &= 0.05\%,
\end{aligned} \tag{8.3}$$

where p_T and E are the transverse momentum and energy of a single jet. Details on the JES can be found in [37].

The differences of both scaled samples are quoted as a systematic uncertainty for each channel separately. For $e + jets$ and $\mu + jets$ they are found to be:

$$\begin{aligned}
\Delta M_{JES}^{e+jets} &= \pm 9.0 \text{ GeV}/c^2, \\
\Delta M_{JES}^{\mu+jets} &= \pm 9.0 \text{ GeV}/c^2.
\end{aligned} \tag{8.4}$$

Jet Energy Resolution The resolution of the jet energy has been measured in data and MC. The MC jet energy resolution is smeared according to the data, but that procedure also has some uncertainties. Varying the jet energy resolution smearing in Monte Carlo according to its uncertainties propagates via a new offset in the calibration straight line to a corresponding uncertainty on the mass of (see Figure (8.1)):

$$\begin{aligned}
\Delta M_{JER}^{e+jets} &= {}^{+1.5}_{-1.0} \text{ GeV}/c^2, \\
\Delta M_{JER}^{\mu+jets} &= {}^{-1.0}_{-3.0} \text{ GeV}/c^2.
\end{aligned} \tag{8.5}$$

Purity of the Sample In order to estimate the influence of the purity of the sample, the fraction signal events in Table (7.5) are varied in the ensemble composition according to the specified error of c_1 (see Figure (8.2)). Ensemble tests for the 175 GeV/ c^2 sample are done and the maximal variation in the mass is quoted as a systematic uncertainty:

$$\begin{aligned}
\Delta M_{purity}^{e+jets} &= \pm 0.5 \text{ GeV}/c^2, \\
\Delta M_{purity}^{\mu+jets} &= \pm 0.5 \text{ GeV}/c^2.
\end{aligned} \tag{8.6}$$

Signal and Background Model Since it is a priori unclear how well the assumed model describes the data, further studies have to be done. As a first step, a data to Monte Carlo comparison is done (see Appendix E). Reasonable to good agreement between the most important variables is found. For the study of the background and signal models, different matrix elements (higher order) and shower simulations like HERWIG or ISAJET should be compared. Since none of the above quoted Monte Carlo is available the uncertainty is estimated from the studies done in the Run I [32], and inflated by a factor of 2 to be conservative:

$$\begin{aligned}
\Delta M_{sgnmodel}^{e+jets} &= \pm 2 \times 1.1 \text{ GeV}/c^2, \\
\Delta M_{sgnmodel}^{\mu+jets} &= \pm 2 \times 1.1 \text{ GeV}/c^2.
\end{aligned} \tag{8.7}$$

$$\begin{aligned}
\Delta M_{bkgmodel}^{e+jets} &= \pm 2 \times 1.0 \text{ GeV}/c^2, \\
\Delta M_{bkgmodel}^{\mu+jets} &= \pm 2 \times 1.0 \text{ GeV}/c^2.
\end{aligned} \tag{8.8}$$

Multi Parton Interactions Because of a bug in the ALPGEN Monte Carlo generator, multi parton interactions were not included in the simulation of $t\bar{t}$ signal samples. Those are the samples used to derive the mass calibration. The 175 GeV/c² sample was re-generated with soft underlying events included and the analysis is repeated for that particular sample. The difference in the measured mass at 175 GeV/c² is quoted as an uncertainty due to the influence of multi parton interactions on the signal sample (see right hand side of Figure (8.3)):

$$\begin{aligned}\Delta M_{MPI}^{e+jets} &= \pm 1.0 \quad \text{GeV/c}^2, \\ \Delta M_{MPI}^{\mu+jets} &= \pm 2.0 \quad \text{GeV/c}^2.\end{aligned}\tag{8.9}$$

Transfer Functions The transfer functions defined in the previous sections are derived from $t\bar{t}$ Monte Carlo events with a jet-parton-matching requirement. The obtained parameters are varied within the error from the fit and the distribution of invariant masses was used to estimate a systematic uncertainty due to the transfer functions:

$$\begin{aligned}\Delta M_{TF}^{e+jets} &= \pm 1.0 \quad \text{GeV/c}^2, \\ \Delta M_{TF}^{\mu+jets} &= \pm 1.0 \quad \text{GeV/c}^2.\end{aligned}\tag{8.10}$$

Acceptance Corrections Due to the limited statistics for the acceptance corrections a second set of parameters for the polynomial is derived, mainly propagating the uncertainty in the overall normalization of the acceptance. The systematic uncertainty due to the parameterization is quoted as:

$$\begin{aligned}\Delta M_{acc}^{e+jets} &= \pm 0.1 \quad \text{GeV/c}^2, \\ \Delta M_{acc}^{\mu+jets} &= \pm 0.1 \quad \text{GeV/c}^2.\end{aligned}\tag{8.11}$$

Muon Resolution In the calculation of the event probabilities, a perfect measurement of the charged lepton energy is assumed. This is essentially a good approximation for electrons due to the resolution of the calorimeter. However, the resolution for muons is worse and therefore effects on the mass are studied in Monte Carlo. This is done by replacing the reconstructed muon by the generated muon, i.e. making use of the parton level information. Ensemble tests for the 175 GeV/c² sample are performed yielding an uncertainty due to the finite resolution of the muon of:

$$\Delta M_{muon}^{\mu+jets} = \pm 1.8 \text{ GeV/c}^2.\tag{8.12}$$

Background Probability Cut The cut on the background probability, previously shown to be stable with respect to the mass and the systematic uncertainty, is varied in the data set. The maximal difference between the minima is quoted as a systematic uncertainty. As expected, a stronger cut on the background probability increases the signal significance.

$$\begin{aligned}\Delta M_{acc}^{e+jets} &= \pm 2.0 \quad \text{GeV/c}^2, \\ \Delta M_{acc}^{\mu+jets} &= \pm 2.0 \quad \text{GeV/c}^2.\end{aligned}\tag{8.13}$$

Trigger Turn On Because the parameterization of the trigger turn on curves is also afflicted with uncertainties, it is also a source of systematic uncertainties. Varying the L3 turn on curves for jets by 1σ results in an uncertainty of:

$$\begin{aligned}\Delta M_{acc}^{e+jets} &= \pm 0.5 \text{ GeV}/c^2, \\ \Delta M_{acc}^{\mu+jets} &= \pm 0.5 \text{ GeV}/c^2.\end{aligned}\tag{8.14}$$

Calibration error due to TuneA bug The mass calibration curves are obtained for the $W + 4\text{ jets}$ Monte Carlo generated with lower parton level cuts and including soft underlying events. In tests it could be shown that the slope and offset of these curves is the same, when the sample with the tuneA bug is used. Therefore it can be concluded that, in case of the background, the method is not sensitive to this bug. And no systematic uncertainty is quoted.

Summary and Combination

Table (8) summarizes the systematic uncertainties in both, the $e + \text{jets}$ and the $\mu + \text{jets}$ channel. Since the errors are assumed to be not correlated they are added in quadrature.

Uncertainty	$e + \text{jets}$ [GeV/ c^2]	$\mu + \text{jets}$ [GeV/ c^2]
Calibration procedure	± 3.5	± 3.5
Likelihood fit procedure	± 0.5	± 0.5
Jet energy scale	± 9.0	± 9.0
Jet energy resolution	$+1.5$ -1.0	-1.0 -3.0
Purity of the sample (c_1 variation)	± 0.5	± 0.5
Signal model	± 2.2	± 2.2
Background model	± 2.0	± 2.0
Multi parton interactions	± 1.0	± 2.0
Transfer functions	± 1.0	± 1.0
Acceptance corrections	± 0.1	± 0.1
Muon resolution	-	± 1.8
Background probability cut	± 2.0	± 2.0
Trigger turn on	± 0.5	± 0.5
Total systematic uncertainty	$+10.5$ -10.5	$+10.7$ -11.1

Table 8.1.: Summary of the systematic uncertainties in the $e + \text{jets}$ and $\mu + \text{jets}$ channel.

The total systematic uncertainties are found to be:

$$\begin{aligned}\Delta M_{sys}^{e+jets} &= \begin{matrix} +10.5 \\ -10.5 \end{matrix} \text{ GeV}/c^2, \\ \Delta M_{sys}^{\mu+jets} &= \begin{matrix} +10.7 \\ -11.1 \end{matrix} \text{ GeV}/c^2.\end{aligned}\tag{8.15}$$

The following figures show examples of the mass distributions which are used to estimate the systematic uncertainties.

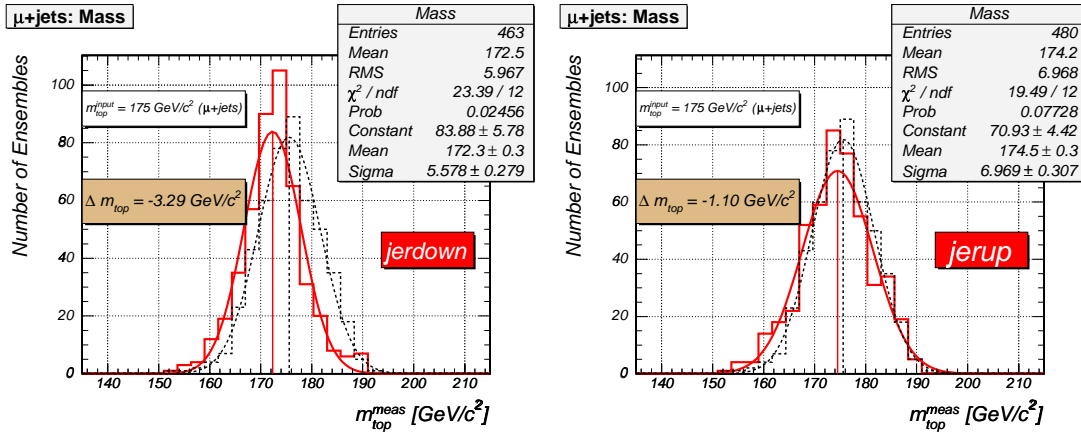


Figure 8.1.: Variation of the jet energy resolution in the $\mu + jets$ channel.

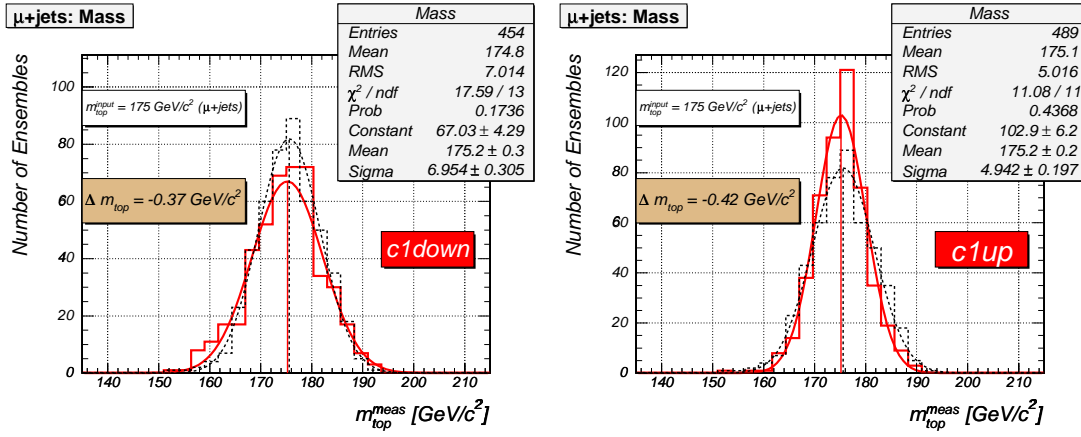


Figure 8.2.: Variation of the $t\bar{t}$ fraction (c_1) according to the errors estimated with the 2nd matrix method in the $\mu + jets$ channel.

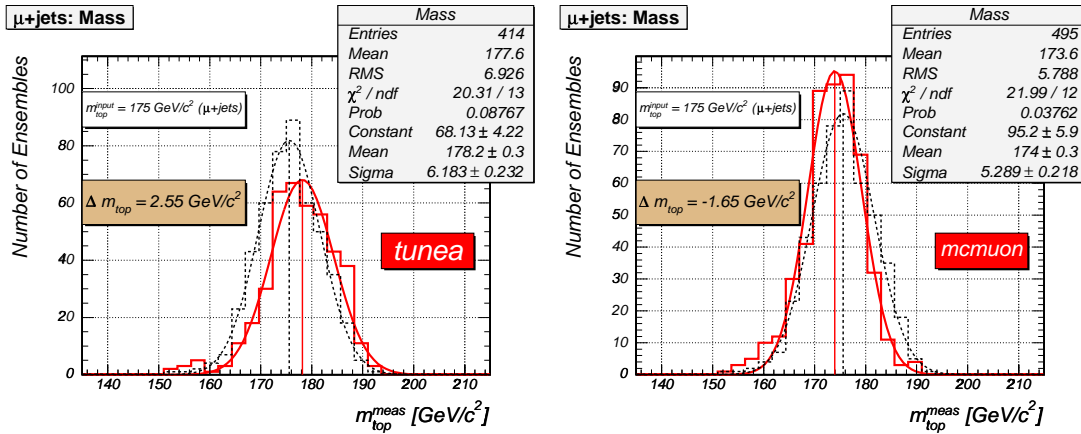


Figure 8.3.: **Left:** Mass distribution for ensembles with and without soft underlying events in the $t\bar{t}$ and $W + 4 jets$ samples. **Right:** Mass distribution with and without Monte Carlo muon. This is done in order to test the sensitivity to a systematic error due to the muon resolution.

Reweighting and shifting the $W + 4 \text{ jets}$ contribution.

Because the background probability distribution in data is not perfectly described by the Monte Carlo two further cross checks have been done. Assuming that the discrepancy is caused by the $W + 4 \text{ jets}$ contribution (which dominates the sample) the $W + 4 \text{ jets}$ events are reweighted by a factor obtained from a bin-by-bin comparison of the distribution. The ensemble tests are redone for the weighted sample and led to only small shifts ($\sim \pm 0.5 \text{ GeV}/c^2$) in the distribution of measured masses and is accounted for in the error on the background probability.

Additionally, the $W + 4 \text{ jets}$ Monte Carlo distribution was shifted towards higher values of background probability in order to test the assumption that the entire discrepancy originates from mismodeling of the $W + 4 \text{ jets}$ events. The distribution was fitted to the data and a χ^2 as function of the shift is minimized yielding

$$\begin{aligned}\Delta \ln p_{bkg}^{e+jets} &= 0.44, \\ \Delta \ln p_{bkg}^{\mu+jets} &= 0.30.\end{aligned}$$

Figure (8.4) shows a comparison between data and the shifted distributions for the $\mu + \text{ jets}$ channel. It should be mentioned that only the $W + 4 \text{ jets}$ contribution is shifted, QCD and $t\bar{t}$ are not shifted.

The ensemble tests are redone for the shift values minimizing the χ^2 and yield no significant difference. Figure (8.5) shows the distribution of measured masses for the ensemble tests with reweighted and shifted $W + 4 \text{ jets}$ contributions.

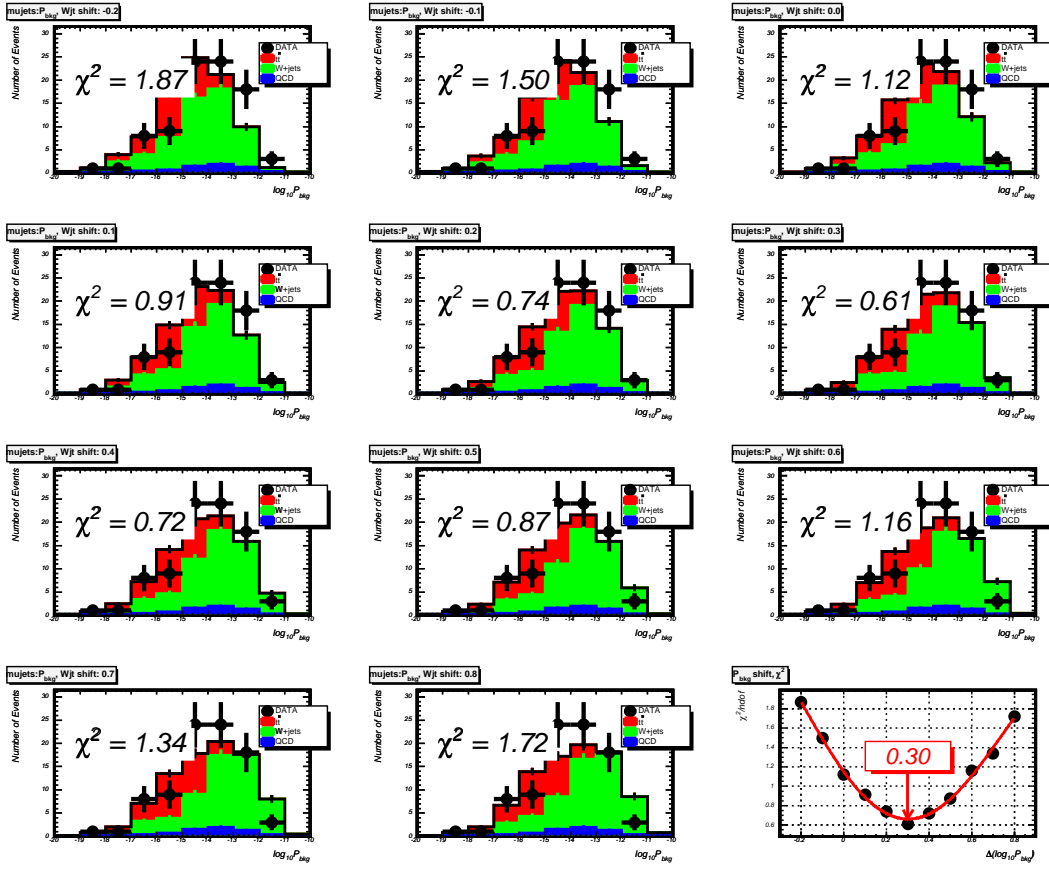


Figure 8.4.: Comparison between data and Monte Carlo for the background probability in the $\mu + \text{jets}$ channel. The $W + 4\text{ jets}$ contribution is shifted and fitted to the data. The plot on the lower right shows the χ^2 as function of the shift value.

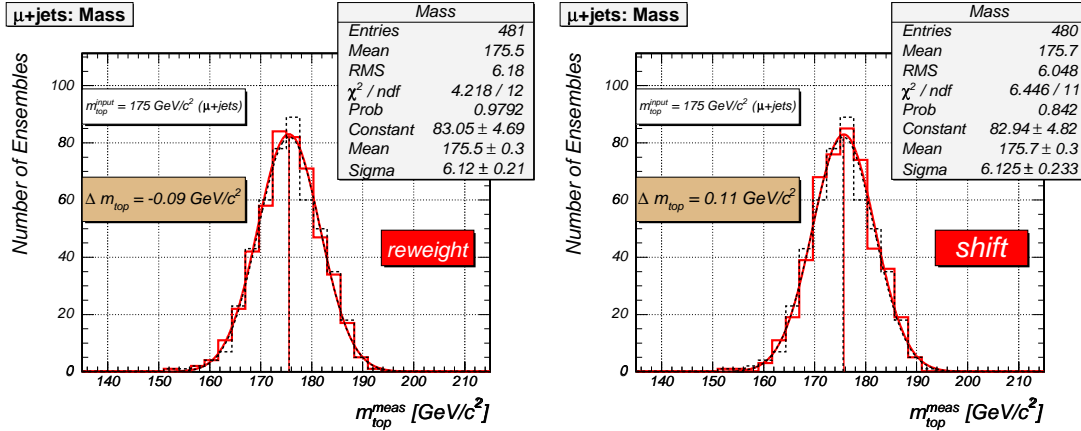


Figure 8.5.: Left: Mass distribution for the ensemble tests with weighted $W + 4\text{ jets}$ contribution in the $\mu + \text{jets}$ channel. The difference is accounted for in the uncertainty for the background probability cut. Right: Mass distribution for the shifted $W + 4\text{ jets}$ contribution.

9. Conclusion and Outlook

The following sections conclude and summarize the analysis presented. Plans for further improvements of the method itself and the analysis are presented.

9.1. Final Result

A method to measure the top quark mass with great statistical power has been introduced. It is based on the theoretical knowledge of the processes involved and makes maximal use of the kinematic properties as well as the resolution of the detector. Due to the assumption of the Standard Model production and decay processes the statistical error decreases compared to alternative approaches [32]. The application on the mass measurement was already shown in the Run I of the Tevatron and with the present analysis it is established in the Run II. With the current data set of roughly 150 pb^{-1} it yields a top quark mass in the lepton + jets channel of

$$m_{top} = 174.1_{-5.1}^{+5.9} (stat.)_{-10.5}^{+10.5} (syst.) \text{ GeV}/c^2. \quad (9.1)$$

Figure (9.1) shows a comparison of the results obtained during the Run I of the Tevatron and this analysis.

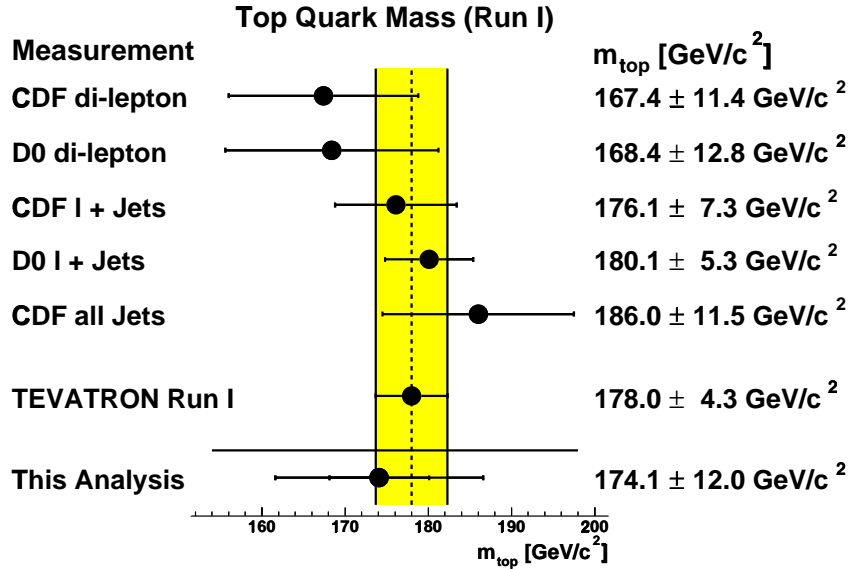


Figure 9.1.: Comparison of the results obtained during the Run I of the Tevatron and this analysis.

9.2. Outlook: Plans, Improvements and Comparison to Run I

The measurement of the top quark mass is presented using the Matrix Element Method. Since the introduced approach is statistically very powerful the systematic uncertainties are the dominant contribution to the error on the mass. In the following, approaches for further improvement are briefly discussed. Subsequently, a comparison to the Run I analysis is presented.

Method Specific Improvements

Several method specific modifications could lead to an improvement of the mass measurement. These include

- b-tagging: Algorithms to identify b-jets are already used in various analyses, for example [38, 39]. These could be used for two purposes. One is to further suppress background events in the preselected data sample, since the fraction of b-jets in $W + 4 \text{ jets}$ and QCD events is rather small. Second, the possible jet-parton combinations can be decreased or weighted according to a b-jet probability. This would reduce the combinatorial background. Technically, these features are already implemented in the code of this analysis, but have to be studied in more detail.
- As can be seen in the next chapter, track jet information can be used in order to further increase the statistics and also improve the quality of jets.
- The matrix element (and PDFs accordingly) are calculated in leading order and do therefore not include virtual loop corrections or 5 jet contributions. Including these into the analysis would improve the modelling of the signal and background.
- Intensive studies of the transfer functions can be found in [26]. It can be shown that the transfer functions for quarks are significantly different from gluon transfer functions (as needed in the $W + 4 \text{ jets}$ case). The latter could be used for the calculation of the background probability.
- As mentioned in the analysis, the muon energy resolution is not perfectly described by a delta-function as assumed by the method. An additional integration (including a set of muon-transfer functions) does improve the mass resolution as can be seen in the Run I analysis [32].
- In this study, the missing energy measured by the detector is not used in the calculation of momenta. The transverse momentum of the neutrino is therefore derived from momentum balance. Including the measured quantity might complete the information content in such a way that the whole available kinematic information is used. If this improves the precision or increases the dependence on systematic uncertainties needs to be studied.
- Since the Matrix Element Method so far does only account for $t\bar{t}$ and $W + 4 \text{ jets}$ probabilities, additional terms for QCD and noise jets could slightly improve the measurement. In the moment, these effects are averaged out but can be studied further.

General Improvements

Due to the large systematic uncertainties several issues of interest for many analyses should be addressed. These are:

- The jet energy scale is the most dominant source of systematic uncertainties. A further confinement of its error would not only improve the mass measurement but is also important for analyses which rely on the quality of jets. One way to improve this quantity could be to derive a flavor dependent jet energy scale. Studies addressing this issue are in progress.
- The modelling of the data with Monte Carlo events (especially the $W + 4 \text{ jets}$ background) is the second largest uncertainty in the analysis. As a data to Monte Carlo comparison shows (Appendix E, in more detail see [26]), further improvement is needed.

Comparison to the Run I Analysis

The Matrix Element Method has been introduced in the Run I of the Tevatron. With the present analysis it has been established in the Run II following the Run I analysis. A few changes have been made. These are

- The matrix element used in the present analysis does include contributions from $q\bar{q} \rightarrow t\bar{t}$ and $gg \rightarrow t\bar{t}$. Also, the spin-correlations between top and antitop are taken into account. Previously, these were not accounted for.
- Technically, the integration over the 5 remaining degrees of freedom is performed with different variables than in Run I. Details on the numerical techniques can be found in Appendix B.
- The possibility of b-tagging is implemented in the framework of the analysis as well as the chance of measuring the hadronic W-mass instead of or in addition to the top mass.
- For the time being, the energy resolution for muon and electron are treated as perfect (delta-functions). From additional muon studies it is known that the former resolution is not adequately described by delta-functions, as assumed here. In the Run I analysis an additional integration over the muon energy was carried out.
- As shown in Section (5.1) the transfer functions used in this analysis are broader than the ones used in the previous analysis. This is due to the calorimeter resolution in Run II, a result of the new tracker and the solenoid coil, and increases the statistical uncertainty on the mass measurement.

10. Further Improvements: A Jet Study

For the measurement of the top quark mass, not only a good jet reconstruction efficiency is needed, but also a good quality of the jets is required. For that purpose a Monte Carlo study of the $t\bar{t}$ samples is done in the reconstruction version p13. It addresses the question if tracking information can be used in order to increase the quality and efficiency of jets, and therefore the purity of the sample. For this study the $e + jets$ channel was studied exclusively since it is expected that the $\mu + jets$ channel behaves in an analog way because only properties of jets are studied.

As a first approach the samples are studied with respect to jet multiplicity and jet-parton matching. Since only the qualitative behavior is of interest here, an event selection following the Run I analysis is applied:

- 1 tight electron with $p_T > 20$ GeV and $|\eta_{det}| < 2.0$,
- Missing $E_T > 20$ GeV,
- Jets with $p_T > 15$ GeV and $|\eta_{det}| < 2.5$.

In order to describe the quality of events (with respect to the jet study), two variables are defined:

$$\epsilon(n) = \frac{\text{number of events with } n \text{ jets}}{\text{number of events}}, \quad (10.1)$$

$$p(m, n) = \frac{\text{number of events with } m \text{ matched jets}}{\text{number of events with } n \text{ jets}}, \quad (10.2)$$

where $\epsilon(n)$ is referred to as efficiency and $p(m, n)$ as purity. A criterion of $\Delta R < 0.3$ is used to match jets to partons. The jet multiplicity distribution in the $t\bar{t}$ sample is shown on the left hand side of Figure (10.1). Only a fraction of about 35% of the events do have 4 jets as required by the Matrix Element Method, i.e. $\epsilon(4) = 0.35$. The purity in the 4th jet multiplicity bin of the sample can be derived from the right hand side of Figure (10.1). Here, the distribution of matched jets in that particular bin is shown. The purity $p(4, 4) = 0.55$. These numbers are used as references in the following study.

10.1. Jet Merging Algorithm

In order to increase the efficiency and purity of the sample, additional tracking information is used. The main idea is the merging of calorimeter jets and track jets. This approach is motivated by initial and final state radiation which is emitted softly and collinearly to the jet direction. Therefore track jets close to the calorimeter jet under study are added to the latter. Also, by repeatedly applying this algorithm until a total of 4 jets is obtained, the number of events in the 4th jet multiplicity bin will increase and with it the efficiency.

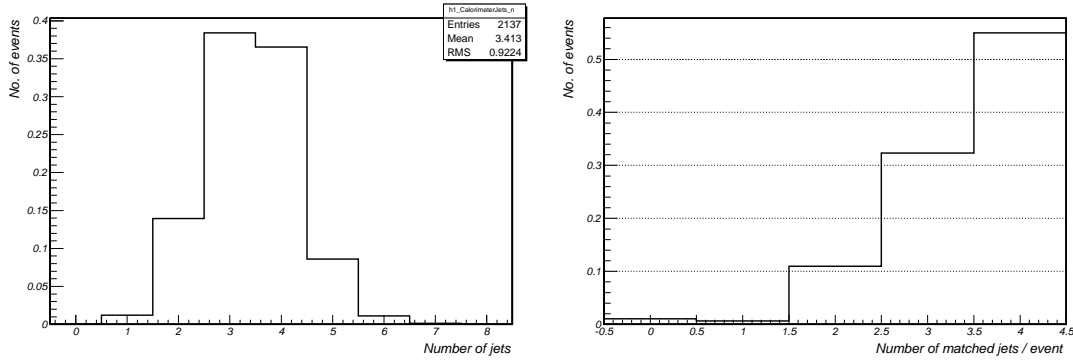


Figure 10.1.: **Left:** Jet multiplicity in the p13 $t\bar{t}$ Monte Carlo sample. **Right:** Distribution of matched jets in the 4th jet multiplicity bin.

Before the algorithm is applied, two steps have to be taken. First, track jets are removed that originate from an electron. These jets are found within a certain region around the electron and therefore cut out with the following criteria:

$$\begin{aligned}\Delta R(e, \text{jet}) &< 0.3, \\ \Delta p_T/p_T &< 0.5.\end{aligned}$$

As a second step, track jets are removed that overlap with calorimeter jets in order to avoid “double counting” of energy. This is accomplished by demanding a certain distance between both jets:

$$\Delta R(\text{cal. jet, trk. jet}) < 0.3. \quad (10.3)$$

The Merging Algorithm

The algorithm used for the merging of calorimeter and track jets works as follows: first, the distance in the $\eta - \phi$ plane is calculated between all (calorimeter and track) jets. Based on these numbers, the jet pair with the smallest distance is merged by adding up the 4-momenta. The distances are recomputed and the whole merging procedure repeated until the number of jets equals 4. It should be mentioned that two calorimeter jets are never merged because this is already done during the reconstruction process. Only merging between different types of jets or between track jets is allowed here. Additionally, the ΔR criterion for jet-parton matching is increased by 0.1 per track jet merged. This accounts for the fact that FSR broadens the jet.

Figure (10.2) shows event displays in the $\eta - \phi$ -plane as an example for the merging algorithm. The markers indicate the quarks and the leptons (for each flavor separately), the circles represent the calorimeter (red/grey) and track (black) jets. The event shown in the top display of Figure (10.2) would not pass the event selection introduced for the Matrix Element Method since only 3 calorimeter jets are present before the merging process. After the algorithm is applied, a total of 4 jets is found. In this case all jets are matched to partons as can be seen in the bottom display.

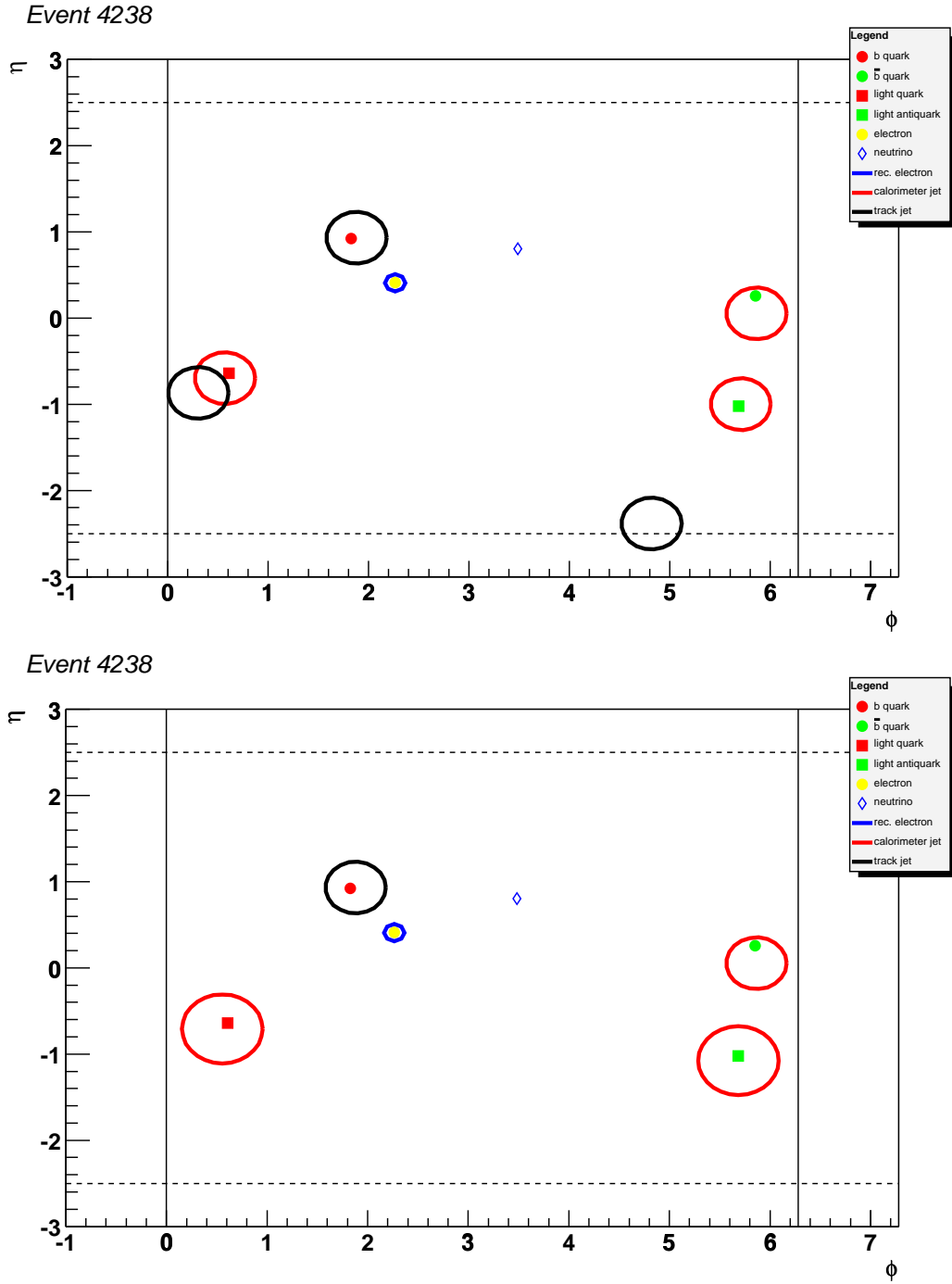


Figure 10.2.: **Top:** Event display of an event with only 3 calorimeter jets (black circles). The event would not have passed the selection criteria for the mass analysis. **Bottom:** The same event as in the top figure, but after the merging algorithm is applied. In total 4 jets remain which are now matched to partons (full circles and squares). The radius of the black circles corresponds to the matching criterion.

Efficiency and Purity

The jet merging algorithm is applied to the entire sample. Table (10.1) summarizes the efficiency and purity obtained and compares the sample with and without merging algorithm applied. In the latter case only events with 4 calorimeter jets are taken into account, so no values for the 3-calorimeter-jet efficiency and purity are quoted.

Two conclusions can be drawn from the comparison: first, the efficiency of events with 4 calorimeter jets increases by (absolute) 2%, from 35% to 37%, when applying the merging algorithm. Second, the purity of 4-jet events, i.e. the number of events with 4 calorimeter jets with all jets matched to partons, increases by (absolute) 2%, from 55% to 57%. Even though the effect is not very large, the merging algorithm can improve the selection in such a way that the number of events is increased together with the quality of the jets.

The number of selected events can additionally be increased if events with 1 track jet and 3 calorimeter jets are included. From Table (10.1) it can be seen that (absolute) 33% of the events in the sample show this configuration. It should be mentioned that the purity of this class of events is only 25% compared to the 57% purity for events with 4 calorimeter jets. In total, the number of selected events is almost doubled.

	$\epsilon(3)$	$\epsilon(4)$	$p(4, 3)$	$p(4, 4)$
without merging	-	0.35	-	0.55
with merging	0.33	0.37	0.25	0.57

Table 10.1.: Efficiency and purity before and after the merging algorithm is applied to the sample. Before the algorithm is applied only events with 4 calorimeter jets are selected, so no values for $\epsilon(3)$ and $p(4, 3)$ are quoted. Both, the number and the quality of events (in terms of jet parton assignment) increase with the jet merging algorithm for events with 4 calorimeter jets. If events with 1 track jet and 3 calorimeter jets are allowed, the number of selected events almost doubles, although the purity of this class of events is only 25%.

As a next step the resolution gained with the additional class of events is studied.

10.2. Resolution

Since the energy resolution of jets is important for the measurement of the top quark mass, the resolution is studied after the jet merging algorithm is applied. Figure (10.3) shows the energy resolution for calorimeter and track jets separately for light and b jets. For the calorimeter jets the distributions are gaussian with non-gaussian tails. This is expected from the experience with the transfer functions. In case of track jets, large tails on the negative side are observed. These can be explained by the fact that only charged particles are observed in the tracker, and therefore the jet energy is underestimated.

An energy correction factor ϵ can be applied to the track jets. In order to derive this factor from Monte Carlo, track jets are matched to calorimeter jets (these track jets were previously removed) and the ratio of energies is calculated, i.e. $\epsilon = E_{cal}/E_{trk}$. Figure (10.4) shows the distribution of ratios. As can be seen it has a mean of 2.6 and large non-gaussian tail to larger fractions. Since on average about 30% neutral particles are contained in a jet, a factor of $\epsilon \approx 1.5$ is expected which corresponds to the maximum of the distribution.

As a next step, correlations between the correction factor and p_T , η , ϕ and the track jet energy are studied. The latter one is shown in Figure (10.5). On the left the 2-dimensional

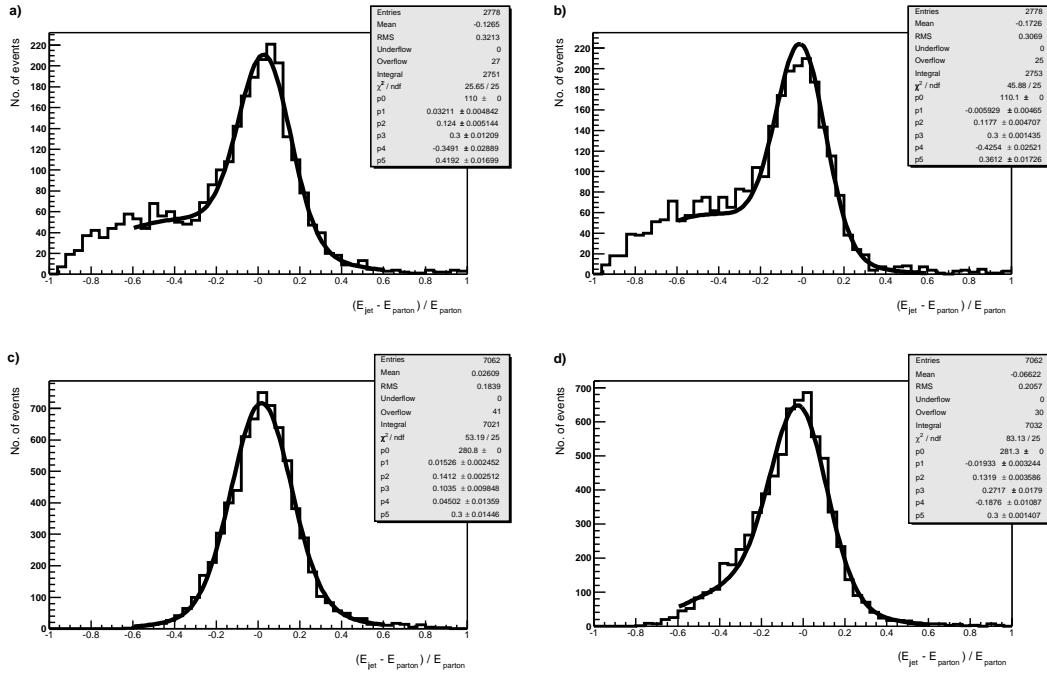


Figure 10.3.: Energy resolution for track (**top**) and calorimeter jets (**bottom**). Both are plotted separately for light (**left**) and b jets (**right**). Large tails on the negative side for track jets are due to neutral particles within the jet.

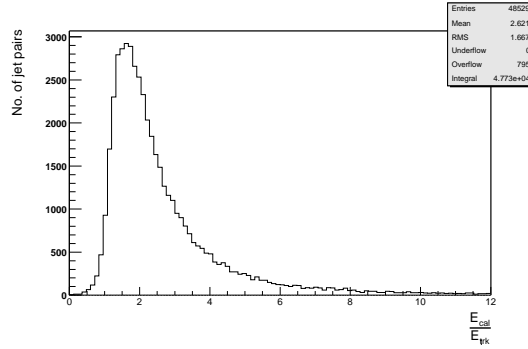


Figure 10.4.: Distribution of energy fractions of calorimeter and track jets. The mean of the distribution is 2.6, the maximum is found at a fraction of ~ 1.5 , which is expected from the approximately 30% neutral particles in a jet.

correlation is plotted, on the right the means (and corresponding errors) for slices of the track jet energies is shown and fitted with a function of the form:

$$\epsilon(E_{\text{trk}}) = p_0 \cdot e^{p_1 \cdot E_{\text{trk}}} + p_2 \cdot E_{\text{trk}} + p_3. \quad (10.4)$$

Additionally, a further identification of final state radiation is studied. Figure (10.6) shows the distribution of distances between merged calorimeter and track jets weighted by the energy of track jets. The cone size for calorimeter jets in the $D\phi$ reconstruction is $\Delta R = 0.5$, and as can be seen in the plot, a local maximum for values around 0.7 is found. As can be concluded from

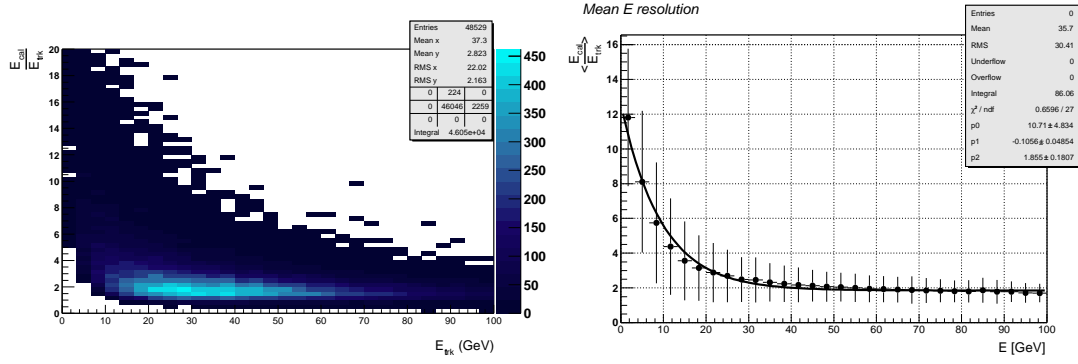


Figure 10.5.: Left: 2-dimensional histogram of ϵ vs. the energy of the track jets. **Right:** The means of slices from the 2-dimensional plot as a function of the track jet energy. The errors correspond to the errors on the means. A functional form given by Equation (10.4) is fitted.

the 2-dimensional histogram on the right hand side of Figure (10.6), an additional cut can be used to further identify final state radiation:

$$\begin{aligned} \Delta R &< 1.0, \\ E_{trk} &< 15 \text{ GeV}. \end{aligned} \quad (10.5)$$

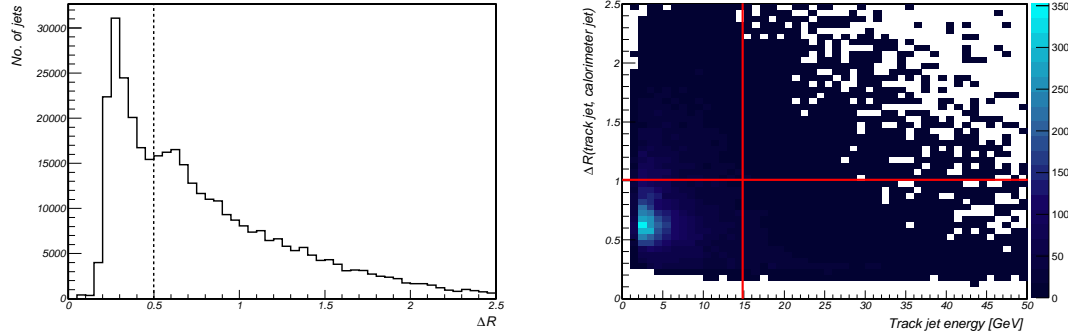


Figure 10.6.: Left: Distance between merged jets weighted by the energy of the track jet. **Right:** ΔR vs. the energy of the merged track jet.

In the following, several scenarios in terms of energy correction are studied with respect to the mass resolution. These are:

1. No energy correction ($\epsilon = 1$).
2. The mean value of the energy ratio distribution ($\epsilon = 2.6$).
3. The track jet energy dependent ϵ parameterized by Equation (10.4).
4. The asymptotic value of the fit ($\epsilon = 1.85$).
5. The energy dependence including a cut for final state radiation.

6. The old event selection, i.e. no merging algorithm applied. Only events with 4 calorimeter jets are selected.

An example for the mass resolution is found in the Figures (10.7) and (10.8). The first shows the mass resolution if no energy correction is applied to the track jets. Non-gaussian tails are observed here. This is expected from the energy resolution plotted in Figure (10.3). The latter figure shows the mass resolution after the cut on final state radiation.

Table (10.2) summarizes the results for the different approaches. The numbers quoted are the means and RMS of the distributions and the width of the central gaussian applying a double-gaussian fit to the distributions. As in case of the transfer functions, this is done in order to account for the non-gaussian tails.

Several conclusions can be drawn from the table: for events with 1 track jet and 3 calorimeter jets, the mass resolution for the hadronic W and top improve with the application of an energy correction factor (from a sigma of 0.24 to values between 0.15 to 0.17 in case of the hadronic W mass, and from 0.18 to values between 0.14 to 0.16 for the hadronic top mass). Also, the means of the distributions converge towards 0 GeV/c² as is expected since the energy correction factor is applied to account for the neutral particles (and the underestimation of energy).

For events with 4 calorimeter jets the effects on the distributions are rather small. The widths of the central gaussians only vary by (absolute) 1%, the means only by (absolute) 5%. This is due to the fact that the track jets only indirectly effect the distributions since they are merged into the calorimeter jets.

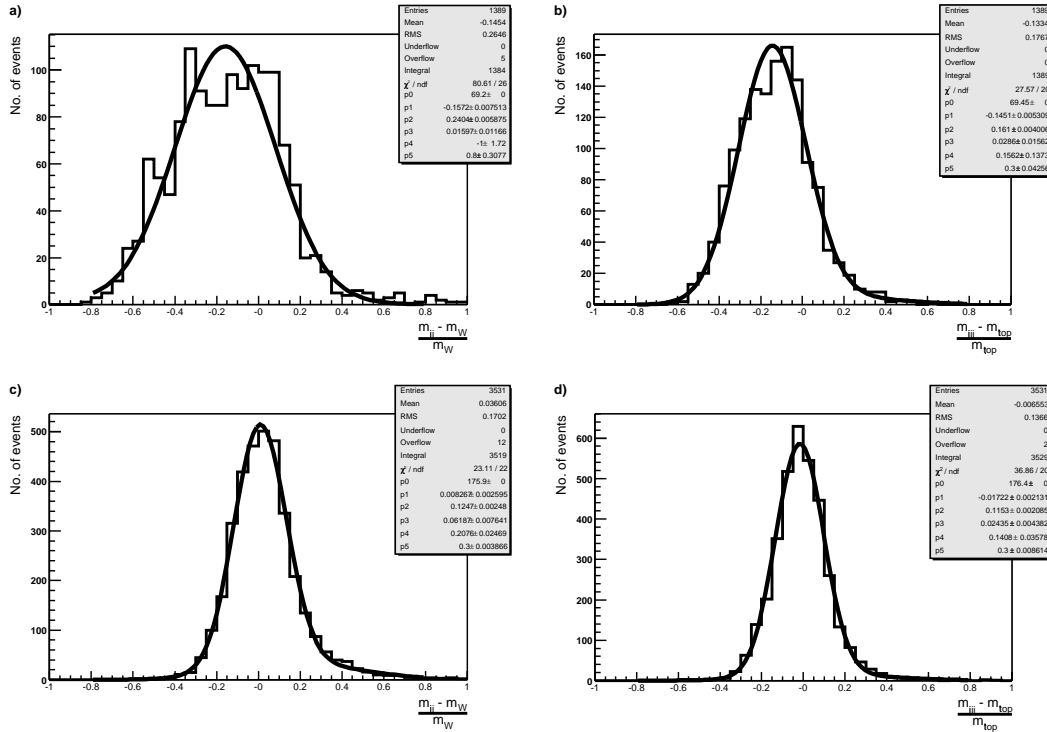


Figure 10.7.: Resolution of the hadronic W (left) and top (right) masses using the correct jet-parton assignment without applying energy corrections to the track jets (scenario 1). This is done for events with 3 (top) and 4 (bottom) calorimeter jets. The distributions have non-gaussian tails and are fitted with double-gaussian functions.

Cal. jets	Track jets	Resolution	$\epsilon = 1$	$\epsilon = 2.6$	$\epsilon = \epsilon(\mathbf{E}_{\text{trk}})$
3	1	$mean_W$	-0.15	0.09	0.12
3	1	RMS_W	0.26	0.25	0.25
3	1	σ_W	0.24	0.17	0.17
3	1	$mean_{top}$	-0.13	0.06	0.07
3	1	RMS_{top}	0.16	0.21	0.19
3	1	σ_{top}	0.18	0.15	0.14
4	0	$mean_W$	0.04	0.07	0.09
4	0	RMS_W	0.17	0.20	0.22
4	0	$sigma_W$	0.12	0.13	0.12
4	0	$mean_{top}$	-0.01	0.03	0.06
4	0	RMS_{top}	0.14	0.17	0.19
4	0	σ_{top}	0.12	0.12	0.12
Cal. jets	Track jets	Resolution	$\epsilon = 1.85$	$\epsilon = \epsilon_{\text{FSR}}(\mathbf{E}_{\text{trk}})$	no merging
3	1	$mean_W$	-0.01	0.05	-
3	1	RMS_W	0.24	0.22	-
3	1	σ_W	0.15	0.16	-
3	1	$mean_{top}$	-0.02	0.00	-
3	1	RMS_{top}	0.19	0.16	-
3	1	σ_{top}	0.16	0.14	-
4	0	$mean_W$	0.06	-0.01	-0.02
4	0	RMS_W	0.19	0.13	0.13
4	0	$sigma_W$	0.12	0.12	0.12
4	0	$mean_{top}$	0.02	-0.05	-0.05
4	0	RMS_{top}	0.16	0.11	0.11
4	0	σ_{top}	0.12	0.11	0.11

Table 10.2.: Resolution parameters for W and top mass obtained from the study described in the text. Due to the applied energy correction the resolution (in terms of width and mean of the distributions) improves for events with 1 track jet and 3 calorimeter jets. For events with 4 calorimeter jets the resolution is only slightly effected.

10.3. Conclusion

From the studies presented here it can be concluded that the introduction of a merging algorithm for track jets does improve the efficiency, i.e. the number of selected events is almost doubled (from 35% to 70% of the number of events in the sample) if events with 1 track jet and 3 calorimeter jets are taken into account. Nevertheless, the purity of the additional sample, $p(4, ; 3) = 0.25$, is less than that of the sample used in the previous analysis $p(4, ; 4) = 0.55$. The mass resolution in the 4 calorimeter jet case does not change and is 12% for the hadronic W mass and 11% for the hadronic top mass. In the sample with 3 calorimeter and one track jet the resolution is derived correcting for the neutral particles not observed by the detector, yielding 16% for the hadronic W mass and 14% for the hadronic top mass.

For the mass analysis with the Matrix Element Method this study could be used for two purposes:

First, the additional sample might behave differently in terms of systematic variations. This is due to the fact that calorimeter and tracker measure quantities independently. By using tracking

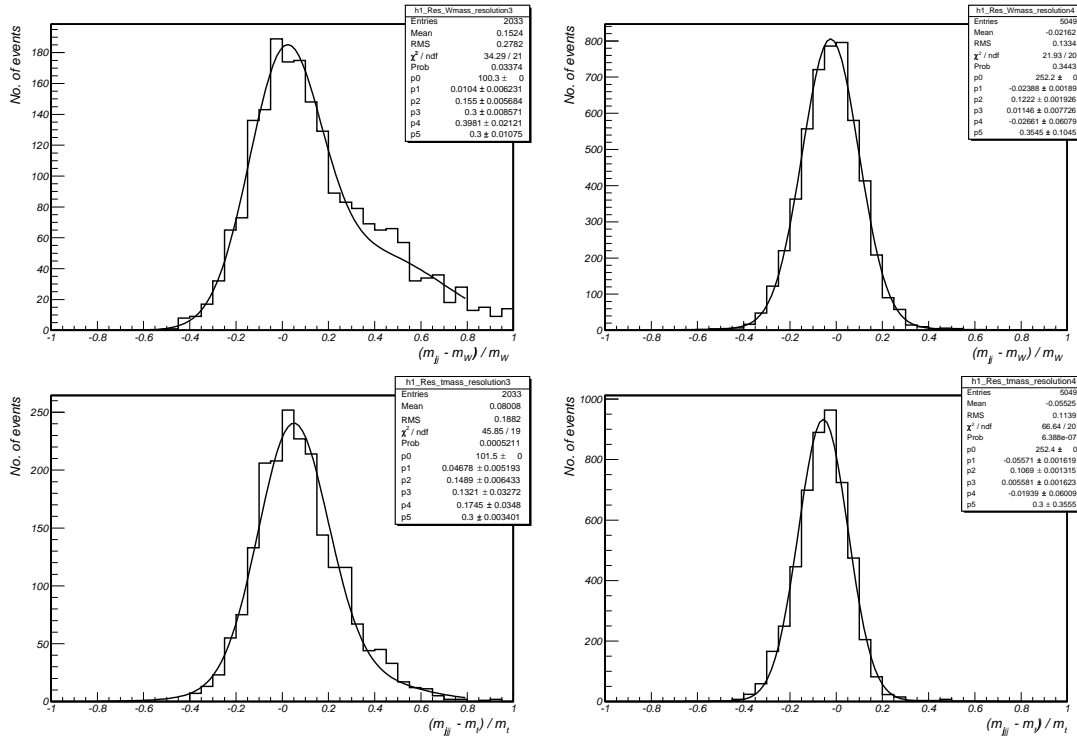


Figure 10.8.: Same as in Figure (10.7) but after applying energy dependent corrections to the track jets and further cutting for final state radiation (scenario 5).

information, the influence on the jet energy scale might be reduced because the energy is not only measured in the calorimeter. The main source of systematic uncertainty might therefore be decreased with this approach. This has to be studied in more detail. Second, the available statistics can be increased. Because the dominating uncertainty does not come from limited statistics, this effect is rather small. The fact that the purity of the additional events is lower has to be studied in more details since the method is sensitive to ISR/FSR mismatched jets. The worse resolution, however, can be described by transfer functions for track jets. These should be derived in analogy to the ones described in Chapter 6.

A. Phase Space Calculations

As described in Section (5.2.2) the transformation of integration variables implies a Jacobian determinant. This transformation factor is derived in the following.

The phase space in Equation (4.2) is a function of the 3-momenta of the final state particles. Energy- and momentum-conservation together with the measurement of jets and leptons reduce the number of integrations to be performed. The set of variables for this integration are the jet momenta (ρ_1, \dots, ρ_4) and the longitudinal momentum of the neutrino (p_ν^z). In terms of numerical integration, an alternative choice of variables is more appropriate: the invariant mass of the hadronic and leptonic top quark ($m_{12b}^2, m_{l\nu b}^2$), the mass of the hadronic W boson (m_{12}^2), the absolute value of the up-type light jets (ρ_1) and the longitudinal momentum of the neutrino (p_ν^z). Both sets are linked via the following equations, where the indices 1 and 2 refer to the light jets, 3 and 4 to the hadronic and leptonic jets, respectively:

$$\rho_1 = \sqrt{E_1^2 - m_1^2} \simeq E_1 \quad (\text{A.1})$$

$$\begin{aligned} m_{12}^2 &= (p_1 + p_2)^2 \\ &= m_1^2 + m_2^2 + 2 \cdot E_1 E_2 - 2 \cdot |\vec{p}_1| |\vec{p}_2| \cos \theta_{12} \\ &\simeq 2 \cdot E_1 E_2 \cdot (1 - \cos \theta_{12}) \end{aligned} \quad (\text{A.2})$$

$$\begin{aligned} m_{123}^2 &= (p_1 + p_2 + p_3)^2 \\ &= m_1^2 + m_2^2 + m_3^2 \\ &\quad + 2 \cdot E_1 E_2 - 2 \cdot |\vec{p}_1| |\vec{p}_2| \cos \theta_{12} \\ &\quad + 2 \cdot E_2 E_3 - 2 \cdot |\vec{p}_2| |\vec{p}_3| \cos \theta_{23} \\ &\quad + 2 \cdot E_1 E_3 - 2 \cdot |\vec{p}_1| |\vec{p}_3| \cos \theta_{13} \\ &\simeq 2 \cdot E_1 E_2 \cdot (1 - \cos \theta_{12}) \\ &\quad + 2 \cdot E_2 E_3 \cdot (1 - \frac{\rho_3}{E_3} \cos \theta_{23}) \\ &\quad + 2 \cdot E_1 E_3 \cdot (1 - \frac{\rho_3}{E_3} \cos \theta_{13}) + m_3^2 \end{aligned} \quad (\text{A.3})$$

$$\begin{aligned} m_{l\nu 4}^2 &= (p_\nu + p_l + p_4)^2 \\ &\simeq 2 \cdot E_l E_\nu (1 - \cos \theta_{l\nu}) \\ &\quad + 2 \cdot E_\nu E_4 (1 - \frac{\rho_4}{E_4} \cos \theta_{\nu 4}) \\ &\quad + 2 \cdot E_l E_4 (1 - \frac{\rho_4}{E_4} \cos \theta_{l 4}) + m_3^2 \end{aligned} \quad (\text{A.4})$$

where the light partons are assumed to be massless.

In order to calculate the Jacobian, all derivations of the new set with respect to the old set have to be calculated. Since most of these terms vanish, the terms not equal to zero are stated explicitly:

$$\left(\frac{\partial \rho_1}{\partial \rho_1}\right) = 1, \quad (\text{A.5})$$

$$\left(\frac{\partial m_{12}^2}{\partial \rho_2}\right) = 2 \cdot E_1(1 - \cos \theta_{12}), \quad (\text{A.6})$$

$$\left(\frac{\partial m_{123}^2}{\partial \rho_3}\right) = 2 \cdot (E_2 \frac{\rho_3}{E_3} - E_2 \cos \theta_{23} + E_1 \frac{\rho_3}{E_3} - E_1 \cos \theta_{13}), \quad (\text{A.7})$$

$$\left(\frac{\partial m_{4l\nu}^2}{\partial \rho_4}\right) = 2 \cdot (E_\nu \frac{\rho_3}{E_3} - E_\nu \cos \theta_{\nu 3} + E_l \frac{\rho_3}{E_3} - E_l \cos \theta_{l3}). \quad (\text{A.8})$$

The Jacobian for the transformation is simply the product of reciprocals of the derivatives stated above in Equations (A.5) to (A.8):

$$J = \frac{1}{1} \cdot \frac{1}{2 \cdot E_1(1 - \cos \theta_{12})} \cdot \frac{1}{2 \cdot (E_2 \frac{\rho_3}{E_3} - E_2 \cos \theta_{23} + E_1 \frac{\rho_3}{E_3} - E_1 \cos \theta_{13})} \cdot \frac{1}{2 \cdot (E_\nu \frac{\rho_3}{E_3} - E_\nu \cos \theta_{\nu 3} + E_l \frac{\rho_3}{E_3} - E_l \cos \theta_{l3})}. \quad (\text{A.9})$$

B. Integration Techniques

The following section describes the numerical techniques of integration for the calculation of signal and background probabilities as used in Chapter 5. Both are a compromise between speed and accuracy due to the CPU-time limitation.

Integration Technique in Case of Signal Probability

In case of the signal probability, the integral in Equation (5.8) over the $\rho_1 - p_\nu^z$ -plane is performed numerically. Because the evaluation of the kinematic equations and the matrix element are rather slow, a fast integration technique had to be implemented. Several routines from CERNLIB [31] (adaptive and gaussian multidimensional integrations) are tested but found to be insufficient for the given purpose. Instead, a simple 2-dimensional Simpson algorithm is used. In principle, the adaptive and gaussian methods are faster given the same accuracy, but as is explained in the following, only certain regions of large probability density are taken into account. For the CERNLIB routines, this was not possible to implement. The main idea is to divide the $\rho_1 - p_\nu^z$ -plane into squares of appropriate size and add all contributions. Each “volume element” is calculated by interpolating the borders of the square by a straight line and integrating analytically over the square. This can be seen in Figure (B.2). After the 4 border points are calculated the function over which the integration is performed is parameterized the following way:

$$f(x, y) = a \cdot x + b \cdot y + c \cdot xy + d. \quad (\text{B.1})$$

The parameters a to d are derived from a system of linear equations fed with the values at the 4 border points. The volume is now the integral over that function:

$$\begin{aligned} V = \int_0^1 dx \int_0^1 dy &= \frac{1}{2}a \cdot x^2 y \frac{1}{2}b \cdot xy^2 \frac{1}{4}c \cdot x^2 y^2 d \cdot xy \Big|_{(0,0)}^{(1,1)} \\ &= \frac{1}{2}a + \frac{1}{2}b + \frac{1}{4}c + d. \end{aligned} \quad (\text{B.2})$$

First, the limits of integration are estimated. This is done by estimating the minimum and maximum value for each variable. Figure (B.1) shows the distributions of ρ_1 and p_ν^z for a given Monte Carlo sample. From these plots the limits are defined to be

$$\begin{aligned} \rho_1 &\in (0. \text{ GeV}, 350. \text{ GeV}), \\ p_\nu^z &\in (-300. \text{ GeV}, 300. \text{ GeV}). \end{aligned}$$

In order to save additional CPU time the area of integration is further confined to regions of larger probabilities. The algorithm used for that purpose works as follows: for all 24 possible

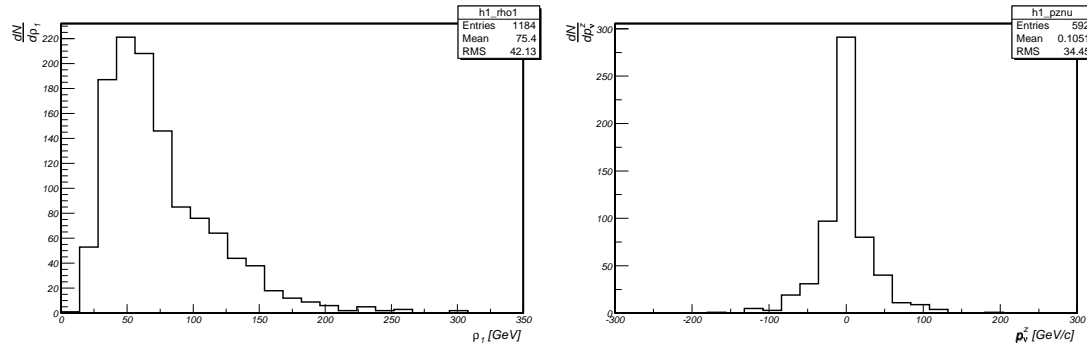


Figure B.1.: **Left:** Distribution of the absolute value of the momentum for light jets. **Right:** Distribution of the longitudinal momentum of the neutrino. Both distributions are made from $t\bar{t}$ samples at a top quark polemass of 175 GeV/ c^2 .

jet parton combinations, the $\rho_1 - p_\nu^z$ -plane is scanned in 5 GeV steps and the global maximum M_i ($i = 1, \dots, 24$) is estimated. From the set of maxima the largest value is referred to as global maximum $M_{global} = \max \{M_i\}$.

First, jet parton combinations with lower probability are neglected in the further calculation of the integral. This is done by demanding the global maximum of the particular combination j to satisfy the following relation:

$$M_j > \epsilon \cdot M_{planes}, \quad (\text{B.3})$$

where ϵ is a small parameter between 0 and 1, which sets the accuracy.

Second, for the remaining jet parton combinations a finer grid (1 GeV) is used to calculate the integrand at each point. This is not done for the entire $\rho_1 - p_\nu^z$ -plane, but only for those regions in which the probability density from the rough 5 GeV scan is larger than a limit defined by the following equation:

$$p(\rho_1, p_\nu^z) > \epsilon \cdot M_i \quad (\text{B.4})$$

where again M_i is the global maximum of combination i and ϵ is the same parameter as in equation (B.3). Using this constraint, only regions of larger probability density are taken into account.

After the grid is calculated, squares with a size of 1×1 GeV² are built. For each square the 4 border points are calculated and the borders are interpolated by a straight line. With this approximation the integral over the square is calculated analytically. All volume elements are then added up. Figure (B.2) visualizes the principle. Figure (B.3) shows two examples of the integrand as a function of ρ_1 and p_ν^z for a single event. On the left hand side only the correct jet-parton-combination is taken into account, whereas on the right hand side all possible combinations passing the criterion in Equation (B.3) are superimposed. The parabolic shape follows from the ambiguity of the longitudinal neutrino momentum.

The technique described is used to find a compromise between accuracy and CPU time. In order to verify that the accuracy is sufficient, the parameter ϵ in Equation (B.3) is varied and the integral calculated. Figure (B.4) shows the accuracy as a function of ϵ . For the analysis $\epsilon = 10^{-5}$ is chosen.

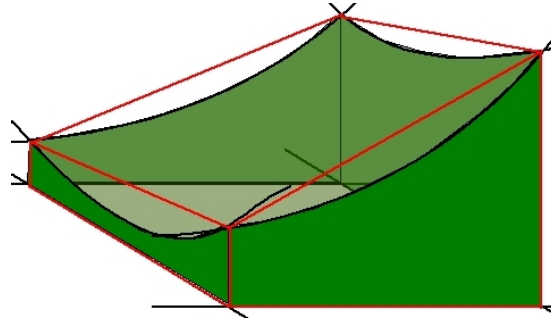


Figure B.2.: For each unity square in $\rho_1 - p_\nu^z$ the borders are interpolated with straight lines. The integral over that region is calculated analytically.

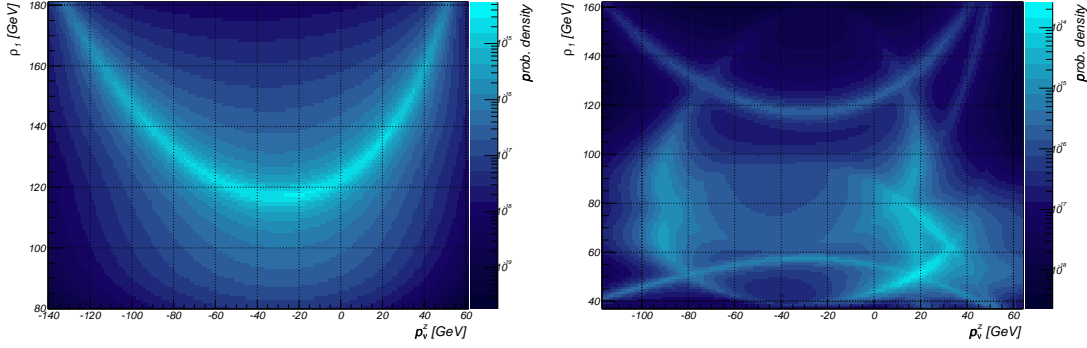


Figure B.3.: Integrand for a single event as function of ρ_1 and p_ν^z . For the integration, only regions are taken into account that have a large probability density. **Left:** Only the correct jet parton assignment is taken into account. The parabola due to the ambiguity of the longitudinal neutrino momentum can be seen. **Right:** All combinations that satisfy Equation (B.3) are added up.

Integration Technique in Case of Background Probability

In case of the background probability the integration is also performed numerically but following a different ansatz. Because the variables of integration are not transformed, they are chosen to be the jet energies¹ and the longitudinal momentum of the neutrino. The technique used for integration is a simple Monte Carlo approach.

From Equation (4.9) it follows that the integral has the following form:

$$I(x) = \int dy f(y) W(x, y), \quad (\text{B.5})$$

where $f(y)$ contains the matrix element, flux factor and parton distribution functions. $W(x, y)$ are the transfer functions for the energies of the jets.

For each parton energy the transfer functions are interpreted as probability densities, so the integral $I(x)$ is the expectation value for $f(y)$. By sampling over the 4-dimensional space of jet energies, the expectation value can be approximated by the average value:

¹Since only light flavored partons are assumed, $\rho_i = |\vec{p}_i| = E_i$.

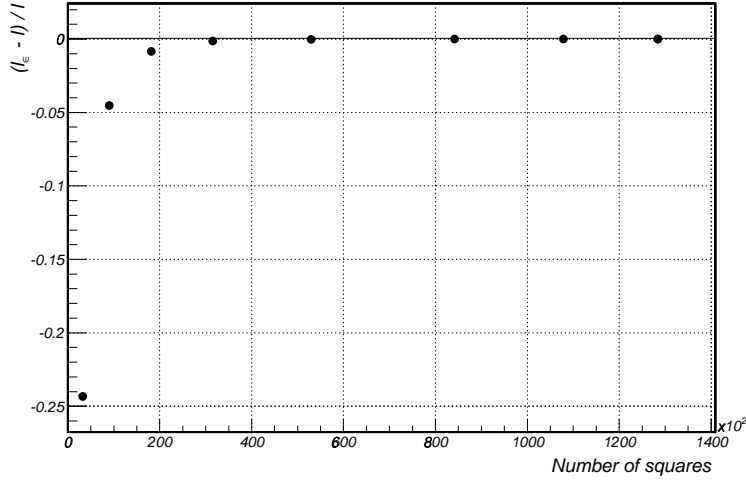


Figure B.4.: Accuracy of the numerical integration for the signal probability as a function of ϵ . For the analysis $\epsilon = 10^{-5}$ is chosen.

$$I(x) = \int dy f(y) W(x, y) \rightarrow \frac{1}{N} \sum_{i=1}^N f(y). \quad (\text{B.6})$$

The N points are selected using random numbers distributed according to the transfer functions. Of course each jet-parton assignment makes it necessary to use different sets of transfer functions. For each sampled point the integration over p_ν^z is performed using a gaussian method (CERNLIB). The sampling is repeated until a certain accuracy is obtained. It is found that for an accuracy of about 10% it is appropriate to use 100 sampling points. Figure (B.5) shows two examples for the accuracy of the integration as a function of the number of evaluations. This procedure is repeated for all 24 possible jet combinations and the average value is used for the probability.

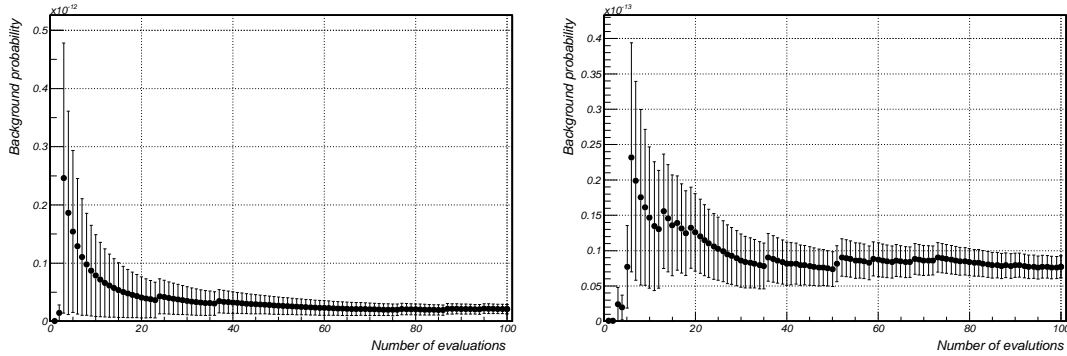


Figure B.5.: Two examples for the accuracy of the integration technique for the background probability. In this case two $W + 4 \text{ jets}$ events are shown. On the x-axis the number of points is plotted. The sampling is repeated until a certain accuracy is obtained.

C. Kinematic Solver

The matrix element and phase space factors are functions of the 4-momenta of the final-state particles. Since the variables of integration are transformed into a new set of variables and because the neutrino p_T is not measured but obtained from momentum balance, the kinematic Equations (A.1) to (A.3) have to be solved.

Before calculating the energies of the partons additional corrections are applied to the measured jet energies. The parton level corrections described in Chapter 6 depend on the flavor, the energy and the η region of the jet and are applied first. Then, the η dependent jet energy scale corrections are multiplied to the measured jet energy. For each jet parton combination these factors are recalculated and applied under the assumptions of a certain parton flavor of the jet.

Next, the hadronic branch of the $t\bar{t}$ -system is calculated. This is done by transforming Equations (A.1) - (A.3) gradually back to the parton energies, starting with ρ_1 . The solutions of the equations are non-ambiguous.

However, for the leptonic branch a system of equations has to be solved. This is due to the fact that the transverse momentum of the neutrino depends on the parton energies. It follows that, once the hadronic branch is fixed, the momenta of the b quark from the leptonic branch and the neutrino are coupled. The following set of equations reflects this fact, assuming that the transverse momentum of the $t\bar{t}$ -system vanishes:

$$\begin{aligned} p_\nu^x &= p_{t_{had}}^x - a \cdot n_{b_{lep}}^x - p_l^x, \\ p_\nu^y &= p_{t_{had}}^y - a \cdot n_{b_{lep}}^y - p_l^y, \end{aligned} \tag{C.1}$$

where $a = |\vec{p}_{b_{lep}}|$ and $\vec{n}_{b_{lep}}$ is the unity vector in the direction of the leptonic b quark. $\vec{p}_{t_{had}}$ refers to the hadronic top quark which was calculated previously. With Equations (C.1) as a constraint Equation (A.4) contains only one unknown, i.e. a . In order to solve for a a function F is defined as follows:

$$F(a) = -m_{A4\nu}^2 + (p_4(a) + p_l + p_{nu}(a))^2. \tag{C.2}$$

The roots of $F(a)$ solve Equation (A.4). They are calculated numerically using Newton's method. Figure (C.1) shows the number of solutions for a sample of events and the value of the obtained solutions vs. the true value of a .

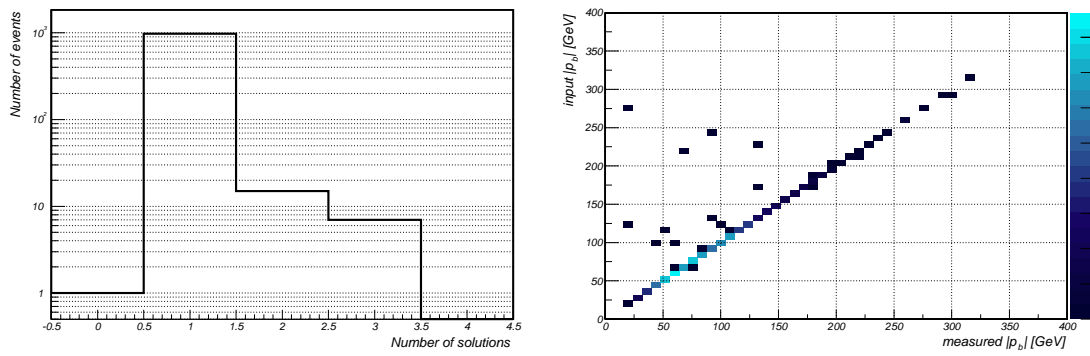


Figure C.1.: **Left:** Number of solutions for a whole sample of events. As can be seen from there, mostly one solution is found. **Right:** Value of a obtained with the method explained in the text vs. the true value of a . In most of the cases the correct solution is found.

D. Data and Monte Carlo Samples

Sample	Reco. Version	top_analyze Version	Number of Events	Comments
<i>ME-Method</i>				
$t\bar{t} \rightarrow l + jets$	p14	Nefertiti	600	mass 150 GeV/c ² , no MPI
$t\bar{t} \rightarrow l + jets$	p14	Nefertiti	300	mass 160 GeV/c ² , no MPI
$t\bar{t} \rightarrow l + jets$	p14	Nefertiti	300	mass 170 GeV/c ² , no MPI
$t\bar{t} \rightarrow l + jets$	p14	Nefertiti	1000	mass 175 GeV/c ² , no MPI
$t\bar{t} \rightarrow l + jets$	p14	Nefertiti	300	mass 175 GeV/c ² , MPI
$t\bar{t} \rightarrow l + jets$	p14	Nefertiti	300	mass 180 GeV/c ² , no MPI
$t\bar{t} \rightarrow l + jets$	p14	Nefertiti	300	mass 190 GeV/c ² , no MPI
$t\bar{t} \rightarrow l + jets$	p14	Nefertiti	600	mass 200 GeV/c ² , no MPI
$W + 4 jets$	p14	Nefertiti	1000	no MPI
$W + 4 jets$	p14	Nefertiti	1000	MPI
$W + 4 jets$	p14	Nefertiti	1000	MPI, low parton level cuts
<i>Data Sets</i>				
Moriond Data Set	p14	Nefertiti		see [37] for details
<i>Jet Studies</i>				
$t\bar{t} \rightarrow e + jets$	p13	v00-02-24	5000	mass 175 GeV/c ²

Table D.1.: Monte Carlo and data samples used in this analysis.

E. Data to Monte Carlo Comparison

In the following the primary measured kinematic quantities of the data sample introduced are compared to Monte Carlo and QCD events as used in the ensemble tests. As can be seen the selected events are reasonably well described with the previously derived mixture of $t\bar{t}$ and background events (see Chapter (7.3)). Also, no accumulation of events in any tail or other suspicious parts of distributions are observed. Therefore, the indication for the presence of a significant number of $t\bar{t}$ events is given. The plots are taken from [26], where a more thorough data to Monte Carlo comparison is given.

It should be mentioned that the two events that cause a jump in the likelihood curve tend to have high values in some of the distributions below. Table (7.7) summarizes the kinematic quantities of those events.

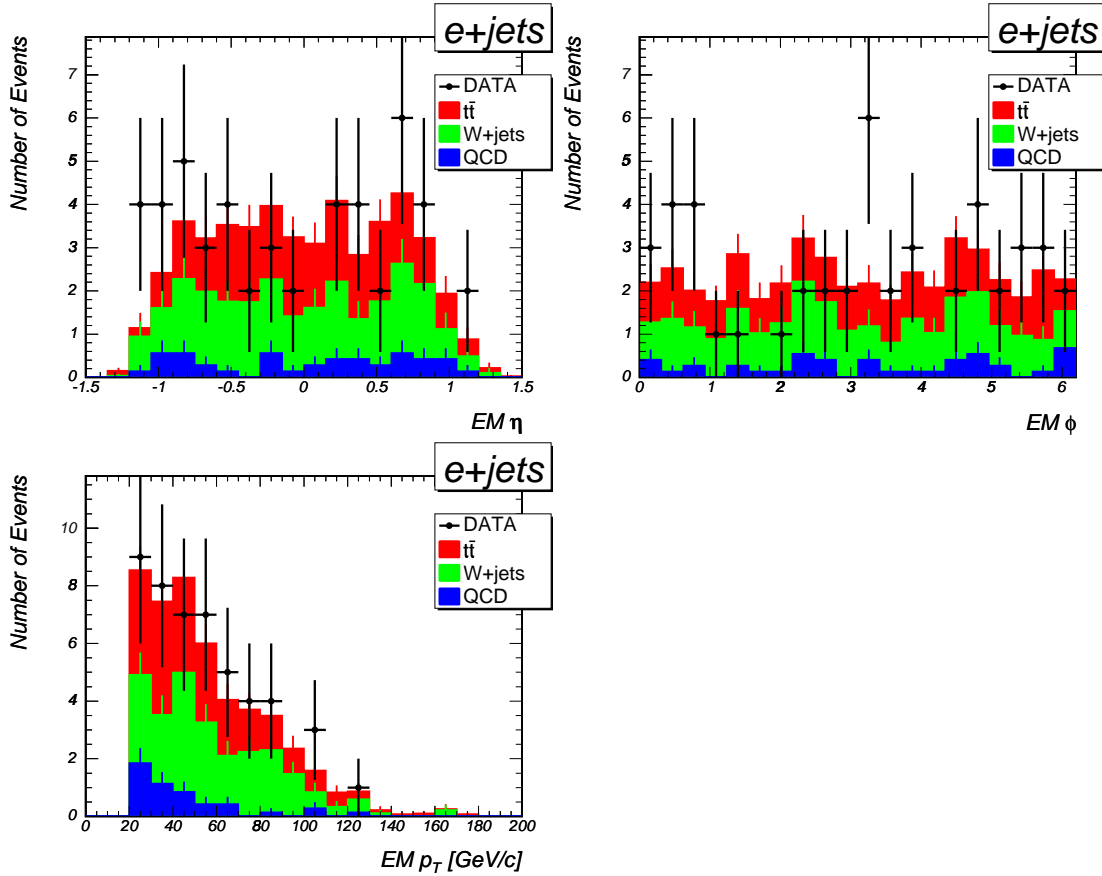


Figure E.1.: Data to Monte Carlo comparison for signal plus background of the selected event sample in the primary measured kinematic quantities in the $e + jets$ channel.

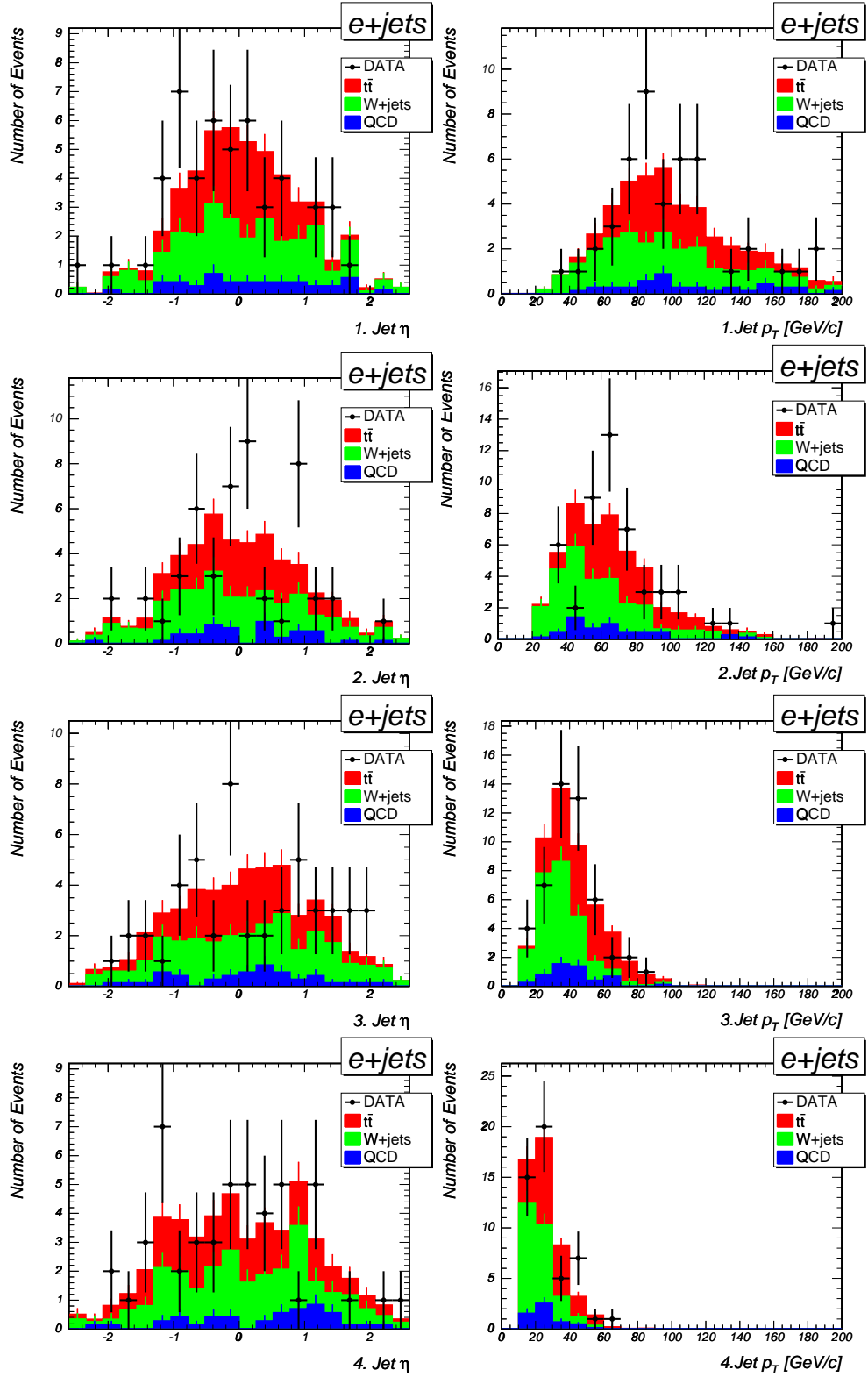


Figure E.2.: Data to Monte Carlo comparison for signal plus background of the selected event sample in the $e + jets$ channel.

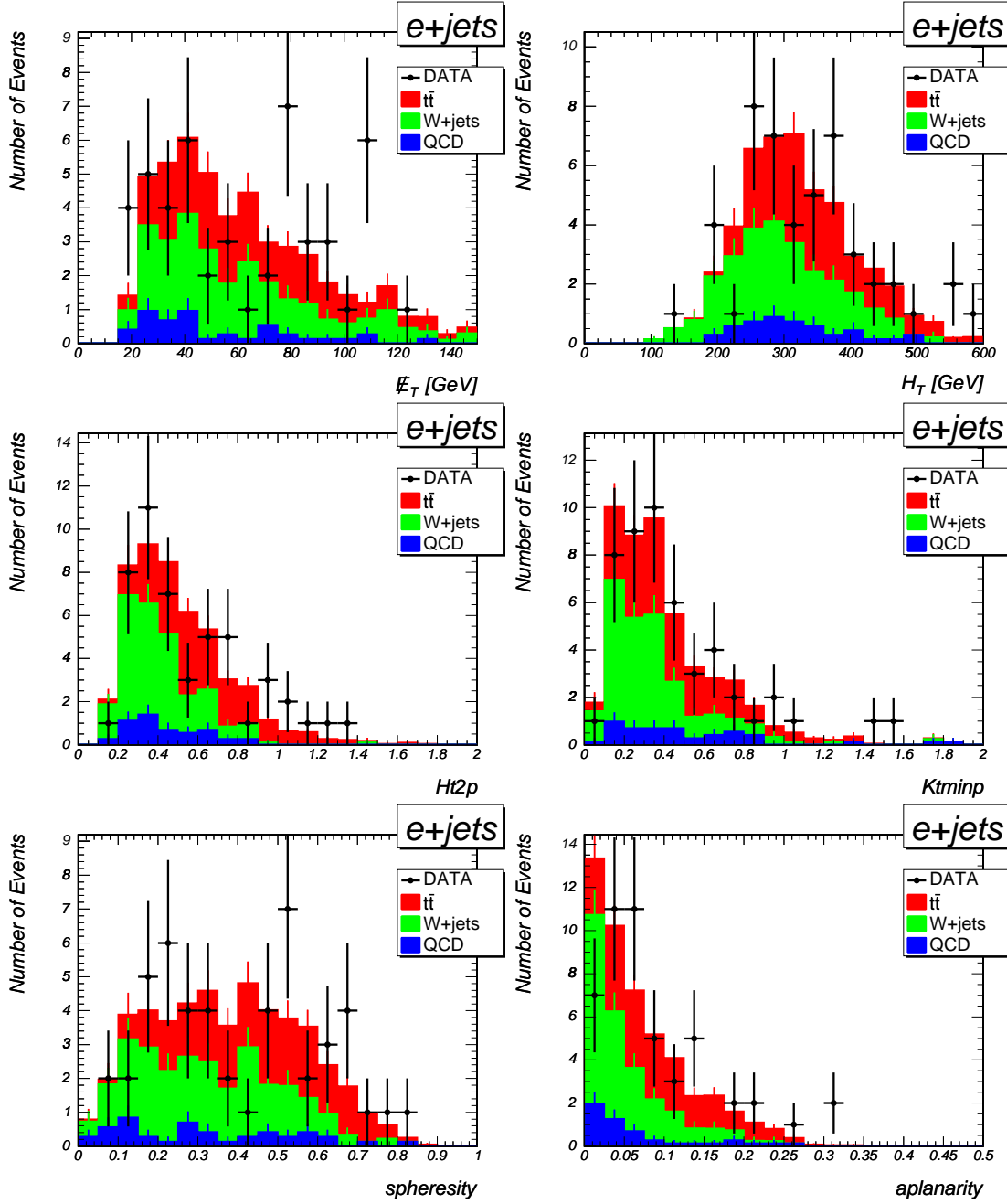


Figure E.3.: Data to Monte Carlo comparison for signal plus background of the selected event sample in the $e + jets$ channel. H_t , H_{t2p} and $ktminp$ are event based energy variables. $Sphericity$ and $aplanarity$ are variables that describe the event shape. The latter four are used in the cross section analyses [1].

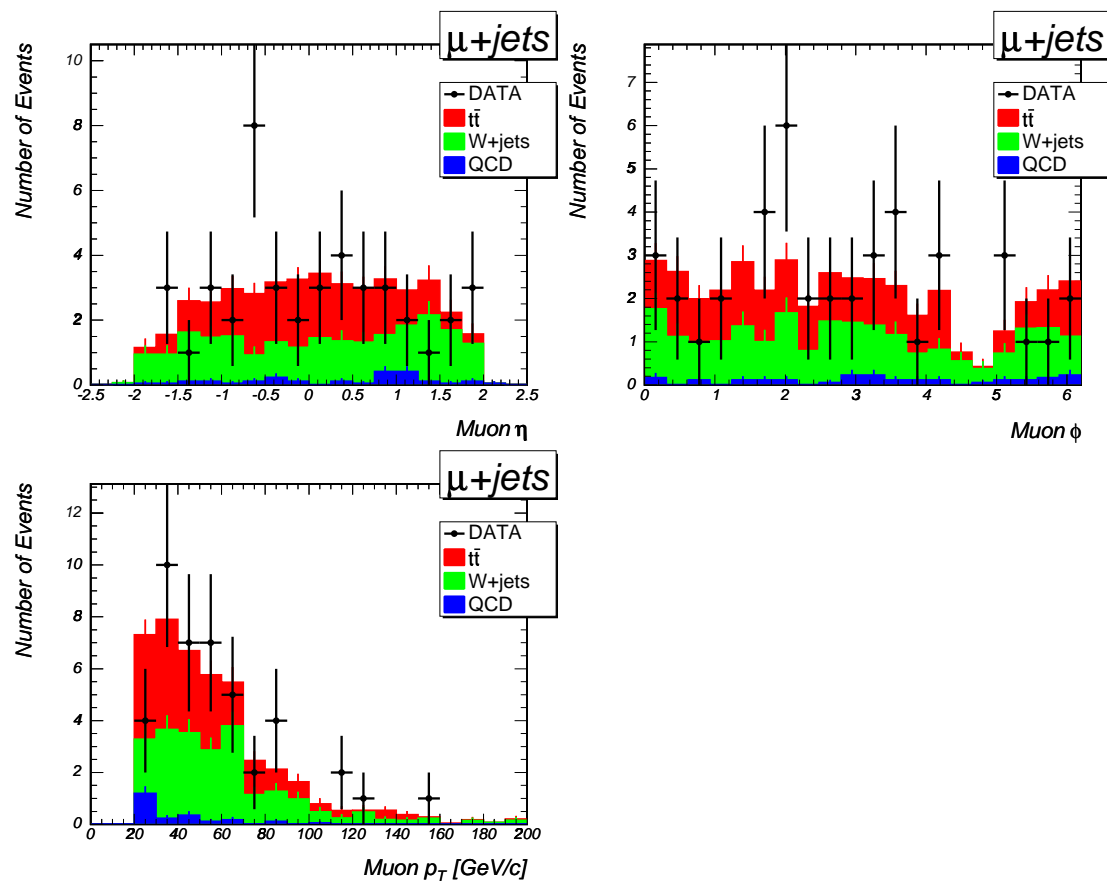


Figure E.4.: Data to Monte Carlo comparison for the signal plus background of the selected event sample in the primary measured kinematic quantities in the $\mu + jets$ channel.

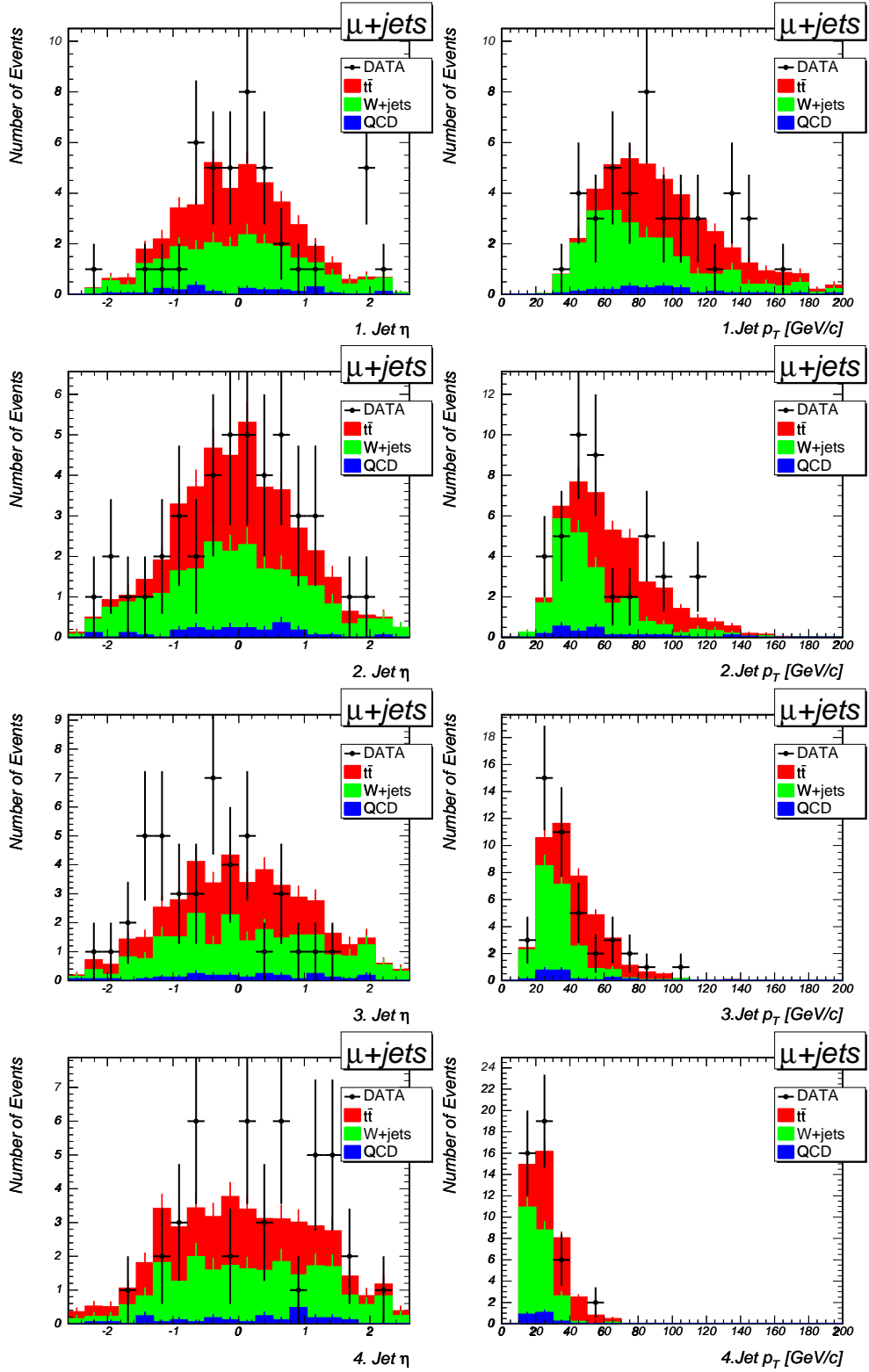


Figure E.5.: Data to Monte Carlo comparison for signal plus background of the selected event sample in the $\mu + jets$ channel.

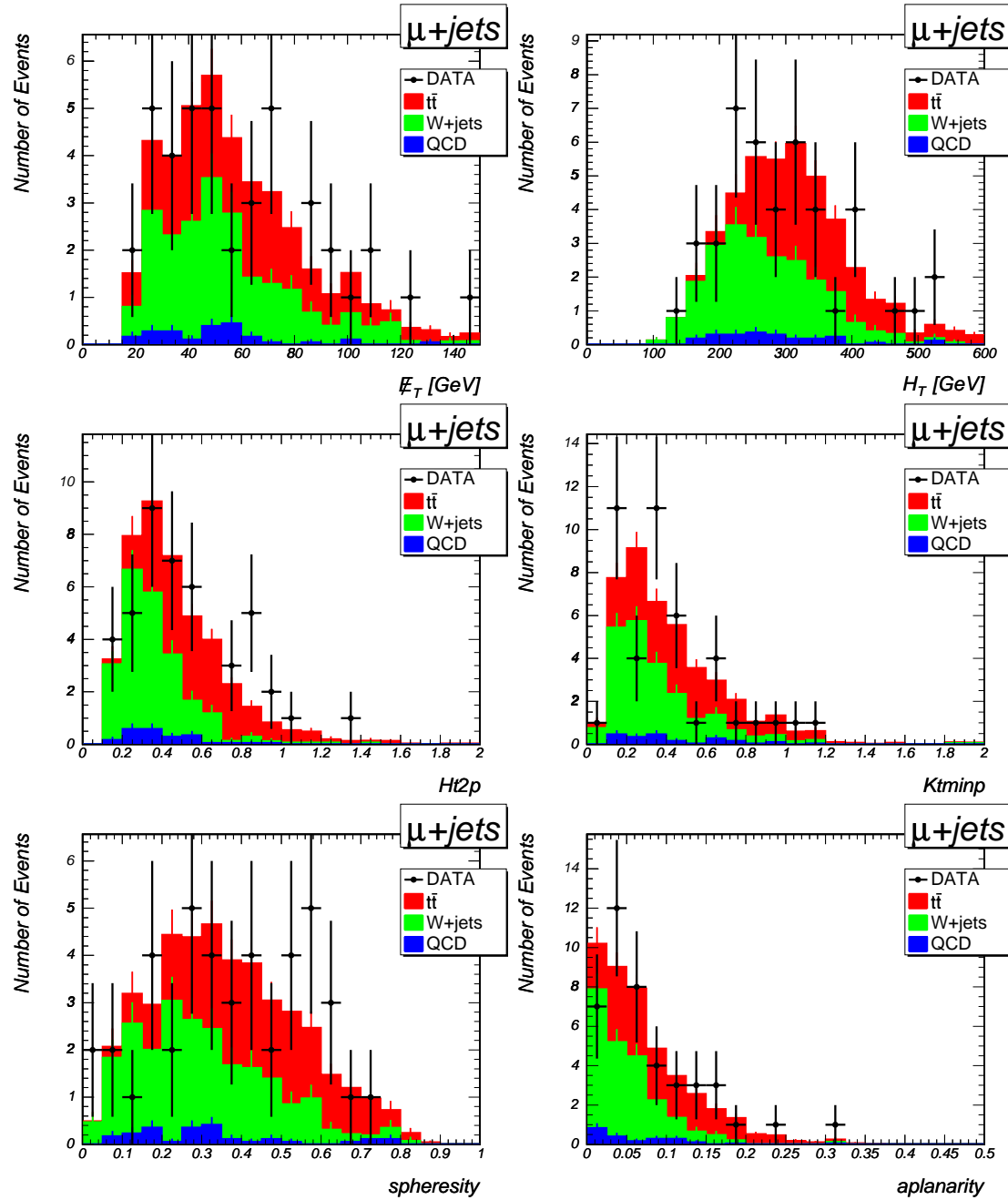


Figure E.6.: Data to Monte Carlo comparison for signal plus background of the selected event sample in the $\mu + \text{jets}$ channel.

Bibliography

- [1] Top Production Group, “Measurement of the $t\bar{t}$ Production Cross-section at $\sqrt{s} = 1.96$ TeV in the Lepton + jets Final States using a Topological Method”, DØ-Note in preparation, March 2004
- [2] H. L. Lai *et al.* (CTEQ Collaboration), “Global QCD analysis of parton structure of the nucleon: CTEQ5 parton distributions”, *Eur. Phys. J. C* **12**, 375, (2000), hep-ph/9903282.
- [3] N. Kidonakis and R. Vogt, “Next-to-next-to-leading order soft-gluon corrections in top quark hadroproduction”, *Phys. Rev. D* **68** (2003) 114014, hep-ph/0308222.
- [4] T. Stelzer, Z. Sullivan and S. Willenbrock, “Single-top-quark production via W-gluon fusion at next-to-leading order”, *Phys. Rev. D* **56**, 5919 (1997), hep-ph/9705398.
- [5] M. C. Smith and S. Willenbrock, “QCD and Yukawa Corrections to Single-Top-Quark Production via $q\bar{q} \rightarrow t\bar{b}$ ”, *Phys. Rev. D* **54**, 6696 (1996), hep-ph/9604223.
- [6] K. G. Chetyrkin and M. Steinhauser, “Three-loop non-diagonal current correlators in QCD and NLO corrections to single top quark production”, *Phys. Lett. B* **502**, 104 (2001), hep-ph/0012002.
- [7] K. Hagiwara *et al.* (Particle Data Group), “Review of Particle Physics”, *Phys. Rev. D* **66**, 010001 (2002).
- [8] The CDF Collaboration, the DØ Collaboration and the TEVATRON Electro-weak working group, “Combination of the CDF and DØ Results on the Top-Quark Mass”, DØ-Note 4417, CDF-Note 6955, TEVEWWG/top 2004/01, April 2004
- [9] The LEP Collaborations ALEPH, DELPHI, L3 and OPAL, The LEP Electroweak Working Group and the SLD Heavy Flavour Group, “A Combination of Preliminary Electroweak Measurements and Constraints on the Standard Model”, CERN-EP/2003-02, hep-ex/0312023 (2003).
- [10] The LEP Collaborations ALEPH, DELPHI, L3 and OPAL, “Electroweak parameters of the Z^0 resonance and the Standard Model”, *Phys. Lett. B* **276**, 247 (1992).
- [11] S. Willenbrock, “Hadron Colliders, the Standard Model and Beyond”, hep-ph/0212032 (2002).
- [12] Fermilab Beams Division, “Run II Handbook”, Fermilab Beams Division Run II webpage, <http://www-bd.fnal.gov/runII/index.html>.
- [13] S. Abachi (DØ Collaboration), “The DØ Upgrade: The Detector and its Physics”, FERMILAB-PUB-96/357-E (1996).

- [14] T. LeCompte and T. Diehl, “The CDF and DØ Upgrades for Run II”, *Ann. Rev. Nucl. Part. Sci.* **50**, page 71-117 (2000).
- [15] D. Denisov *et al.*, “DØ Detector magnets for Run II: geometry, currents and B-H curves”, DØ-Note 3792, November 2000.
- [16] L. Groers, “DØ Calorimeter Upgrades for Tevatron Run II”, DØ-Note 4240, Proceedings for the IXth International Conference on Calorimetry in Particle Physics, Annecy, France, Oct 9-14, 2000.
- [17] M. Adams *et al.*, “Design Report for the Central Preshower Detector for the DØ Upgrade”, DØ-Note 3014, January 1996.
- [18] A. Gordeev *et al.*, “Design Report for the Forward Preshower Detector for the DØ Upgrade”, DØ-Note 3445, May 1998.
- [19] T. Diehl *et al.*, “Technical Design of the Central Muon System”, DØ-Note 3365, March 1998.
- [20] T. Diehl *et al.*, “Technical Design for the DØ Forward Muon Tracking Detector Based on Mini-Drift Tubes”, DØ-Note 3366, December 1997.
- [21] T. Diehl *et al.*, “Technical Design Report for the DØ forward trigger scintillator counters”, DØ-Note 3237, November 1997.
- [22] F. Maltoni and T. Stelzer, “MadEvent: Automatic event generation with MadGraph,” *JHEP* **0302**, 027 (2003), hep-ph/0208156.
- [23] T. Stelzer and W. F. Long, “Automatic generation of tree level helicity amplitudes,” *Comput. Phys. Commun.* **81**, 357 (1994), hep-ph/9401258.
- [24] H. Murayama, I. Watanabe and K. Hagiwara, “HELAS: HELicity amplitude subroutines for Feynman diagram evaluations”, KEK-91-11
- [25] F.A. Berends, H. Kuijf, B. Tausk and W.T. Giele, “On the Production of a W and Jets at Hadron Colliders”, *Nucl. Phys. B* **357**:32-64, 1991.
- [26] K. Kröninger, A. Margerkurth, P. Schieferdecker, A. Quadt “Top Mass Measurement in the Lepton + Jets Channel using the Matrix Element Method in Run II”, DØ-Note in preparation, March 2004.
- [27] G. Mahlon, S. Parke, *Phys. Lett. B* **411**, 133 (1997)
G. Mahlon, S. Parke, *Phys. Rev. D* **53**, 4886 (1996)
- [28] D. O. Carlson, “Physics of Single-Top Quark Production at Hadron Colliders”, hep-ph/9508278.
- [29] M. Jezabek and J.H. Kühn, *Nucl. Phys. B* **314**(1989)1
- [30] K. Hagiwara, D. Zeppenfeld and S. Komamiya, “Excited Lepton Production At Lep And Hera”, *Z. Phys. C* **29** (1985) 1
- [31] <http://cernlib.web.cern.ch/cernlib/>
- [32] F. Canelli, J. Estrada, T. Ferbel, G. Guierrez “Description of a Method Developed to Measure the Mass of the Top Quark at DØ”, DØ-Note 003975, April 2002

-
- [33] F. James (Computing and Networks Division CERN Geneva, Switzerland) “Minuit - Function Minimization and Error Analysis”, CERN Program Library Long Writeup D506
 - [34] M. Klute *et al.*, “TopAnalyze - A Framework Analyze Package For Top Group Analyses”, DØ-Note 4122, March 2003.
 - [35] Top Physics Group, “Direct measurement of the top quark mass in the lepton+jets channel using Run II data (General Note)”, DØ-Note 4266, March 2004.
 - [36] T. Sjöstrand, P. Edén, C. Friberg, L. Lönnblad, G. Miu, S. Mrenna and E. Norrbin, Computer Phys. Commun. 135 (2001) 238 (LU TP 00-30, hep-ph/0010017)
 - [37] Top Physics Group, “DØ Top Analyses and Data Sample for the Winter Conference 2004”, DØ-Note in preparation, February 2004.
 - [38] Top Production Group, “Measurement of the $t\bar{t}$ Production Cross Section at $\sqrt{s} = 1.96$ TeV in Lepton+Jets Final States using Soft Muon Tags” DØ-Note in preparation, March 2004
 - [39] Top Physics Group, “Measurement of the $t\bar{t}$ Xsec at $\sqrt{s} = 1.96$ TeV in the all-jets channel”, DØ-Note 4346, March 2004.

Acknowledgements

This thesis would not have been accomplished without the help and support of many people to whom I would like to express my gratitude.

First of all I would like to thank Prof. N. Vermes for giving me the possibility of writing this thesis. I am grateful for the opportunity of spending almost half of the time at the DØ experiment which was a very interesting and fruitful experience.

I would like to thank Dr. Arnulf Quadt for his support and encouragement. He helped me patiently throughout the whole time of this study and always found time to give me advice. He taught me the enthusiasm for physics and the work within a collaboration.

I would also like to thank the group of Prof. Vermes and Prof. Kobel. I am especially grateful for the advice and support of my colleagues in the local DØ group: Tobias Golling, Markus Klute, Jörg Meyer, Su-Jung Park, Arnulf Quadt, Christian Schwanenberger, Markus Warsinsky and Norbert Vermes.

Since this thesis was done within the DØ collaboration I would like to thank the whole “Top Quark Mass” team, especially Philipp Schieferdecker, Aurelio Juste and Ia Iashvili.

I am grateful for the financial support I received from the Deutscher Akademischer Austausch Dienst and the Heinrich-Hertz-Stiftung. It would not have been possible for me to spend time at the experiment without their assistance.

Last but not least I would like to thank my friends and family who always supported me during my studies. I am very grateful to my parents who made it possible for me to study and who were always there to help me. I would also like to thank my girlfriend Katrin, my brother Dennis and my friends Michael, Sascha and Daniel.